

**BOVINE BONE-BASED HYDROXYAPATITE  
DECORATED WITH  $\text{SnFe}_2\text{O}_4/\text{Bi}_2\text{WO}_6$  COMPOSITE  
FOR PHOTOCATALYTIC MALACHITE GREEN-  
CONTAINING GREYWATER EFFLUENT  
TREATMENT AND ANTIBACTERIAL  
APPLICATIONS**

**GOY CHIEN KAI**

**UNIVERSITI TUNKU ABDUL RAHMAN**

**BOVINE BONE-BASED HYDROXYAPATITE DECORATED WITH  
SnFe<sub>2</sub>O<sub>4</sub>/Bi<sub>2</sub>WO<sub>6</sub> COMPOSITE FOR PHOTOCATALYTIC MALACHITE GREEN-  
CONTAINING GREYWATER EFFLUENT TREATMENT AND  
ANTIBACTERIAL APPLICATIONS**

**GOY CHIEN KAI**

**A project report submitted in partial fulfilment of the requirements for the award of  
the degree of Bachelor of Engineering (Honours) Petrochemical Engineering**

**Faculty of Engineering and Green Technology  
Universiti Tunku Abdul Rahman**

**June 2024**

**DECLARATION**

I hereby declare that this project report is based on my original work except for citations and quotations which have been duly acknowledged. I also declare that it has not been previously and concurrently submitted for any other degree or award at UTAR or other institutions.

Signature : GOY CHIEN KAI

Name : GOY CHIEN KAI

ID No. : 19AGB03586

Date : 16/5/2024\_\_\_\_\_

**APPROVAL FOR SUBMISSION**

I certify that this project report entitled **“BOVINE BONE-BASED HYDROXYAPATITE DECORATED WITH SnFe<sub>2</sub>O<sub>4</sub>/Bi<sub>2</sub>WO<sub>6</sub> COMPOSITE FOR PHOTOCATALYTIC MALAHITE GREEN-CONTAINING GREYWATER EFFLUENT TREATMENT AND ANTIBACTERIAL APPLICATIONS”** was prepared by GOY CHIEN KAI has met the required standard for submission in partial fulfilment of the requirements for the award of Bachelor of Engineering (Hons) Petrochemical Engineering at Universiti Tunku Abdul Rahman.

Approved by,

Signature : *Sin Jin Chung* \_\_\_\_\_

Supervisor : Assoc.Prof. ChM. Ts. Dr. Sin Jin Chung

Date : 17/5/2024 \_\_\_\_\_

Signature : *Lam Sze Mun* \_\_\_\_\_

Supervisor : Assoc.Prof. ChM. Ts. Dr. Lam Sze Mun

Date : 17/5/2024 \_\_\_\_\_

The copyright of this report belongs to the author under the terms of the copyright Act 1987 as qualified by Intellectual Property Policy of Universiti Tunku Abdul Rahman. Due acknowledgement shall always be made of the use of any material contained in, or derived from, this report.

© 2024, Goy Chien Kai. All right reserved.

Special dedicated to  
My beloved parents, supervisors, lecturers, seniors, and friends.

## ACKNOWLEDGEMENTS

I would like to express my sincere gratitude to everyone who had led me a hand in completing this project.

I extend my deepest gratitude to my supervisor, Assoc. Prof. ChM. Ts. Dr. Sin Jin Chung and co-supervisor Assoc. Prof. ChM. Ts. Dr. Lam Sze Mun for their unwavering guidance, wisdom and encouragement throughout the course of this project. Their invaluable insights, constructive feedback, and patience have been instrumental in shaping the direction of my research and fostering my growth as a budding scholar, I am truly grateful for their dedication, mentorship, and belief in my abilities. My greatest gratitude also goes to my moderator, Ir. Ts. Dr. Toh Pey Yi, for their insightful feedback.

In addition, I wish to thank all of the helpful and pleasant laboratory officers, particularly Ms. Lim Cheng Yen, Mrs. Ropidah Hamimi binti Mohd Zain and Mr. Yong Tzyy Jeng, for their outstanding support in giving technical assistance during the completion of Final Year Project.

I extend my deepest gratitude to my family and friends for their unwavering love, encouragement, and understanding during this challenging yet rewarding endeavour. Their unwavering support, patience, and belief in my abilities have been a constant source of strength and motivation throughout the ups and downs of this journey. I am profoundly grateful for their sacrifices, encouragement, and unwavering faith in my dreams. Last but not least, my heartfelt appreciation goes to one of my friend and senior, Lim Khar Lok, for his guidance and encouragement during this project.

**BOVINE BONE-BASED HYDROXYAPATITE DECORATED WITH  
SnFe<sub>2</sub>O<sub>4</sub>/Bi<sub>2</sub>WO<sub>6</sub> COMPOSITE FOR PHOTOCATALYTIC MALACHITE  
GREEN-CONTAINING GREYWATER EFFLUENT TREATMENT AND  
ANTIBACTERIAL APPLICATIONS**

**ABSTRACT**

Greywater contains dyes, pathogenic bacteria and microorganism, making its treatment essential for addressing potential future water crises. Heterogeneous photocatalysis with semiconductor material is proved highly efficient in removing organic contaminants which is well-suited in Malaysia as this country is located in a tropical latitude with consistent sunlight. In this study, a novel 7.5wt%-SnFe<sub>2</sub>O<sub>4</sub>/Bi<sub>2</sub>WO<sub>6</sub>/HAp ternary nanocomposite material was fabricated via solvothermal-deposition method. The morphological structure, energy bandgap, charge transfer properties, recombination of photoexcited electron-hole pairs, crystallinity, and crystal orientation of as-fabricated photocatalyst are determined via different analytical techniques. The result displayed that visible-light absorption range of composite materials has extended to longer wavelength that covered the visible light spectrum in addition to 7.5wt%-SnFe<sub>2</sub>O<sub>4</sub>/Bi<sub>2</sub>WO<sub>6</sub>/HAp with 1wt% HAp loading has the greatest visible light photosensitivity. The photocatalytic capabilities are assessed through decomposition of MG under sunlight illumination for 180 minutes. This ternary nanocomposite has demonstrated the highest photocatalytic activity where removal efficiency of 84.63% MG ( $k_{app} = 0.0088 \text{ min}^{-1}$ ) and 99.59% MG ( $k_{app} = 0.0211 \text{ min}^{-1}$ ) in greywater were achieved separately. The phytotoxicity studies revealed toxicity level of MG-containing greywater was greatly reduced after being treated with 7.5wt%-SnFe<sub>2</sub>O<sub>4</sub>/Bi<sub>2</sub>WO<sub>6</sub>/HAp-1wt%. The *E. coli* inactivation experiment showed that this photocatalyst has the highest anti-microorganism ability and largely restrained bacterial activity. This present work manifests multifunction of 7.5wt%-SnFe<sub>2</sub>O<sub>4</sub>/Bi<sub>2</sub>WO<sub>6</sub>/HAp-1wt% in photodecomposition of organic dyes and antibacterial application under sunlight irradiation.



**TABLE OF CONTENT**

<b>DECLARATION</b>	<b>II</b>
<b>APPROVAL FOR SUBMISSION</b>	<b>III</b>
<b>ACKNOWLEDGEMENTS</b>	<b>VI</b>
<b>ABSTRACT</b>	<b>VII</b>
<b>LIST OF TABLES</b>	<b>XII</b>
<b>LIST OF FIGURES</b>	<b>XIII</b>
<b>LIST OF SYMBOLS/ABBREVIATIONS</b>	<b>XVII</b>
<b>CHAPTER 1</b>	<b>1</b>
<b>INTRODUCTION</b>	<b>1</b>
1.1 Background of Study	1
1.2 Problem Statement	5
1.3 Objectives	9
1.4 Scope of Study	9
<b>CHAPTER 2</b>	<b>10</b>
<b>LITERATURE REVIEW</b>	<b>10</b>
2.1 Water Pollution and Greywater	10

2.2	Review on Dye and compositions in Household Greywater	14
2.3	Usage and Hazardous Effects of Malachite Green	20
2.4	Heterogenous Photocatalysis	22
2.5	Bi <sub>2</sub> WO <sub>6</sub> as Photocatalyst	24
2.6	Mechanism of Bi <sub>2</sub> WO <sub>6</sub> Photocatalysis	32
2.7	Modifications of Bi <sub>2</sub> WO <sub>6</sub>	36
2.8	Phytotoxicity	43
2.9	Antibacterial Experiments	45
2.10	Summary of Literature Review	46
	<b>CHAPTER 3</b>	<b>48</b>
	<b>METHODOLOGY</b>	<b>48</b>
3.3	Preparation of Photocatalyst	51
3.4	Characterization	56
3.4.1	X-ray Diffraction (XRD)	56
3.4.2	Field Emission Scanning Electron Microscopy (FESEM) and Energy Dispersive X-ray (EDX) Spectroscopy	56
3.4.3	Ultraviolet – Visible Diffuse Reflectance Spectroscopy (UV-vis DRS)	56
3.4.4	Fourier Transform Infrared Spectroscopy – Attenuated Total Reflectance (FTIR-ATR)	57
3.4.5	Transient Photocurrent Response (TPR), Electrochemical Impedance Spectroscopy (EIS), Mott-Schottky (M-S), and Cyclic Voltammetry (CV)	57
3.5	Photoactivity Test	58
3.6	Phytotoxicity Test	61
3.7	Radical Scavenging Experiment	61

3.8	<i>E. coli</i> inactivation experiment	62
<b>CHAPTER 4</b>		<b>63</b>
<b>RESULT AND DISCUSSION</b>		<b>63</b>
4.1	Characterization	63
4.1.1	Field Emission Scanning Electron Microscopy (FESEM)	63
4.1.2	Energy Dispersive X-ray (EDX)	66
4.1.3	X-ray Diffraction (XRD)	71
4.1.4	Attenuated Total Reflectance – Fourier Transform Infrared Spectroscopy (ATR-FTIR)	74
4.1.5	Ultraviolet-visible Diffuse Reflectance Spectroscopy (UV-vis DRS)	77
4.1.6	Transient Photocurrent Response (TPR), Electrochemical Impedance Spectroscopy (EIS), Mott-Schottky (M-S), and Cyclic Voltammetry (CV)	80
4.2	Solar Photocatalytic Activities	85
4.2.1	Photodegradation of Malachite Green (MG)	85
4.2.2	Photodegradation of greywater containing Malachite Green (MG)	90
4.3	Phytotoxicity Evaluation	96
4.4	Radical Scavenging Experiment	99
4.5	Antibacterial Experiment	102
<b>CHAPTER 5</b>		<b>103</b>
<b>CONCLUSION AND RECOMMENDATIONS</b>		<b>103</b>
5.1	Conclusion	103
5.2	Recommendation	104
<b>REFERENCES</b>		<b>106</b>

**LIST OF TABLES**

<b>TABLE</b>	<b>TITLE</b>	<b>PAGE</b>
2.1	: Microbial illnesses connected with polluted waters.	13
2.2	: Standard of treated greywater in some developing and developed countries.	15
2.3	: Greywater characteristics of low-income countries (LIC) and high-income countries (HIC).	19
2.4	: Acceptable conditions for discharge of industrial effluent or mixed effluent of standard A and B.	20
2.5	: General properties of Malachite Green.	22
2.6	: Comparison between bismuth-based photocatalyst.	30
2.7	: Summary of Bi <sub>2</sub> WO <sub>6</sub> with various morphologies for diverse photocatalytic applications.	32
2.8	: Photocatalytic performance of Bi <sub>2</sub> WO <sub>6</sub> -Based Heterojunction ternary Photocatalyst on different kinds of pollutant.	43
3.1	: List of Materials and Chemicals used.	50
4.1	: Comparison of photocatalytic MG degradation over Bi <sub>2</sub> WO <sub>6</sub> -based photocatalyst.	95

## LIST OF FIGURES

FIGURE	TITLE	PAGE
2.1	: redox reactions (Oxidation and reduction) on semiconductor photocatalyst.	24
2.2	: (a) Schematic illustration of semiconductor photocatalysis, (b) Crystal structure of $\text{Bi}_2\text{WO}_6$ , (c) hybridization of Bi 6s + O 2p orbitals lead to high redox potential.	27
2.3	: Photodegradation of organic pollutant by $\text{Bi}_2\text{WO}_6$ .	36
2.4	: Schematic illustration of electron-hole separation on a direct Z-scheme heterojunction photocatalyst under light irradiation	38
3.1	: Overall Experimental Flowchart	49
3.2	: Synthesis of $\text{SnFe}_2\text{O}_4$ photocatalyst	52
3.3	: Synthesis of $\text{Bi}_2\text{WO}_6$ photocatalyst.	53
3.4	: Synthesis of 7.5wt%- $\text{SnFe}_2\text{O}_4/\text{Bi}_2\text{WO}_6$ binary composite	54
3.5	: Synthesis of HAp powder.	55
3.6	: Synthesis of 7.5wt%- $\text{SnFe}_2\text{O}_4/\text{Bi}_2\text{WO}_6/\text{HAp}$ ternary composite.	56
3.7	: Experiment Setup for photodegradation of Malachite Green dye in distilled water.	59
3.8	: MG calibration curve of Absorbance versus concentration (Distilled water + MG).	60
3.9	: Experiment Setup for photodegradation of Malachite Green dye in greywater.	61
3.10	: MG calibration curve of Absorbance versus concentration (Greywater+ MG).	61
4.1	: FESEM images of as-synthesized photocatalysts; (a) $\text{SnFe}_2\text{O}_4$ ; (b) $\text{Bi}_2\text{WO}_6$ ; (c) HAp; (d) 7.5wt%- $\text{SnFe}_2\text{O}_4/\text{Bi}_2\text{WO}_6$ ; (e) $\text{SnFe}_2\text{O}_4/\text{HAp}$ -1wt%; (f) $\text{Bi}_2\text{WO}_6/\text{HAp}$ -1wt%; (g) 7.5wt%- $\text{SnFe}_2\text{O}_4/\text{Bi}_2\text{WO}_6/\text{HAp}$ -1wt%; (h) 7.5wt%- $\text{SnFe}_2\text{O}_4/\text{Bi}_2\text{WO}_6/\text{HAp}$ -3wt%; (i) 7.5wt%- $\text{SnFe}_2\text{O}_4/$	66

Bi<sub>2</sub>WO<sub>6</sub>/HAp-5wt%; (j) 7.5wt%- SnFe<sub>2</sub>O<sub>4</sub>/Bi<sub>2</sub>WO<sub>6</sub>/HAp-10wt%. [Blue arrow represent SnFe<sub>2</sub>O<sub>4</sub>; yellow arrow represent Bi<sub>2</sub>WO<sub>6</sub>; red arrow represent HAp]

- |      |   |   |    |
|------|---|---|----|
| 4.2  | : | (a) The EDX spectra of SnFe <sub>2</sub> O <sub>4</sub> ; (b)-(e) elemental dot mapping of SnFe <sub>2</sub> O <sub>4</sub> .   | 68 |
| 4.3  | : | (a) The EDX spectra of Bi <sub>2</sub> WO <sub>6</sub> ; (b)-(e) elemental dot mapping of Bi <sub>2</sub> WO <sub>6</sub> .   | 68 |
| 4.4  | : | (a) The EDX spectra of HAp; (b)-(e) elemental dot mapping of HAp.   | 68 |
| 4.5  | : | (a) The EDX spectra of 7.5 wt%-SnFe <sub>2</sub> O <sub>4</sub> /Bi <sub>2</sub> WO <sub>6</sub> ; (b)-(g) elemental dot mapping of 7.5 wt%-SnFe <sub>2</sub> O <sub>4</sub> /Bi <sub>2</sub> WO <sub>6</sub> .                                 | 69 |
| 4.6  | : | (a) The EDX spectra of SnFe <sub>2</sub> O <sub>4</sub> /HAp-1 wt%; (b)-(g) elemental dot mapping of SnFe <sub>2</sub> O <sub>4</sub> / HAp-1 wt%.  | 69 |
| 4.7  | : | (a) The EDX spectra of Bi <sub>2</sub> WO <sub>6</sub> /HAp-1 wt%; (b)-(g) elemental dot mapping of Bi <sub>2</sub> WO <sub>6</sub> / HAp-1 wt%.  | 69 |
| 4.8  | : | (a) The EDX spectra of 7.5 wt%-SnFe <sub>2</sub> O <sub>4</sub> /Bi <sub>2</sub> WO <sub>6</sub> /HAp-1 wt%; (b)-(i) elemental dot mapping of 7.5 wt%-SnFe <sub>2</sub> O <sub>4</sub> /Bi <sub>2</sub> WO <sub>6</sub> / HAp-1 wt%.            | 70 |
| 4.9  | : | (a) The EDX spectra of 7.5 wt%-SnFe <sub>2</sub> O <sub>4</sub> /Bi <sub>2</sub> WO <sub>6</sub> /HAp-3 wt%; (b)-(i) elemental dot mapping of 7.5 wt%-SnFe <sub>2</sub> O <sub>4</sub> /Bi <sub>2</sub> WO <sub>6</sub> / HAp-3 wt%.            | 70 |
| 4.10 | : | (a) The EDX spectra of 7.5 wt%-SnFe <sub>2</sub> O <sub>4</sub> /Bi <sub>2</sub> WO <sub>6</sub> /HAp-5 wt%; (b)-(i) elemental dot mapping of 7.5 wt%-SnFe <sub>2</sub> O <sub>4</sub> /Bi <sub>2</sub> WO <sub>6</sub> / HAp-5 wt%.            | 70 |
| 4.11 | : | (a) The EDX spectra of 7.5 wt%-SnFe <sub>2</sub> O <sub>4</sub> /Bi <sub>2</sub> WO <sub>6</sub> /HAp-10 wt%; (b)-(i) elemental dot mapping of 7.5 wt%-SnFe <sub>2</sub> O <sub>4</sub> /Bi <sub>2</sub> WO <sub>6</sub> / HAp-10 wt%.          | 71 |
| 4.12 | : | (a) The XRD spectra of as-fabricated single photocatalysts: (a) SnFe <sub>2</sub> O <sub>4</sub> ; (b) Bi <sub>2</sub> WO <sub>6</sub> ; and (c) HAp.   | 73 |
| 4.13 | : | (a) The XRD spectra of as-fabricated binary photocatalysts: (a) 7.5 wt%-SnFe <sub>2</sub> O <sub>4</sub> / Bi <sub>2</sub> WO <sub>6</sub> ; (b) Bi <sub>2</sub> WO <sub>6</sub> /HAp-1wt%; and (c) SnFe <sub>2</sub> O <sub>4</sub> /HAp-1wt%. | 74 |
| 4.14 | : | (a) The XRD spectra of as-fabricated ternary photocatalysts with different HAp loading: (a) 7.5 wt%-SnFe <sub>2</sub> O <sub>4</sub> /Bi <sub>2</sub> WO <sub>6</sub> /HAp-1wt%; (b) 7.5 wt%-   | 74 |

SnFe<sub>2</sub>O<sub>4</sub>/Bi<sub>2</sub>WO<sub>6</sub>/HAp-3wt%; and (c) 7.5 wt%-  
 SnFe<sub>2</sub>O<sub>4</sub>/Bi<sub>2</sub>WO<sub>6</sub>/HAp-5wt%; 7.5 wt%-  
 SnFe<sub>2</sub>O<sub>4</sub>/Bi<sub>2</sub>WO<sub>6</sub>/HAp-10wt%.

- 4.15 : The ATR-FTIR spectra of as-fabricated photocatalysts. 77
- 4.16 : UV-vis absorbance spectra of the as-synthesized photocatalysts. 80
- 4.17 : Energy analysis of the as-synthesized photocatalysts via Tauc plot. 80
- 4.18 : Transient Photocurrent Response of the as-synthesized photocatalysts. 84
- 4.19 : Electrochemical Impedance Spectroscopy analysis of the as-fabricated photocatalysts. 84
- 4.20 : Cyclic voltammetry of the as-synthesized photocatalysts. 85
- 4.21 : Mott-Schottky analysis of as-prepared photocatalysts: (a) pristine SnFe<sub>2</sub>O<sub>4</sub>; (b) pristine Bi<sub>2</sub>WO<sub>6</sub>; (c) pristine HAp. 85
- 4.22 : (a) Degradation profiles of Malachite Green over as-synthesized photocatalyst; (b) Kinetic study for the photodegradation of Malachite Green; (c) Apparent reaction rate constant,  $k_{app}$  over as-synthesized photocatalyst; (d) Absorption spectra of Malachite Green over 7.5wt%-SnFe<sub>2</sub>O<sub>4</sub>/Bi<sub>2</sub>WO<sub>6</sub>/HAp-1wt% ternary composite with the decolourization inset. 90
- 4.23 : 4.23: (a) Degradation profiles of Malachite Green over as-synthesized photocatalyst in greywater; (b) Kinetic study for the photodegradation of Malachite Green in greywater; (c) Apparent reaction rate constant,  $k_{app}$  over as-synthesized photocatalyst; (d) Absorption spectra of Malachite Green in greywater over 7.5wt%-SnFe<sub>2</sub>O<sub>4</sub>/Bi<sub>2</sub>WO<sub>6</sub>/HAp-1wt% ternary composite with the decolorization inset. 94
- 4.24 : shows schematic diagram for the pathway of photocatalytic degradation of MG from complex structure to simpler molecular components. 96
- 4.25 : Figure 4.25: (a) The growth of Mung Beans after 7 Days in different conditions; radicles length of Mung Beans at (b) distilled water; (c) untreated greywater; (d) treated 99

- greywater; (e) Phytotoxicity of MG dye in greywater before and after degradation using 7.5wt%-SnFe<sub>2</sub>O<sub>4</sub>/Bi<sub>2</sub>WO<sub>6</sub>/HAp-1wt% nanocomposite.
- 4.26 : Radical scavenging experiment over 7.5wt%-SnFe<sub>2</sub>O<sub>4</sub>/Bi<sub>2</sub>WO<sub>6</sub>/HAp-1wt% nanocomposite. 102
- 4.27 : Schematic illustration of charge carrier separation and transfer pathway and photocatalytic mechanism of Z-scheme 7.5wt%-SnFe<sub>2</sub>O<sub>4</sub>/Bi<sub>2</sub>WO<sub>6</sub>/HAp-1wt% nanocomposite heterojunction under sunlight irradiation. 102



## LIST OF SYMBOLS/ABBREVIATIONS

$\alpha$	Absorption coefficient
$\theta$	Diffraction angle, °
$\lambda$	Wavelength, nm
$B$	Optical-transition-dependent constant
$C_0$	Concentration of pollutant at time (t = 0), mg/L
$C_t$ or $C$	Concentration of pollutant at given time, mg/L
$E^0$	Redox potential, V
$E_{CB}$	Conduction band potential, eV
$E_g$	Energy bandgap, eV
$E_{VB}$	Valence band potential, eV
$h$	Planck's constant, J-s
$k_{app}$	Apparent reaction rate constant, min <sup>-1</sup>
$n$	Nature of transmission
$t$	Reaction time, min
$\nu$	Frequency of incident beam, Hz
$e^-$	Electrons
$e_{CB}^-$	Conduction band electrons
$h^+$	Holes
$h_{VB}^+$	Valence band holes
$h_{tr}^+$	Trapped holes
$h_\nu$	photons
$H^+$	Hydrogen ion
$HO_2^\bullet$	Hydroperoxyl radical
$O_2^{\bullet-}$	Superoxide radical
$OH^-$	Hydroxyl group
$OH^\bullet$	Hydroxyl radical
$I_{pa}$	Anodic peak current
$E_{pa}$	Anodic peak potential
$E_{FB}$	Flat band potential

2D	Two-dimensional
3D	Three-dimensional
Ag	Silver
AgI	Silver iodide
AOPs	Advanced oxidation processes
ATR-FTIR	Attenuated Total Reflectance-Fourier Transform Infrared Spectroscopy
Ba	Barium
BET	Barrett-Emmett-Teller
BOD	Biochemical oxygen demand
Bi	Bismuth
BQ	Benzoquinone
BWO	Bismuth tungstate
BiFeO <sub>3</sub>	Bismuth ferrite
BiMnO <sub>3</sub>	Bismuth manganese oxide
BiOBr	Bismuth oxobromide
BiVO <sub>4</sub>	Bismuth vanadate
BiVO <sub>5</sub>	Bismuth vanadate
Bi(NO <sub>3</sub> ) <sub>3</sub> ·5H <sub>2</sub> O	Bismuth nitrate pentahydrate
Bi <sub>2</sub> O <sub>3</sub> ·nMoCO <sub>3</sub>	Bismuth Molybdate
Bi <sub>2</sub> O <sub>3</sub>	Bismuth oxide
Bi <sub>2</sub> MnO <sub>6</sub>	Bismuth manganese oxide
Bi <sub>2</sub> MoO <sub>6</sub>	Bismuth molybdenum oxide
Bi <sub>2</sub> S <sub>3</sub>	Bismuth sulfide
Bi <sub>2</sub> WO <sub>6</sub>	Bismuth Tungstate
Ca	Calcium
CAGR	Compound annual growth rate
CB	Conduction band
CBBR	Coomassie brilliant blue
CIP	Ciprofloxacin
Cl <sub>2</sub>	Chlorine
Co	Cobalt

CO <sub>2</sub>	Carbon dioxide
COD	Chemical oxygen demand
Cr (VI)	Hexavalent chromium
Cu	Copper
CV	Cyclic voltammetry
C <sub>2</sub> H <sub>5</sub> OH	Ethyl alcohol
C <sub>2</sub> H <sub>6</sub> O <sub>2</sub>	Ethylene glycol
C <sub>6</sub> H <sub>10</sub> O <sub>2</sub>	Benzoquinone
C <sub>7</sub> HF <sub>13</sub> O <sub>5</sub> S·C <sub>2</sub> F <sub>4</sub>	Nafion
C <sub>10</sub> H <sub>16</sub> N <sub>2</sub> O <sub>8</sub>	Ethylenediaminetetraacetic
C <sub>16</sub> H <sub>18</sub> ClN <sub>3</sub> S	Methylene blue
C <sub>28</sub> H <sub>25</sub> ClN <sub>2</sub>	Malachite green
Ca <sub>10</sub> (PO <sub>4</sub> ) <sub>6</sub> (OH) <sub>2</sub>	hydroxyapatite
DO	Dissolved oxygen
DOE	Department of Environment
E. coli	Escherichia coli
EDTA	Ethylenediaminetetraacetic
EDX	Energy Dispersive X-ray
EIS	Electrochemical Impedance Spectroscopy
EQA	Environmental Quality Act
EtOH	Ethyl alcohol
eV	Electron volt
FC	Faecal coliforms
Fe	Iron
Fe <sup>2+</sup>	Iron (II) ion
Fe <sup>3+</sup>	Iron (III) ion
FeCl <sub>3</sub> ·6H <sub>2</sub> O	Iron (III) Chloride Hexahydrate
Fe(OH) <sub>3</sub>	Iron (III) oxide-hydroxide
FESEM	Field Emission Scanning Electron Spectroscopy
GI	Germination index
GO	Graphene oxide
HAp	hydroxyapatite
H <sub>2</sub>	Hydrogen

$\text{H}_2\text{O}_2$	Hydrogen peroxide
$\text{H}_2\text{O}$	Distilled water
HCl	Hydrochloric acid
HIC	High-income countries
$\text{HNO}_2$	Nitrous acid
$\text{HNO}_3$	Nitric acid
HRTEM	High resolution transmission emission microscopy
IUPAC	International Union of Pure and Applied Chemistry
JCPDS	Joint Committee on Powder Diffraction Standards
K	Potassium
KOH	Potassium hydroxide
LB	Luria-Bertani
LIC	Low-income countries
MB	Methylene blue
MBR	Membrane bioreactor
MG	Malachite green
$\text{MoS}_2$	Molybdenum disulfide
Mn	Manganese
M-S	Mott Schottky
N	Nitrogen
$\text{N}_2$	Nitrogen
Na	Sodium
$\text{Na}_2\text{WO}_6 \cdot 2\text{H}_2\text{O}$	Sodium tungstate dihydrate
NaCl	Sodium chloride
NaOCl	Sodium hypochlorite
NaOH	Sodium hydroxide
$\text{Na}_2\text{SO}_4$	Sodium sulphate
$\text{NH}_4^+$	Ammonium cation
NHE	Normal hydrogen electrode
NO	Nitrogen monoxide
$\text{NiWO}_6$	Nickel tungstate
O	Oxygen
$\text{O}_3$	Ozone

OG	Orange G
P	Phosphorus
pH	Potential of Hydrogen
PL	photoluminescence
PO <sub>4</sub> <sup>3-</sup>	Phosphate ion
pzc	Point of zero charge
RBC	Rotating biological contractor
RhB	Rhodamine B
ROS	Reactive oxygen species
rpm	Rotation per minute
SDG	Sustainable development goal
Sn	Tin
Sn <sup>2+</sup>	Stannous cation
SnCl <sub>4</sub> ·5H <sub>2</sub> O	Tin (IV) chloride pentahydrate
SnFe <sub>2</sub> O <sub>4</sub>	Tin ferrite
SSR	Solid state reaction
Ta	Tantalum
TC	Total coliforms
TC	Tetracycline
Ti	Titanium
TN	Total nitrogen
TiO <sub>2</sub>	Titanium dioxide
TOC	Total organic carbon
TP	Total phosphorus
TPR	Transient Photocurrent Response
TSS	Total suspended solid
UASB	Up-flow anaerobic sludge blanket system
UV	ultraviolet
UV-vis DRS	Ultraviolet-visible Diffuse Reflectance Spectroscopy
USD	United States Dollars
USEPA	United States Environmental Protection Agency
UTAR	Universiti Tunku Abdul Rahman
VB	Valence band

W	Tungsten
WHO	World health organization
WO <sub>3</sub>	Tungsten (IV) oxide
Xe	Xenon
XRD	X-ray Diffraction
ZBO	Zinc bismuthate
ZnBiO <sub>4</sub>	Zinc bismuthate
ZnO	Zinc oxide
ZnCdS	Zinc Cadmium Sulfide
ZnWO <sub>6</sub>	Zinc tungstate
Zr	Zirconium

## **CHAPTER 1**

### **INTRODUCTION**

#### **1.1 Background of Study**

All living things found on Earth require water for survival and it is one of most crucial yet indispensable natural resources to human beings. Although the earth surface is covered with almost 71% of water in nature, however merely approximately 3% of water source are fresh water, and yet less than 1% of this drinkable source are accessible by human beings (Yusof et al, 2022). According to Zaheer (2023), annual water consumption in the globe is almost 4 trillion cubic meters. The water consumption in the worldwide is basically classified into three types of uses, namely agriculture irrigation, industrial process, and domestic purposes. Approximately 75% to 90% of freshwater is mostly consumed by low-income or developing countries such as Pakistan, Thailand and Thailand that relied on agriculture sector. 17% of total freshwater has been consumed for industrial manufacturing processes in developed countries such as United State and China. While 11% of global water is utilized for sake of municipal and domestic uses. For an instance, China consumes as high as 70 billion cubic meters of water per annum in aspect of domestic purpose such as washing and cleaning activities. Yet, owing to the increasing water demand in the world, freshwater shortage problem has been discussed and sparked a hot controversial topic in recent year owing to factors of an increase in water pollution, urbanization, climate change, rapid growth in global population and industrialization. According to the progress report published in 2021, the world population was near to 8 billion people by 2030, however, merely 81% of population is accessible to safe drinking water and the remaining 19% population might experience lacking safely managed drinking

water in their daily life (United Nations, 2021). The consumption of unsafe water without undergoing standard sanitation or purification process poses to health problem and even death. According to Prüss-Üstün et al. (2008) mentioned that continuous amelioration of water quality in aspect of hygiene and sanitation could avoid at minimum 9.1% of disease burden or 6.3% of death in the world caused by the consumption of unclean water source containing pathogenic microorganisms. Viewed from certain angle, Malaysia is one of the water-rich countries which is attributed to the annual rainfall greater than 3000mm, nevertheless, the water pollutions and unsustainable land-use practices has adversely affected the water quality and subsequently lead to a reduction of clean water supply. Meanwhile, Malaysia's daily water consumption per capita was reported as 205 liters which is far exceeding the recommended 165 liters per day by World Health Organization and water demand in Malaysia is expected to enhance to as high as 103% than current demand by 2050. When the basic demand far exceeds supply, a potential crisis such as water shortage can be foreseen. According to the report by Mathew and Ismail (2023), they stated that the relatively low water tariff in Malaysia results in excessive use of water and improper disposal of contaminated wastes to the rivers, are hardly be treated by the current number of wastewater treatment plants.

In addition, greywater production produced is kept accelerating due to the growth in population. According to United States Environmental Protection Agency (2023), it estimated that one people can use up to 303 liters of water per day at home. The domestic greywater volume per capita that generated in Asian countries is estimated in the range of 72 and 225 Liters per day, daily activities such as shower and laundry may use up to a total of 86 liters per day where it is deem as normal in areas supplied with piped water source. For greywater produced in the household, bathroom accounts for up to 60% of total greywater production, followed by laundry and kitchen greywater. World Health Organization (2006) also stated that average total wastewater produced per household is 586 Liters per day in which greywater production occupied 61%. The total volume of greywater generated in the household can be further heighten up to 90% if dry latrine is in pervasiveness (Oteng-Peprah et al.,2018). Furthermore, urbanization in each country is become prevalent and mostly two-third of population is expected to live in urban area by 2050. Yet, this scenario is brought about water crisis due to the over-reliance on the freshwater resource and ineffective water



treatment. According to report by United Nations Educational, Scientific and Cultural Organization (2023), water scarcity problem become common and estimates 1.7 to 2.4 billion of city dwellers will encounter water shortage issues. One of the reasons are that increasing volume of greywater with less contaminated are discharged to mix with polluted wastewater and thereby water pollution is further deteriorated. Therefore, prudent use of water and recyclability of domestic wastewater is deemed as one of workable alternatives in achieving sustainability of water supply particularly in the arid and rural areas.

Apart from that, greywater quality is generally varied dependent on the water sources and household activities. The common composition in greywater includes bleaches, detergents, filler, softener, suspended solids like hairs and fibers and dye. Alkalinity of laundry greywater is obviously high which containing high pH value of 9.3 to 10 due to the presence of high concentration of bleach and sodium-hydroxide based soaps. In recent years, greywater reuse system is promoted in some water conscious countries including Australia and United States to save more water from discharging into sewers. For an instance, collected greywater is reused in some water-demanding activities either potable or non-potable purposes such as toilet flushing. However, laundry greywater cannot be reused for irrigation purpose before properly treated due to the presence of harmful chemical compositions and possible contaminated with heavy metal (Oteng-Peprah et al., 2018). It implies that relatively less amount of greywater has been reused but direct discharge to sewage system and further increases polluted water which more difficult to be treated.

Recently, health studies on greywater are kept increasing due to adoption of greywater reuse system in some countries located in semi-arid regions, and areas that encountering water scarcity or drought problems. However, untreated greywater may pose to potential health risk and unsafe to ingest. This is due to the reason that greywater is mainly generated from kitchen and laundry activities, deem as another pathway of transmitting diseases for person who ingested infected greywater without and even cause death. The bacteria in the greywater might originate from contamination food residues, contaminants attached on clothing, and cross-contamination with toilet water due to leaks or improper plumbing connection. According to Oteng-Peprah et al. (2018), microorganisms, pathogenic bacteria such as

Salmonella and Campylobacter, protozoa and helminths can be found in greywater, in addition of greywater is possible to be contaminated with faecal matters if poor personal hygiene and bad management of greywater disposal. Not only that, the detected pathogenic Escherichia coli, enteric viruses, and enteroviruses in greywater from laundry source is diagnosed as main factors of causing waterborne diseases and reduce reusability of greywater (O'Toole et al., 2012).

Nowadays, greywater is highly contaminated and no longer appropriate to reuse for agricultural irrigation and other potable water-demanding activities by considering public health concerns and its contamination level. According to Ong et al. (2019), biological systems such as up-flow anaerobic sludge blanket system (UASB), membrane bioreactor (MBR), and rotating biological contractor (RBC) are usually applied for biosolids and sludge removal. Physical system like filtration and sedimentation process is conducted as primary treatment to reduce suspended solid concentration that possible to lead to pathogen formation. Chemical Systems such as coagulation, flocculation, and magnetic ion exchange resin technology has been implemented in the final stage of treatment. Recently, advanced oxidation processes that involves hydroxyl radical ( $\text{OH}\bullet$ ) generation such as homogenous and heterogenous photocatalytic oxidation-reduction process (catalysis + light), photolysis (UV light +  $\text{H}_2\text{O}_2$ ), Fenton ( $\text{Fe}^{2+}$  +  $\text{H}_2\text{O}_2$ ) and photo-Fenton (solar light + Fenton), sonolysis (ultrasounds), ozonolysis ( $\text{O}_3$ ), and hydrothermal and wet oxidation technologies (reaction with water at elevated high temperature) (Barışçı, 2018; DEMİR & AKTAŞ, 2022). The application of photocatalytic degradation of pathogen in presence of ultraviolet (UV) light is more efficient as compared to disinfection process. In spite of photocatalysis can be either homogenous or heterogenous to produce hydroxyl radical, however, heterogenous catalytic process is preferable by considering reusability of photocatalyst and efficiency of separation process. Because it is easier to separate if the reacting species present in difference physical states, solids, or liquid phase (Devi et al., 2022).

In general, heterogeneous photocatalysis is driven by semiconductor materials activated through exposure to light. Indeed, photocatalyst is leveraged to promote oxidation-reduction reactions, especially targeting the degradation of organic

pollutants and inactivation of pathogenic bacteria. Photocatalyst with outstanding light-absorbing properties is selected. Light energy is absorbed for excitation of electrons from the valence band to higher energy level, creating electron-hole pairs. Reactive oxygen species (ROS), namely hydroxyl radical (OH•) and superoxide radical ( $\bullet\text{O}^{2-}$ ) species are generated from oxidation reaction that function to initiate the breakdown of organic pollutant and decomposition of contaminants. Furthermore, semiconductor materials are favourable catalyst in heterogeneous photocatalysis owing to their stable mechanical and chemical properties, high resistance to poisoning and attrition, and reusability and non-selectivity as applicable in various working conditions. Its prominent electronic properties help to drive redox reactions under sunlight irradiation more efficiently, the specific energy bandgap structure exhibits broad spectrum of light absorption to absorb more light energy and therefore expand the range of photons that is capable of driving photocatalytic reactions (Kumar et al., 2021). Not only that, but semiconductor materials also provide the flexibility of tailoring its properties through adjustment or modification in terms of composition, synthesis method, energy bandgap, and doping, for sake of achieve the optimum performance of photocatalytic degradation.

## 1.2 Problem Statement

The global water crisis is becoming severe, and it is mostly caused by water scarcity, pollution problem, rapid population growth, and climate change. The increasing demand of water resource to meet the basic needs of growing population, urbanization, and industrialization is considered insufficient and further deteriorate water shortage scenario in the future if alternative sources haven't been discovered. From the perspective of environmental impacts, ecosystem degradation is certainly induced such as habitat degeneration and disruption in ecological balance if water scarcity can be mitigated shortly. Greywater resource is one of the best alternative water resources to alleviate this problematic issue due to its low content of organic content which approximately 30% and low nutrient content of less than 20% such as phosphorus and nitrogen element (Oh et al., 2018). *Escherichia coli* (*E. coli*) is known as a type of coliform bacteria that is commonly detected in untreated or inadequately treated light greywater. Although this bacterium itself is not fatal or harmful to human, but its presence in domestic wastewater implies the existence of waterborne pathogens that is

possible to induce waterborne diseases such as gastrointestinal illness. Hence, it is essential to treat the light greywater and reduce its concentration of *E. coli* below 10 CFU/100ml. According to Oteng-Peprah et al. (2018) and Morel and Diener (2006), the average ratio of BOD<sub>5</sub>/COD detected in greywater is in range between 0.31 and 0.71 and it indicates high biodegradability.

Indeed, Synthetic dye is known as soluble organic compounds and can be categorized into reactive, direct, disperse, acid and basic dyes (Shindhal et al., 2020). Presence of synthetic dye such as Rhodamine B and Malachite Green. Colored textiles will also discharge dye residues into laundry water. The conventional treatment of wastewater containing synthetic dye is usually not efficient due to its high durability and solubility in water. In general, application of reactive dye for coloring cellulosic fibers become pervasive and it is expected to increase with time. These dyes compose of complex aromatic functional group like azo and anthraquinone as chromophores, the degree of fixation to cellulose textiles is decreased once these reactive dyes are hydrolyzed to certain point, and eventually increasing volume of dyes are discharged into laundry waster and further enhance the difficulty of wastewater treatment (İlkiz et al., 2021). Yet, the higher the concentration of detergent increase the pH value of water results in acceleration of breakdown of covalent bond between dyes and textiles if under alkali condition. As a result, BOD and COD value, total organic carbon (TOC) total suspended solids (TSS) concentration in greywater is boosted to higher level (Cai et al., 2016; Fijan et al., 2008).

Nowadays, the most efficient techniques that applied for organic pollutant degradation in wastewater are advanced oxidation processes (AOPs), which operates through generation of highly reactive species including hydroxyl radicals and superoxide anion radicals to trigger the oxidative degradation of organic pollutants (Lam et al., 2012). Among this technology, Fenton oxidation process and heterogeneous photocatalysis are widely utilised in wastewater treatment. However, heterogenous photocatalysis is a promising strategy which are more advantageous and sustainable compared to Fenton oxidation process. This can be attributed to several reasons. Firstly, Fenton oxidation process is pH-dependent, it requires acidic environment with pH range within 3 to 4 in order to achieve its optimized performance. Secondly, iron oxide sludge precipitation ( $\text{Fe}(\text{OH})_3$ ) is considered one of the

drawbacks of the Fenton applicability because it creates sludge-management issue and often requires additional handling and disposal measures to resolve the generated residues (Ayoub, 2022). Thirdly, semiconductor materials utilised in heterogenous photocatalysis has appeared tremendous superiority in removal of organic pollutants such as low cost, non-toxicity, and high flexibility in various operating conditions without incurring significant loss in photocatalytic activity. Since heterogeneous photocatalysis is capable of driven under the sunlight irradiation which comprised of 42% visible light and 5% ultraviolet light and therefore heterogenous photocatalysis is favourably applied in Malaysia owing to its tropical climate and substantial amount of sunlight are free and available to initiate photocatalysis (Lam et al., 2012).

In recent years, Bismuth tungstate ( $\text{Bi}_2\text{WO}_6$ ) is an n-type semiconductor, a member of ternary Aurivillius oxide which gained a lot of attention in wastewater treatment owing to outstanding photocatalytic degradation of organic contaminants on its relatively large surface area and high crystallinity (Liu et al., 2015). Although  $\text{Bi}_2\text{WO}_6$  is well-known for its relatively small band gap of approximately 2.7eV, high chemical and thermal stabilities which considered it as ideal candidate for visible-light photodegradation. However, its relatively narrow visible-light adsorption range, poor efficiency of carrier separation and weak reduction ability which adversely affect superoxide radicals' generation, therefore these drawbacks has impeded  $\text{Bi}_2\text{WO}_6$  as single catalyst in real-world application (Wang et al., 2022).  $\text{Bi}_2\text{WO}_6$  has narrow bandgap properties incurs high recombination rate of electron-hole pair separation and limits the maximum visible light utilization. It is essential to implement some efficient modifications to get rid of these weakness by coupling with other stable semiconductor materials or support materials with suitable bandgap potential that capable of excited by visible light with broader visible-light adsorption range.

There are various approaches can be applied to ameliorate photocatalytic efficiency of  $\text{Bi}_2\text{WO}_6$  including morphology control, metal and non-metal element doping, defect introduction, and coupling of two compatible semiconductor photocatalyst for heterojunction construction. In this study, it is more feasible to generate novel ternary composite material with Z-scheme heterojunction which provides more effective charge separation as well as high redox potential and consequently, improves to higher photocatalytic activity.  $\text{Bi}_2\text{WO}_6$ -based

heterojunction photocatalyst incorporates with other highly compatible semiconductor materials could also enhance the visible-light response of ternary composite material (Tahir et al, 2021). According to Zhang et al. (2021), Tin Ferrite ( $\text{SnFe}_2\text{O}_4$ ) is a preferable choice owing to their eco-friendly nature and cost-effective. Since  $\text{SnFe}_2\text{O}_4$  is mainly constituted by Sn and Fe, which abundant in nature and yet it has an attractive direct bandgap of 2.53 eV allow this monomer photocatalyst having considerably great visible light responsiveness (Lee & Lu, 2015). The unique magnetization nature at room temperature offers magnetic retrievability and recyclability indicates it is a promising candidate in wastewater treatment process (Li et al., 2022). Nanoparticles structure of Sn results in great pore number and high specific surface area exposed for photocatalytic performance of organic pollutants (P & Seetharaman, 2022). According to Ma et al. (2023), incorporation of  $\text{Bi}_2\text{WO}_6$  with  $\text{SnFe}_2\text{O}_4$  can efficiently lead to formation of Z-scheme system which decreases recombination rate of photogenerated electron-hole pairs, associated with greater redox capacity and therefore ameliorates the photocatalytic efficiency of semiconductor composite. In addition, hydroxyapatite (HAp) is a naturally earth-abundant inorganic functional insulator material which can be synthesized from natural resources such as eggshells, fishbones, bovine bones, and mussel shells. It generally has a relatively wide energy bandgap of 6eV and superior properties including high chemical and thermal stability (Lv et al., 2024). Since HAp is environmental friendliness and inexpensive, it gains attention to modify their compositions so enables perform visible light driven photocatalytic reaction through lowering their energy band gap that corresponds to visible light photons. High porosity nature of HAp constitutes a photoactive support which provides higher specific surface area available for particles attachment, result in maximizing the adsorption of organic pollutants for photocatalytic degradation. To the best of our knowledge, there is no detailed research on photodegradation of Malachite Green (MG) dye using  $\text{SnFe}_2\text{O}_4/\text{Bi}_2\text{WO}_6$  in other literatures. Therefore, in this work, novel  $\text{SnFe}_2\text{O}_4/\text{Bi}_2\text{WO}_6/\text{HAp}$  ternary nanocomposite material is synthesized and determine its efficiency for MG degradation and wastewater treatment under sunlight irradiation. The Z-scheme heterojunction of  $\text{SnFe}_2\text{O}_4/\text{Bi}_2\text{WO}_6/\text{HAp}$  is proposed for visible-light drive photocatalytic reaction of MG degradation and greywater treatment (Mohammad et al., 2022).

### 1.3 Objectives

There are three main objectives aimed to be achieved in this research project, which are,

- i) To synthesize  $\text{SnFe}_2\text{O}_4/\text{Bi}_2\text{WO}_6/\text{HAp}$  ternary Z-scheme heterojunction photocatalyst via a solvothermal-deposition method.
- ii) To characterize the physical, chemical, optical, and electronic properties of synthesized  $\text{SnFe}_2\text{O}_4/\text{Bi}_2\text{WO}_6/\text{HAp}$  photocatalyst.
- iii) To investigate the effectiveness of as-fabricated  $\text{SnFe}_2\text{O}_4/\text{Bi}_2\text{WO}_6/\text{HAp}$  photocatalyst on the photocatalytic Malachite Green-containing greywater effluent treatment and antibacterial applications.

### 1.4 Scope of Study

$\text{SnFe}_2\text{O}_4/\text{Bi}_2\text{WO}_6/\text{HAp}$  Z-scheme heterojunction photocatalyst was produced using a solvothermal-deposition method with various HAp loading amounts. Following that, the as-synthesized powdered photocatalysts underwent a range of characterization techniques such as X-ray Diffraction (XRD), Field Emission Scanning Electron Microscopy (FESEM), Attenuated Total Reflectance – Fourier Transform Infrared Spectroscopy (ATR-FTIR), Ultraviolet-visible Diffuse Reflectance Spectroscopy (UV-vis DRS), Transient Photocurrent Response (TPR), Electrochemical Impedance Spectroscopy (EIS), Mott-Schottky (M-S), and cyclic voltammetry (CV) analysis. Photocatalytic degradation efficiency of dyes including Malachite green using  $\text{SnFe}_2\text{O}_4/\text{Bi}_2\text{WO}_6/\text{HAp}$  ternary nanocomposite was investigated. The photocatalytic efficiency of the as-synthesized photocatalysts in degrading Malachite green with concentration of 5mg/L and treating greywater collected from washing machine under direct sunlight exposure was then investigated. The treated effluent will then be used again for the phytotoxicity test. Radical scavenging experiments were conducted for the purpose to identify the active species present during photocatalytic activity. Lastly, toxicity of degraded MG solution by single photocatalyst  $\text{SnFe}_2\text{O}_4$ ,  $\text{Bi}_2\text{WO}_6$ , binary photocatalyst  $\text{SnFe}_2\text{O}_4/\text{HAp}$ ,  $\text{Bi}_2\text{WO}_6/\text{HAp}$ , and ternary  $\text{SnFe}_2\text{O}_4/\text{Bi}_2\text{WO}_6/\text{HAp}$  Z-scheme heterojunction photocatalyst were assessed by *E. coli* inactivation experiment.

## CHAPTER 2

### LITERATURE REVIEW

#### 2.1 Water Pollution and Greywater

Water pollution is the migration or accumulation of contaminants, pollutants, or substances, either natural or manmade, in water bodies such as rivers, lakes, seas, and groundwater, resulting in an overall decline in water quality. These contaminants can include chemicals, heavy metals, nutrients, pathogens, and other compounds that exceed normal levels, causing detrimental effects on aquatic ecosystems, human health, and the overall use of water resources. Since water is being known as universal solvent and thereby its ability to dissolve wide range of substances generated from agriculture activities, urban areas, and industrial operations result in more susceptible to pollution. Water pollution can be classified into two types, namely point source pollution and non-point source pollution. For point source water pollution is referred to as the deliberate discharge of pollutants or toxic substances into water bodies from a single, identifiable source, such as industrial facilities, wastewater treatment plants, or pipes. In this scenario, the pollution may be traced back to a specific area or facility, distinguishing it from non-point source pollution, which is caused by diffuse and extensive sources such as agricultural runoff or urban stormwater. Point source pollution occurs when pollutants such as chemicals, fertilisers, heavy metals, or pathogens are released directly into rivers, lakes, or other bodies of water via independent outlets, enabling focused regulatory measures and mitigation efforts at the recognised source. In the contrast, non-point source can be summarised as discharge of contaminants originated from undefined non-specific and unidentifiable



discharge point which is difficult to trace the origin directly (Denchak, 2023).

Sewage is considered as the main contaminated wastes discharged into aquatic system which comprised of industrial wastes, municipal wastes, and domestic waste that generated from industries, urban area, and household (Das & Acharya, 2003). According to Bashir et al. (2020), approximately 58% of wastewater produced from metropolitan areas and 81% of industrial effluents are dumped directly into water bodies without properly treated and end up with the scenario of contaminating around 73% of water bodies. The spillage of sewage undoubtedly jeopardizes water pollution and at the meantime, the clean water resource has been depleted. Owing to presence of nutrient pollutant load and organic substances in sewage, the dissolved oxygen (DO) concentration is one of main criteria in determination of maltreated wastewater. The higher the BOD, the more severe of the pollution problem due to high concentration of organic pollutants present in the receiving water. According to Smith et al. (2016), when the population grows, consumption of water will be increasingly reliant on renewable surface water, which presently provides more than half of all drinking water worldwide. In Malaysia, water crisis is reflected to everywhere and this circumstance can be said induced by rapid pace of urbanisation and industrialization practices. Clean water shortage problem is interrelated to water pollution, because it originates from numerous kinds of human actions and influences from the environment. For instance, industrial discharges, agricultural runoff such as pesticides and fertilizers, untreated sewage, and inappropriate waste disposal may pollute rivers, lakes, and groundwater sources. This contamination results in water quality degradation, reducing safe and clean water availability for household, agricultural, and commercial uses. Nevertheless, surface water has been contaminated by sewage effluent containing various types of harmful microorganisms is applied for domestic and other purposes which might outcome in the dissemination of waterborne illnesses (Bashir et al., 2020). Table 2.1 depicts some of the common microorganisms that potentially detected found in sewage effluent.

As increasing challenging issues arouse in terms of water scarcity, pollution problem, and water control, Malaysia government and policymakers enacted and implemented stricter environmental control and water resource policies such as Environmental Quality Act 1974 (EQA) to halt the deterioration of inland pollution

and industrial water pollution. Although Malaysia currently kept struggling for achieving the United Nations Sustainable Development Goal 6 (SDG 6), however, phenomena of increasing clean water demand reflected in imports, drinking water service have not yet attained basic standards, and additional treatment required for treating anthropogenic wastewater clearly embody more effort are needed for realization (Ismail et al.,2023). According to Loi et al. (2022), the temporary closed of water treatment facilities in Selangor owing to violation of raw water quality standards and yet ten out of thirteen occurrences resulted in water outages, affecting up to 1.14 million residents live in that state. This case embodies it are essential to enhance pollution preventive methods and control to minimize the frequency of water supply disruption by effectively managing the contaminants level below the stipulated standard limits.

**Table 2.1 shows Microbial illnesses connected with polluted waters (Bashir et al., 2020).**

Types	Species	Diseases incurred
Bacteria	<p>“<i>E. coli O157:H7</i>”</p> <p>“<i>Escherichia coli</i>”</p> <p>“<i>Salmonella sp.</i>”</p> <p>“<i>Vibrio Cholera</i>”</p>	<p>“Bloody diarrhoea, haemolytic uremic syndrome”</p> <p>“Gastroenteritis”</p> <p>“Salmonellosis, gastroenteritis, diarrhoea”</p> <p>“Cholera”</p>
Protozoa	<p>“<i>Balantidium colis</i>”</p> <p>“<i>Cryptosporidium Parvum</i>”</p> <p>“<i>Cyclospora cayetanensis</i>”</p>	<p>“Balantidiasis”</p> <p>“Cryptosporidiosis”</p> <p>“Persistent diarrhoea”</p>
Viruses	<p>“<i>Poliovirus</i>”</p> <p>“<i>Hepatitis A and E</i>”</p> <p>“<i>Norovirus</i>”</p>	<p>“Respiratory disease &amp; eye infections”</p> <p>“Gastroenteritis”</p> <p>“Infectious hepatitis”</p>

Greywater is contributed to 43% to 70% of total domestic wastewater volume, such large quantity with low contamination level is considered as alternative source of clean water supplies to cope with water shortage and subsequently road to water sustainability in metropolitan areas. Initially, greywater is treated and utilised as

freshwater substitute for non-potable applications, assist in minimizing freshwater consumption, as well as tackle global water scarcity. It can lead to a result of saving up to 50% of fresh water for toilet flushing and gardening activities (Oh et al.,2018). Table 2.2 shows the standards of treating greywater in some countries. As looking into Table 2.2, it can be extrapolated that all countries that implementing greywater treatment have very high requirement on the concentration of organic contaminants and yet turbidity and total suspended solid are crucial for regulating quality of treated greywater before release. However, currently there is no any water quality standards for treated greywater are implemented by Department of Environment (DOE).

According to the statistics, among 1792 families living in Malaysia were investigated and result in potable water consumption at rate of around 0.226 m<sup>3</sup> per person per day (m<sup>3</sup>/p/d) and interestingly approximately 67% of total amount drinkable water have been utilized for toilet flushing, showering, and laundry washing (FOMCA, 2010). It is essential to expand the water source for sake of promoting water security. Nevertheless, warning given by United Nations provides insight of relying solely on river as water supply could not be able to cope with forthcoming water scarcity owing to rapid climate change and population expansion by 2030 (FOMCA, 2017). The use of wastewater including greywater is prevalent around the world however, mostly wastewater do not undergo adequate treatment or other safeguards to protect human and environmental health which lead to the death of almost 1 million people suffering from waterborne diseases such as diarrhea (WHO, 2023).

**Table 2.2 shows standard of treated greywater in some developing and developed countries. (Oh et al., 2018).**

Parameter (s)	Unit	Australia	Israel	USA	Italy	New South Wales	UK	Canada
pH	-	-	-	6 to 9	6 to 9.5	-	5 to 9.5	-
TSS	mg/L	<30	<10	-	<10	<20	-	<20
Turbidity	NTU	-	<100	<2	-	2	<10	<5
COD	mg/L	-	<10	-	<100	-	-	-
BOD	mg/L	<20	-	<10	<20	<20	-	<20
Total N	mg/L	-	-	-	<15	-	-	-
Total P	mg/L	-	-	-	<2	-	-	-
Cl <sub>2</sub> residual	mg/L	-	-	>1	-	2	<2	>0.5
<u>E.Coli</u>	cfu/100ml	-	-	-	<10	-	-	-
Thermotolerant coliforms	cfu/100ml	<10	-	-	-	-	-	-
Faecal coliforms	cfu/100ml	-	-	N.D	-	<1	1000	<200

## 2.2 Review on Dye and compositions in Household Greywater

Dye-containing wastewater poses substantial problems to both wastewater treatment operations and the environment due to the intricate makeup of dye compounds and their potential detrimental effects. The negative consequences are far-reaching, including treatment efficacy, environmental sustainability, and ecosystem risk. In the past decade, dyes are widely employed in numerous kinds of industries, notably textile, paper, printing, plastic, cosmetic, and food production. The textile sector ranks the tops among all industries in terms of applying dyes for fiber colorization. According to Drumond Chequer et al. (2012), there are more than  $1 \times 10^4$  different kinds of dyes and pigments have been applied widely in industries and  $7 \times 10^5$  tons of synthetic dyes were generated annually in the world and yet the discharge of used dyes to wastewater effluent can reach up to  $2 \times 10^5$  tons during the dyeing and finishing processes. In present, the annual production of synthetic dyes is significantly increased and currently production is approximately  $7 \times 10^7$  tons per annum, more interestingly over than  $1 \times 10^4$  tons volume of dyes have been extensively utilized in textile industries (Al-Tohamy et al., 2022). The global textile market was estimated at USD 993.6 billion in 2021, and that figure is expected to continue expanding at a 4% CAGR from 2022

through 2030. Yet, Malaysia's clothing market is estimated to generate approximately USD 5.2 billion in revenue by 2023, with a projected growth rate of over four percent through 2027 (MIDA, 2023). It implies that more dyes are ready to be produced from textile industries in order to cater the increasing market demand due to rapid population growth.

In common, wastewater effluent containing synthetics dyes is the main contaminating contributor to water bodies. Owing to the complicated chemical processes, synthetic dyes are generally formed using hazardous and toxic chemicals, which provides the properties such as high temperature and chemical stabilities (Forgacs et al., 2004). Complicated chemical functional groups of synthetic dyes including azo, anthraquinone, sulphur, indigoid, triphenylmethyl, xanthene, phthalocyanine derivatives contains aromatic rings or double bonds conjugated systems makes it recalcitrant to biodegradation or can be said as resistant to microbiological attack (Przystaś et al., 2011). Due to high chemical stability of these contaminants, conventional wastewater treatment processes have been discovered to be extremely poor in dealing with synthetic textile dye effluent (Rodríguez Couto, 2009). The existence of minimal amounts of dyes which could less than 1 mg/L for certain dyes in water makes it extremely visible, influencing the aesthetic quality, water transparency, and dissolved oxygen concentration (DO) in rivers, lakes, and other bodies of water, ultimately resulting in degradation of the aquatic ecosystem (Wijetunga et al., 2010). In the past, different kinds of wastewater treatment technologies have been evaluated for sake of decolourisation and dye-containing wastewater such as textile wastewater. Conventional treatment technologies can be classified into biological (aerobic, anaerobic, biodegradation, activated sludge), physical (adsorption, membrane separation, ion exchange) and chemical processes (ozonation, Fenton) (Liu & Wang, 2024). Nevertheless, the synthetic dyes are also constantly upgraded with time and substituted with superior chemical substances that have enhanced fastness, stability, brightness, and ability to resist natural deterioration from sunshine and microbes (Wijetunga et al., 2010). Therefore, biological treatment processes are solely efficient for biodegradable organic compounds and ineffectual in eliminating non-biodegradable and recalcitrant organics, which implies that complicated molecular structures of synthetic dyes are difficult to break down by microbial degradation. Because synthetic dyes' slow decomposition rates make it

difficult for microorganisms to break it down during the standard biological treatment residence period, superadd microbial reproduction and reaction rate of biological methods are relatively low to catch up (Liu et al., 2022).

Greywater is the sewage generated from various home activities that excludes considerable amounts of faecal matter as well as is produced from sources such as sinks and showers, bathtubs, and washing machines (Oron et al., 2014). According to Liu et al. (2010), Biochemical Oxygen Demand (BOD) of greywater is generally within the range of 33 to 466 mg/L and more interestingly, prolonged residence time in the reservoir could promote microbial re-growth and consequently result in the decline of water quality. However, in some countries where facing water deficiency, local government have made greywater recycling obligatory for newly built constructions in order to achieve water sustainability (Matos et al., 2020). Greywater can be classified into two types, namely light greywater, and dark greywater according to the presence of pollutants' contamination level in that source. Dark greywater is generated from laundry washing and washing machines while light greywater is source from shower and bathtub (Alsulaili & Hamoda, 2015). In general, greywater from laundry machine comprise of detergents, oils, solvents, surfactants, synthetic dyes, bleaches, and non-biodegradable fibres from clothes. Presence of bacteria and viruses in greywater are originated from dirty clothing while high amount of laundry detergent added induces high chemical concentration, oxygen demand, suspended solid as well as high turbidity level. As synthetic dyes generally contain heavy metal which could lower the biodegradability of greywater (Shaikh & Ahammed, 2020). The greywater characteristics of some different countries which divided into high-income and low-income countries have been shown in Table 2.3. As Malaysia is still considered as developing country and therefore from Table 2.3, high-income countries generally produce greywater with low contamination levels as compared to low-income countries. This could be attributed to well-planned and advanced infrastructure for wastewater management as well as more stricter wastewater discharge standards. Although Malaysia do not have clear environmental rules and regulations pertaining to greywater discharge to water bodies, however Department of Environment (DOE) under the Ministry of Environment and Water has established the certain criteria must comply being discharged. The industrial effluents standards are divided into two classes namely, standard A and standard B and shown in Table 2.4. Standard A applies

to wastewater discharge into any inland waterways within the sensitive areas outlined in the Environmental Quality Act's Sixth Schedule, whereas Standard B applies to any other inland waters or Malaysian waters where are considered fewer sensitive zones (Department of Environment, 2009). According to specification, synthetic dyes colour intensity should be controlled below 100 ADMI\* and 200 ADMI\* listed in Standard A and Standard B, respectively. While for aspect of BOD, it should not exceed 20 mg/L and 50 mg/L in Standard A and B, respectively to ensure low organic pollutants content in treated greywater.

**Table 2.3 shows Greywater characteristics of low-income countries (LIC) and high-income countries (HIC) (Shaikh & Ahammed, 2020).**

Source	Country	LIC/LHC	pH	TSS (mg/L)	BOD (mg/L)	COD (mg/L)	TN (mg/L)	TP (mg/L)	TC (CFU/100mL)	FC (CFU/100mL)	E. coli (CFU/100mL)
Bathroom	Malaysia	LIC	6.30-6.73	101-	81-271	251-508	-	-	-	-	2.5x10 <sup>4</sup> -6.1 x10 <sup>5</sup>
	Brazil	LIC	-	206	156	273	50.3	5.3	4.0x10 <sup>5</sup>	-	5.1 x10 <sup>4</sup>
	Greece	HIC	7.50	156	74	390	2.7	0.1	-	-	-
	Spain	HIC	7.20-8.30	74	-	-	11.0-36.0	0.8-15.0	-	-	8.0 x10 <sup>1</sup> -4.4 x10 <sup>5</sup>
Hand Basin	Brazil	LIC	6.72-9.82	-	-	47-350	-	-	0.0-1.7 x10 <sup>6</sup>	-	-
	Jordan	LIC	-	-	-	263	9.6	2.6	-	-	-
	Portugal	HIC	7.10-7.50	40-141	40-141	76-287	-	0.3-1.3	-	-	-
	UK	HIC	7.32	153	153	587	10.4	-	9.4 x10 <sup>3</sup>	-	1.0 x10 <sup>1</sup>
Kitchen	India	LIC	6.20	308	308	602	-	-	-	2.3 x10 <sup>2</sup>	-
	Jordan	LIC	5.58	644	644	2244	-	18.3	2.0x10 <sup>7</sup>	-	7.0 x10 <sup>5</sup>
	Greece	HIC	6.90	319	319	1119	65.0	2.7	-	-	-
	Greece	HIC	6.72	299	299	775	-	-	-	-	-
Laundry	Jordan	LIC	9.60	760	760	2500	2.8	9.0	NA	-	NA
	India	LIC	9.40	1852	1852	824	-	-	-	4.3x10 <sup>2</sup>	-
	Slovenia	HIC	9.60	-	-	280	2.8	9.9	-	-	-
	Australia	HIC	9.30-10.0	88-250	88-250	-	-	-	2.3 x10 <sup>3</sup> -3.3 x10 <sup>5</sup>	1.1 x10 <sup>2</sup> -1.1 x10 <sup>3</sup>	-
Light Greywater	India	LIC	7.13-8.53	82-256	82-256	164-424	-	-	4.6 x10 <sup>3</sup> -9.3 x10 <sup>6</sup>	2.6 x10 <sup>3</sup> -9.0 x10 <sup>4</sup>	4.5 x10 <sup>1</sup> -7.8 x10 <sup>3</sup>
	Malaysia	LIC	5.94-6.40	36-224	36-224	146-903	-	-	6.0 x10 <sup>7</sup> -1.9 x10 <sup>8</sup>	-	0.0 -5.2 x10 <sup>6</sup>
	Spain	HIC	4.90-7.90	9-195	9-195	41-535	1.3-25.5	-	1.4 x10 <sup>6</sup> -4.1 x10 <sup>6</sup>	-	0.0 -1.1 x10 <sup>6</sup>
	UK	HIC	7.20	37	37	96	-	0.9	2.2 x10 <sup>7</sup>	-	3.9 x10 <sup>5</sup>
Dark Greywater	Uganda	LIC	7.20	996	996	2861	-	2.9	6.9 x10 <sup>7</sup>	-	4.2 x10 <sup>6</sup>
	Kenya	LIC	6.20	-	-	-	-	-	7.3 x10 <sup>6</sup>	5.4 x10 <sup>5</sup>	-
	Israel	HIC	7.30	47	47	-	-	-	-	-	1.6 x10 <sup>5</sup>
	Italy	HIC	7.20	166	166	602	-	1.9	-	-	-



**Table 2.4 shows acceptable conditions for discharge of industrial effluent or mixed effluent of standard A and B (Department of Environment, 2009).**

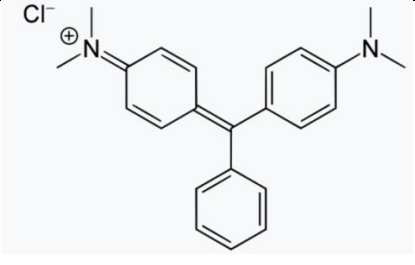
	<b>Parameter</b>	<b>Unit</b>	<b>Standard A</b>	<b>Standard B</b>
(i)	Temperature	°C	40	40
(ii)	pH value	-	6.0-9.0	5.5-9.0
(iii)	BOD, at 20°C	mg/L	20	50
(iv)	Suspended Solids	mg/L	50	100
(v)	Mercury	mg/L	0.005	0.05
(vi)	Cadmium	mg/L	0.01	0.02
(vii)	Chromium, Hexavalent	mg/L	0.05	0.05
(viii)	Chromium, Trivalent	mg/L	0.20	1.0
(ix)	Arsenic	mg/L	0.05	0.10
(x)	Cyanide	mg/L	0.05	0.10
(xi)	Lead	mg/L	0.10	0.5
(xii)	Copper	mg/L	0.20	1.0
(xiii)	Manganese	mg/L	0.20	1.0
(xiv)	Nickel	mg/L	0.20	1.0
(xv)	Tin	mg/L	0.20	1.0
(xvi)	Zinc	mg/L	2.0	2.0
(xvii)	Boron	mg/L	1.0	4.0
(xviii)	Iron (Fe)	mg/L	1.0	5.0
(xix)	Silver	mg/L	0.1	1.0
(xx)	Aluminium	mg/L	10	15
(xxi)	Selenium	mg/L	0.02	0.5
(xxii)	Barium	mg/L	1.0	2.0
(xxiii)	Fluoride	mg/L	2.0	5.0
(xxiv)	Formaldehyde	mg/L	1.0	2.0
(xxv)	Phenol	mg/L	0.001	1.0
(xxvi)	Free Chloride	mg/L	1.0	2.0
(xxvii)	Sulphide	mg/L	0.50	0.50
(xxviii)	Oil and Grease	mg/L	1.0	10
(xxix)	Ammoniacal Nitrogen	mg/L	10	20
(xxx)	Colour	ADMI*	100	200

### 2.3 Usage and Hazardous Effects of Malachite Green

Malachite Green (MG) or N-methylated diamino-triphenylmethane is known as blue-green cationic dye with chemical formula of  $C_{23}H_{25}N_2$ , this synthetic dye comprises of 3 aromatic rings that connected by carbon atoms and generally appears as chloride salt with chemical formula structure of  $C_{23}H_{25}ClN_2$  (Ahmad et al., 2024). According to Table 2.5, MG has molecular weight of 364.9g/mol and density of 1.0448g/ml. Generally, it is hard for biodegradation and lead to decline in water quality and reduce the photocatalysis activities carried out by aquatic plant (Zhang et al., 2022). The application of dyes poses environmental and health problems owing to its genotoxic and carcinogenic properties. MG dyes with minimal concentration of 1 mg/L could trigger harm and damage to humanity and animal species due to its toxicity (Sarkar et al., 2021). In common, MG dyes are widely applied in wide range of industrial production including paper, textile, jute, plastic as well as biocide in agriculture (Vergas et al., 2019). According to Sarkar et al. (2021), in many nations including European Union, United States, and Japan, MG dyes have been prohibited for aquatic species that consumed by humanity, in addition to food additives application. According to Tran et al. (2022), developing countries have not yet to restrict the use of MG dyes owing to cheaper cost and high efficiency, while developed countries have banned the industrial use of this synthetic dye. Nevertheless, MG dyes still prevalent and proceed to large-scale manufacturing and its residue form leucomalachite in fish, fish products, and water samples have been frequently inspected. MG synthetic dye is toxic towards aquatic and terrestrial creatures, therefore it has highly lethal impact on freshwater fish owing to both chronic and acute exposure and consequently incurs public health disorders (Mandale et al., 2024). When the polluted aquatic species has been consumed by human, which might trigger toxic impact on human organs such as reproductive systems, infertility, kidney, heart, and liver failure (Tiwari et al., 2023). According to Kotian et al. (2024), since MG dyes is one of popular artificial food colourant which could bring about physiological consequences include multiorgan tissue injury, chromosomal fractures, carcinogenesis, pulmonary toxicity, and teratogenicity. This synthetic dye has high degree of solubilities in water as well as organic solvents such as ethanol and methanol, thereby it could easily be detected in the wastewater discharged from textile industries. Hence, hazardous properties and detrimental impacts of Malachite Green synthetic dye, it turns out to be worthwhile to

eliminate it from wastewater effluent.

**Table 2.5 shows general properties of Malachite Green (PubChem, 2024).**

Molecular Structure	
Molecular Formula	$C_{23}H_{25}ClN_2$
IUPAC Name	4-[[4-(Dimethylamino) phenyl] (phenyl)methylidene]- <i>N,N</i> -dimethylcyclohexa-2,5-dien-1-iminium chloride
Colour Index Number	42000
Appearance	Green crystal with metallic luster
Molecular Weight	364.9 g/mol
Density	1.0448 g/mL
Melting Point	158-160°C
Solubility	Soluble in alcohol, methanol, amyl alcohol, ethanol, water

## 2.4 Heterogenous Photocatalysis

Heterogeneous photocatalysis has gained importance primarily due to its effectiveness in environmental clean-up. It is widely used to break down organic pollutants, which include pigments, herbicides and other industrial toxins, providing ecologically sound and environmentally friendly techniques for wastewater treatment. According to Friedmann (2022), the application of heterogeneous photocatalysis with the use of sunlight to trigger photodegradation of organic pollution in wastewater is considerably economically viable as compared with advanced oxidation processes such as ozonation. Extensive researches and articles pertaining to photocatalytic degradation of organic contaminants were published over the few past decades due to its capabilities of removing a wide range of dangerous pollutants including infectious microbes and heavy metals (Wang et al., 2022). Stabilities and reusability of photocatalyst have been extensively studied in recent years and photo-corrosion should be resolved to secure the photo-oxidation performance of heterogenous catalyst. These two parameters are mainly influenced by synthesis approaches, process temperature, and crystallinity of photocatalyst (Kongsuebchart et al., 2006). Besides, expenses of wastewater treatment and photocatalytic degradation efficiency can be positively affected if high stability and reusable photocatalyst is utilized (Subash et al., 2013). Yet, mechanism of photocatalysis could be briefly stated in this way: initially the energy of sunlight that surpasses bandgap energy strikes on semiconductor-based photocatalyst's surface, induce the electron-hole pairs formation. Movement of electron from valance band (VB) to conduction band (CB), generating positive hole at VB. Reaction of excited electrons in CB and holes in VB the with oxygen and water to form superoxide as well as hydroperoxide radicals, respectively. Redox reaction occurs, reduction is carried out with excited electrons while organic pollutants are oxidised by holes simultaneously to degrade contaminants. Reaction of adsorbed water molecules and photogenerated holes results to hydroxyl radicals' formation to oxidise targeted molecules (Wang et al., 2022).

In photocatalytic degradation system, semiconductor materials are the most common types that being used as catalyst, which can be either organic or inorganic materials. In Although semiconductor-based photocatalysts might encounter low utilization of sunlight on catalyst surface for high photocatalytic activity, but

undoubtedly, the benchmark semiconductor materials such as titanium dioxide ( $\text{TiO}_2$ ) and zinc oxide ( $\text{ZnO}$ ) are resistant to photo-corrosion, cost effective, non-toxicity, chemically inert, long-term high stabilities, environmentally friendly, and readily available (Karim et al., 2022). In fact, there are several core properties that significantly influence the performance of semiconductor photocatalyst, namely (i) bandgap energy which refers to the gap between valence band minimum ( $E_{\text{VB}}$ ) and conduction band maximum ( $E_{\text{CB}}$ ), (ii) band edge positions of  $E_{\text{CB}}$  and  $E_{\text{VB}}$ , (iii) interactions of charge carriers including photogenerated carriers' recombination rates, mobility, lifespan, interfacial charge transfer, and diffusion length. Referring to Figure 2.1, semiconductor-based photocatalyst with bandgap energy of more than 3eV merely receptive towards UV light while for others photocatalysts with narrower bandgap tend to sunlight absorption. To critically emphasize,  $E_{\text{CB}}$  ought to be higher than reduction potential so that semiconductor has greater tendency to receive electrons and perform reduction reaction ( $A + e^- \rightarrow A^-$ ), while  $E_{\text{VB}}$  value should lower than oxidation potential to promote the oxidation of electron donor ( $D + h^+ \rightarrow D^+$ ). Therefore, the movement of charge carriers play significant role in maximizing the performance of photoinduced processes under the sunlight irradiation, at the meantime decrease electron-hole pairs recombination rate and conduct redox reactions (Tan et al., 2019).

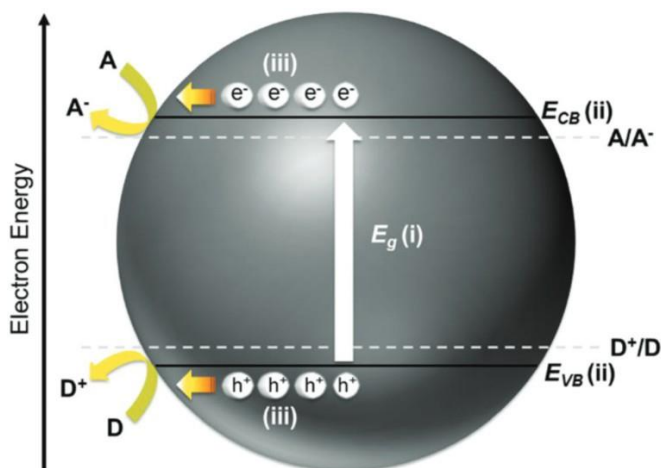


**Figure 2.1 shows redox reactions (Oxidation and reduction) on semiconductor photocatalyst (Tan et al., 2019).**

## 2.5 Bi<sub>2</sub>WO<sub>6</sub> as Photocatalyst

Bismuth-based photocatalyst has garnered attention in last few decades because of their distinctive characteristics and outstanding efficacy across multiple photochemical uses. For an instance, bismuth-based semiconductors such as bismuth molybdate (Bi<sub>2</sub>O<sub>3</sub>•nMoO<sub>3</sub>), bismuth oxyhalides (BiOX, where X can refer to halogen including fluorine and chlorine), bismuth oxide (Bi<sub>2</sub>O<sub>3</sub>), and bismuth vanadate (BiVO<sub>5</sub>), bismuth tungstate (Bi<sub>2</sub>WO<sub>6</sub>). According to Table 2.3, BiVO<sub>4</sub>, Bi<sub>2</sub>MoO<sub>6</sub>, BiFeO<sub>3</sub>, and BiMnO<sub>3</sub> are visible-light responsive catalyst, therefore, bismuth-based compounds are widely applied in photodecomposition, sustainable energy production including water splitting and carbon dioxide reduction techniques, and airborne pollutants neutralization. Among these mentioned photocatalysts, Bismuth tungstate, Bi<sub>2</sub>WO<sub>6</sub> has gained a lot of interest for its exceptional photocatalytic performance under visible light irradiation, distinctive layered structure, robust photochemical reactions, high thermal stability, and ecological sustainable (Li et al., 2024). Bi<sub>2</sub>WO<sub>6</sub> is one of the popular semiconductor materials that have been classified as an Aurivillius oxide owing to its properties of structure which closely resemble the fundamental formula of Aurivillius phase. Bi<sub>2</sub>WO<sub>6</sub> comprised of alternating perovskite-like layered structure as well as bismuth layers (Bi<sub>2</sub>O<sub>2</sub>). General formula of this n-p type semiconductor is Bi<sub>2</sub>A<sub>n-1</sub>B<sub>n</sub>O<sub>3n+1</sub>, in which both of A and B represents the particular elements found in the periodic table. As symbol A refers to alkaline earth metal or rare earth metal such as Bismuth (Bi), Sodium (Na), Calcium (Ca), Barium (Ba), and Potassium (K), while symbol B is defined as transition metal elements including Tungsten (W), Iron (Fe), Titanium (Ti), and Tantalum (Ta). In this case, Bi<sub>2</sub>WO<sub>6</sub> containing elements of Bi, W, and O (Bismuth, tungsten, and oxygen, respectively) is generated through the interaction between alternating fluorine-like bismuth oxide [Bi<sub>2</sub>O<sub>2</sub>]<sup>2+</sup> ionic layered sheets as well as octahedral tungsten oxide [WO<sub>4</sub>]<sup>2-</sup> ionic layers where it contains as-mentioned metal elements to facilitate the formation of “n” perovskite-like layers as shown in Figure 2.2 (b) (Elaoui et al., 2023). This interaction between layers form three polymeric phases where provides large surface area and active sites ready for adsorption process with targeted species. In short, the distinctive sandwiched structure brings about positive impact on charge carrier separation and decrease recombination rate, further maximize its photodegradation activities.

In general, hybridization of Bi 6s and O 2p orbitals at valence band (VB) maximum shown in Figure 2.2 (c), induce narrow bandgap among bismuth-based photocatalyst. Due to its relatively narrower gap of approximately 2.8eV and visible light absorption range at around 470 nm, allow this material capable of capturing a wider range of solar spectrum. The decrease in bandgap of Bi<sub>2</sub>WO<sub>6</sub> is attributed to a greater percentage of hydrogen-related defects. These imperfections result the creation of cationic vacancies levels on the VB level, thereby lowers the CB level. Narrow bandgap which lower than 3 eV allows the absorption of visible light which account for 42% to 43 % of solar spectrum, maximize the photocatalytic performance of organic pollutants by harvesting large amount of energy. According to Gordanshekan et al., Bi<sub>2</sub>WO<sub>6</sub> is considered as one of promising photocatalyst on carbon dioxide (CO<sub>2</sub>), dye degradation, and hydrogen gas (H<sub>2</sub>) synthesis. As compared with the earlier well-known catalysts such as titanium dioxide (TiO<sub>2</sub>) and zinc oxide (ZnO) has limited practical applications because of its pristine material has relatively wide bandgap of 3.2 eV and 3.37 eV, respectively. (Madhusudan Reddy et al., 2003; Jafarova & Orudzhev, 2021). The large bandgap indicates these catalysts have relatively restricted photo-response spectrum. Hence, Bi<sub>2</sub>WO<sub>6</sub> exhibits its outstanding photocatalytic activity compared to TiO<sub>2</sub> and ZnO as visible light is the primary source of energy for Bi<sub>2</sub>WO<sub>6</sub> while TiO<sub>2</sub> and ZnO are primarily responsive depending on ultraviolet (UV) light.

More interestingly, some interesting properties such as piezoelectricity, ferroelectricity, and non-linear dielectric susceptibility are significant on determining the practical applications and versatility of photocatalyst. Piezoelectricity refers to capability of photocatalyst to produce electrical charges as outcome of mechanical stress or deformation. Ferroelectricity is related to tendency of materials to produce spontaneous electrical polarisation which is susceptible to reverted via an outside magnetic field. While non-linear dielectric susceptibility implies polarisation responses cannot be linearly correlated to induced electrical field, which leads to nonlinear impact. Since Bi<sub>2</sub>WO<sub>6</sub> demonstrate sophisticated electrical properties where it is temperature dependent. For an instance, when temperature reach more than 700°C, its conduction property become mostly ionic, in the contrast, it become electronic for lower oxygen partial pressure (Maćzka et al., 2010). Oxygen vacancies concentration play significant role in affecting the electrical conductivity of Bi<sub>2</sub>WO<sub>6</sub>. When O<sub>2</sub>

engagement is reduced, the greater the tendency to be n-type semiconductor, whereas excessive  $O_2$  activity could facilitate the p-type conductivity (Elaoui et al., 2023). Yet, electronic structure and morphology of semiconductor are main factors in affecting photocatalytic reaction effectiveness. As mentioned earlier, valence band of  $Bi_2WO_6$  is formed by hybridization of Bi 6s and O 2p orbitals while W 5d orbitals constitutes conduction band minimum, result in bandgap within the range of 2.6 eV to 2.9 eV. This promotes the movement of photogenerated charge carrier, enhance oxidation-reduction ability in pollutant degradation under visible-light irradiation (Zhou et al., 2015).

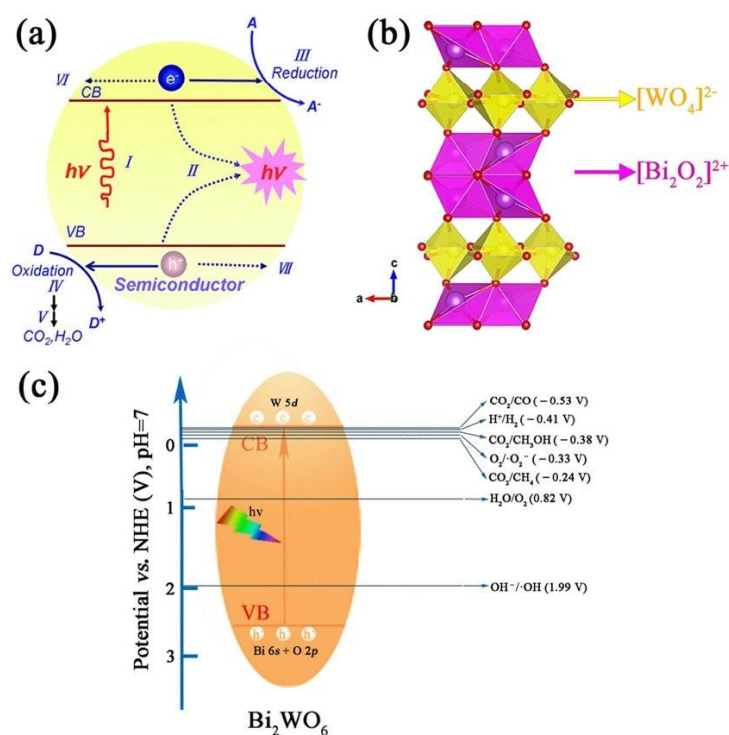


**Figure 2.2 shows (a) Schematic illustration of semiconductor photocatalysis, (b) Crystal structure of  $Bi_2WO_6$ , (c) hybridization of Bi 6s + O 2p orbitals lead to high redox potential (Chen et al., 2021).**

The outstanding photodegradation performance of  $Bi_2WO_6$  can be attributed to its high crystallinity, large specific surface area for pollutant adsorption, particles sizes, as well as defect concentration. According to Elaoui et al. (2023), fabrication processes and morphologies of photocatalyst are vital in generating catalyst with superior characterizations. Table 2.6 has listed comparison between bismuth-based



photocatalyst. There are several common synthesis methods for  $\text{Bi}_2\text{WO}_6$  preparation, namely solid-state synthesis, hydrothermal process, solvothermal method, sol-gel method, electro-deposition, and microwave-assisted method. Among these fabrication pathways, hydro/solvothermal methods are frequently employed for  $\text{Bi}_2\text{WO}_6$  preparation owing to its advantages of producing 3D nanostructure such as flower-like, erythrocyte-like, single-crystal-like, and hallow shape via adjustment of process temperature, reaction time, solvent, and pH level. It is worth to note that,  $\text{Bi}_2\text{WO}_6$  with 3D flower-like shape containing numerous nanoplates provides large specific surface area for adsorption reaction of target species and high mobility of photogenerated electrons to gather solid pollutant via oxidation process, demonstrates exceptional photodegradation activity of cephalosporin antibiotic (Chen et al., 2021).

Table 2.7 provides summary of  $\text{Bi}_2\text{WO}_6$  with various morphologies for diverse photocatalytic applications. According to Zhang et al. (2012),  $\text{Bi}_2\text{WO}_6$  nanofibers fabricated via electrospinning method is preferable than  $\text{Bi}_2\text{WO}_6$  produced via solid-state reaction (SSR). It can be observed through the methylene blue (MB) degradation, because  $\text{Bi}_2\text{WO}_6$  nanofibers could decompose 20 ppm MB within 3.5 hours with degradation efficiency as high as 94.69%, while SSR-  $\text{Bi}_2\text{WO}_6$  could merely achieve 54.3%. At the meantime, this  $\text{Bi}_2\text{WO}_6$  nanofibers demonstrate high photodegradative stability after repeated degradation activity. Yang et al. (2017) investigated the photodegradation performance on Rhodamine-B (RhB) of  $\text{Bi}_2\text{WO}_6$  nanofibers and hierarchical  $\text{Bi}_2\text{WO}_6$  microspheres, found that Barrett-Emmett-Teller (BET) surface area of hierarchical microspheres is greater than nanofibers due to high quantity of mesopore which provide more surface-active sites for RhB adsorption reaction which allows charge carrier mobility to become relatively simple. Therefore, the degradation efficiency of RhB under visible light irradiation using hierarchical microspheres and nanofibers reach to 74% and 88 within 60 minutes, respectively. Hierarchical  $\text{Bi}_2\text{WO}_6$  nanoarchitecture reported by Wang et al. (2015), the measured bandgap is 2.71 eV which implies the ease of excitation of electron-hole pairs under visible light irradiation with wavelength greater than 400 nm. Formation of hydroperoxyl and superoxide radicals demonstrate strong redox capability in oxidizing RhB molecules and subsequently convert to non-toxic products such as  $\text{H}_2\text{O}$  and  $\text{CO}_2$ .

Xu et al. (2018) stated the  $\text{Bi}_2\text{WO}_6$  porous nanosheets with 18 nm thickness not

merely provide exceptional photocatalytic activity, but also provide high photoreduction efficiency of Cr (VI) which can be achieved almost 97% associated with high reusability and stability after four successive degradation cycles. In aspect of airborne pollutants, it was reported by Chen et al. (2015) that Bi<sub>2</sub>WO<sub>6</sub> hollow microspheres assembled by nanoplates capable of removing nitrogen monoxide (NO) with removal rate of 44.5% after 60 minutes irradiation time. This is ascribed to the high specific surface area facilitate diffusion of photoexcited holes to oxidable compounds. In another case, through adjusting the reaction temperature and undergoing calcination process, the crystallinity and pore environment are greatly influenced. According to Wang et al. (2015), Bi<sub>2</sub>WO<sub>6</sub> nanoplates that synthesized with temperature of 180°C and calcined at 400°C for 2 hours, result in formation of photocatalyst with high crystallinity and 3D multi-layered nanoplates with distinctive mesoporous structure. Associated with clearly identified fringes of lattice exhibiting an interplanar spacing of 0.192 nm to 0.273 nm, cause highly permeable and ease of diffusion for target gas species. Thus, NO removal efficiency of calcined Bi<sub>2</sub>WO<sub>6</sub> nanoplates is maintained at 89.8% which higher than 71.7% that conducted using uncalcined sample. Wang et al. (2015) and Wang et al. (2019) have revealed that the used nanoflake Bi<sub>2</sub>WO<sub>6</sub> has no observable change in degradation efficiency after few consecutive cycles and could easily recycled through simple filtration process. This proves that Bi<sub>2</sub>WO<sub>6</sub> are highly stable towards organic pollutant degradation such as dye molecules.

**Table 2.6 shows comparison between bismuth-based photocatalyst (Elaouni et al., 2023).**

<b>catalysts</b>	<b>Materials</b>	<b>Advantages</b>	<b>Disadvantages</b>	<b>Application(s)</b>
Bismuth vanadate	$\text{BiVO}_4$	<ul style="list-style-type: none"> <li>-Low band gap</li> <li>-Good dispersibility -non-toxic</li> <li>-corrosion resistant,</li> <li>-exceptional photocatalytic performance in degrading organic pollutants under visible light</li> </ul>	Overall photocatalytic activity is limited by the relatively low mobility of charge carriers it exhibits	<ul style="list-style-type: none"> <li>-Water splitting,</li> <li>-Photocatalytic degradation of pollutants</li> <li>-Solar fuel production</li> <li>-Antibacterial applications</li> <li>-Air purification</li> </ul>
Bismuth molybdate	$\text{Bi}_2\text{MoO}_6$	Visible light-responsive catalyst used in photocatalytic applications with a good photocatalytic efficiency and stability	-Relatively wide bandgap which limits its absorption of visible light and reduces overall efficiency	<ul style="list-style-type: none"> <li>-Photocatalysis,</li> <li>-Water treatment</li> <li>-Air purification</li> <li>-Solar fuel production</li> <li>-Energy storage</li> </ul>
Bismuth-based perovskites	$\text{BiFeO}_3$ $\text{BiMnO}_3$	<ul style="list-style-type: none"> <li>-Exhibit exceptional stability</li> <li>-Broad spectrum of multi-functional properties including water splitting, <math>\text{CO}_2</math> reduction, and catalytic energy storage</li> </ul>	-Challenge on synthesis of bismuth-based perovskites, their overall efficiency can be constrained by defects and surface reactivity, which have an impact on their performance	<ul style="list-style-type: none"> <li>-Photocatalysis</li> <li>-Water splitting</li> <li>-Solar cells</li> <li>-Wastewater treatment</li> <li>-Energy storage</li> </ul>

Bismuth-based zeolites	<p>Bismuth-containing ZSM-5 zeolite</p> <p>Bismuth-containing beta zeolite</p> <p>Bismuth-exchanged Y zeolite</p> <p>Bismuth-containing MFI zeolite</p>	<p>Demonstrate notable activity and exhibit a high level of selectivity on NO<sub>x</sub> reduction and hydrocarbon conversion</p>	<p>The synthesis process of these catalysts can involve complexity, and various factors such as metal loading, acidity, and reaction conditions can influence their catalytic performance</p>	<ul style="list-style-type: none"> <li>-Catalytic applications</li> <li>-Adsorption</li> <li>-Separation environmental sensing</li> <li>-Energy storage and conversion</li> </ul>
Bismuth tungstate	Bi <sub>2</sub> WO <sub>6</sub>	<ul style="list-style-type: none"> <li>-Exhibits responsiveness to visible light, demonstrates exceptional effectiveness in achieving photocatalytic efficacy</li> <li>-Good chemical and thermal stability</li> </ul>	<p>tendency towards rapid charge carrier recombination, detrimentally impact its overall photocatalytic efficiency.</p>	<ul style="list-style-type: none"> <li>-Photocatalysis</li> <li>-Antibacterial applications</li> <li>-Self-cleaning surfaces</li> <li>-Water splitting for hydrogen production</li> <li>-Environmental sensors</li> </ul>

**Table 2.7 shows summary of Bi<sub>2</sub>WO<sub>6</sub> with various morphologies for diverse photocatalytic applications.**

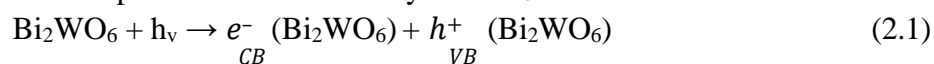
Photocatalyst	Synthesis Method	Light Source	Reaction conditions			Photocatalytic Activity	References
			Catalyst Loading	Pollutant	Initial Concentration of pollutant		
Hierarchical Bi <sub>2</sub> WO <sub>6</sub> microspheres	Electrospinning process	Visible light	1 g/L	Rhodamine-B	10 mg/L	88% RhB degradation	(Yang et al., 2017)
Hierarchical Bi <sub>2</sub> WO <sub>6</sub> microspheres	Electrospinning process	500 W Xenon lamp	1.5g/L	Methylene Blue	20mg/L	94.7% MB degradation	(Zhao et al., 2012)
2D Ultra-thin Bi <sub>2</sub> WO <sub>6</sub> porous nanosheets	hydrothermal	300 W Xenon lamp	1.2 g/L	Cr (VI)	10 mg/L	97% Cr (VI) degradation	(Xu et al., 2018)
3D Hallow Bi <sub>2</sub> WO <sub>6</sub> microspheres	Ultrasonic spray pyrolysis	300 W halogen lamp	0.3 g/L	Nitrogen monoxide	48 mg/L	44.5% NO removal	(Chen et al., 2017)
2D Flake-Like Bi <sub>2</sub> WO <sub>6</sub>	Hydrothermal	Visible light	1.0 g/L	Rhodamine-B	5 mg/L	100% RhB degradation	(Wang et al., 2015)
Hierarchical Bi <sub>2</sub> WO <sub>6</sub> nanoarchitecture	Solvothermal	Visible light	0.5 g/L	Rhodamine-B	10 <sup>-5</sup> mol/L	97% RhB degradation	(Wang et al., 2015)
Mesoporous nanoplate multi-directional assembled Bi <sub>2</sub> WO <sub>6</sub>	Solvothermal	300 W Xenon lamp	0.02 g/mL	Nitrogen monoxide	2 mg/L	89.8% NO removal	(Wan et al., 2018)

## 2.6 Mechanism of Bi<sub>2</sub>WO<sub>6</sub> Photocatalysis

In recent years, Bi<sub>2</sub>WO<sub>6</sub> is considered as a promising candidate with relatively narrow bandgap width (2.8 eV), which make this semiconductor more feasible in absorption of photon in the visible light spectrum. The electron-hole pair recombination rate is lower as compared with other semiconductors with narrower bandgap energy such as graphitic carbon nitride (g-C<sub>3</sub>N<sub>4</sub>) with 2.7eV and Iron (III) oxide (Fe<sub>2</sub>O<sub>3</sub>) which possess 2.2 eV (Orimolade et al., 2021). Therefore, the photocatalysis process of Bi<sub>2</sub>WO<sub>6</sub> are constituted by 4 pivotal phases, namely electron-hole pair generation, charge carrier trapping, recombination of photoexcited electron and hole, and interfacial charge transfer.

Firstly, electron-hole pair generation. since narrow bandgap energy property of Bi<sub>2</sub>WO<sub>6</sub> which lower than 3eV, therefore when Bi<sub>2</sub>WO<sub>6</sub> is exposed to visible light or sunlight irradiation where incident photon energy ( $h\nu$ ) that are equivalent to or greater than its band gap ( $E_g$ ), photo-absorption and photoexcitation occurs. This result to facilitation of electrons ( $e^-$ ) in the filled VB level to occupy the vacant CB level, subsequently generate holes in the unfilled VB, and ultimately producing photo-induced electron-hole pairs ( $e^-_{CB}$  and  $h^+_{VB}$ ) (Ibhadon & Fitzpatrick, 2013). Eq. (2.1)

demonstrate the absorption of illumination by Bi<sub>2</sub>WO<sub>6</sub>.



Where

$h$  = Planck's constant

$\nu$  = frequency of incident light

Secondly, charge trapping entails capturing and immobilization of photogenerated electrons or holes at specified places on the surface or within the bulk of a Bi<sub>2</sub>WO<sub>6</sub> semiconductor. Such locations may be structural defects (crystal defect), oxygen vacancies, or other surface states. Trapping sites could momentarily hold confine charge carriers as well before allowing to excite back into the band triggered by external force which could be electric field, thermal radiation, or photon (Haneef et al., 2020). The photogenerated electron-hole pair also known as exciton pair which could be weakly or tightly connected with Coulomb attractive interactions. Yet, exciton pair with weakly bound is referred as Wannier-Mott excitons or free excitons,

usually encountered in nanocrystals made of semiconductors. In the contrast, exciton pair with tightly bound is known as Frankel excitons that generally appeared in organic dyes. According to Qian et al. (2019), in semiconductors, surface trapping tends to occur on either the subsurface or the surface. When capturing, charge carriers' principal states are temporal species like trapped holes, trapped electrons, and free electrons which has shown in Eq. (2.2) and (2.3). The trapped electrons and holes are prioritised to locate at the catalyst's surface, in the contrast, free electrons are scattered in the bulk. Charge trapping is considerably a slow as compared with other processes,



Charge carrier recombination could directly influence the overall effectiveness of photocatalysis of a semiconductor photocatalyst. Photo-excited electron-hole pairs are capable of recombine spontaneously at trapping sites on Bi<sub>2</sub>WO<sub>6</sub>'s surface or in the bulk, releasing energy as heat and light which shown in Eq. (2.4) and this behaviour is referred as surface recombination. Direct recombination of charge carrier pairs has been triggered at the catalyst surface. Yet, this occurs most commonly at defect sites such as interstitial atoms, vacancies, and grain boundaries (Qian et al., 2019). Auger Recombination is referring to a non-radiative process that additional energy generated from e<sup>-</sup>/h<sup>+</sup> pairs recombination is transmitted to electrons or holes then undergo simulation to greater energy level within identical band rather than emitting photons (Fu & Zhao, 2018). Especially Auger recombination is facilitated to occur at defect sites such as interstitial atoms or vacancies with equation shown in Eq. (2.5). Furthermore, removing crystal imperfections is anticipated as being efficient at reducing charge recombination while increasing photocatalytic efficiency.



Lastly, interfacial charge transfer. When photo-induced electrons at CB level and holes at VB level are migrated to Bi<sub>2</sub>WO<sub>6</sub> surface and separated apart without recombination, interfacial charge transfer mechanism is subsequently occurred where redox reaction (oxidation-reduction process) is triggered to happen on catalyst surface. On Bi<sub>2</sub>WO<sub>6</sub> semiconductor's surface, there are two reactions are initiated simultaneously, namely electron-induced reduction reaction and hole-induced

oxidation reaction. Photo-induced hole at valence band is reacted with absorbed species which is water molecules or hydroxide ion ( $\text{OH}^-$ ) to generate the highly reactive species called hydroxyl radicals ( $\bullet\text{OH}$ ) through oxidation reaction as shown in Eq. (2.6) and (2.7). Simultaneously, electrons in conduction band are utilized in reduction of molecular oxygen species ( $\text{O}_2$ ) to form superoxide radicals ( $\text{O}_2\bullet^-$ ), shown in Eq. (2.8). Hydrogen peroxide ( $\text{H}_2\text{O}_2$ ) is generated when photo-induced charge carrier on catalyst surface particularly positive hole at valence band react with water molecules ( $\text{H}_2\text{O}$ ) as illustrated in Eq. (2.9).  $\text{H}_2\text{O}_2$  is subsequently be decomposed to form hydroxyl radicals ( $\bullet\text{OH}$ ) and hydroxide ions ( $\text{OH}^-$ ) when reacted with photo-excited electron in conduction band shown in Eq. (2.10). Superoxide radicals ( $\text{O}_2\bullet^-$ ) could produce hydroperoxyl radicals ( $\text{HO}_2\bullet$ ) through protonation shown in Eq. (2.11).  $\text{HO}_2\bullet$  is known as highly reactive species and involves in degradation of organic pollutant. Once Fermi level as well as redox potential of the adsorbed pollutant molecules are positively greater than VB maxima or negatively lower than CB minima, it spontaneously induces the transfer of photo-excited charge carriers from catalyst surface to adsorbed pollutant molecules surface. Complete photocatalytic breakdown of organic contaminants comprises a mixture of several different kinds of reactive oxygen species (ROS), namely  $\bullet\text{OH}$ ,  $\text{O}_2\bullet^-$ ,  $\text{H}_2\text{O}_2$ ,  $\text{HO}_2\bullet$ , and  $\text{OH}^-$  into less harmful products such as  $\text{CO}_2$ ,  $\text{H}_2\text{O}$ , and mineral acids (Eq. (2.13)) (Qian et al. 2019; Haneef et al.,2020; Thongam & Chaturvedi, 2021).





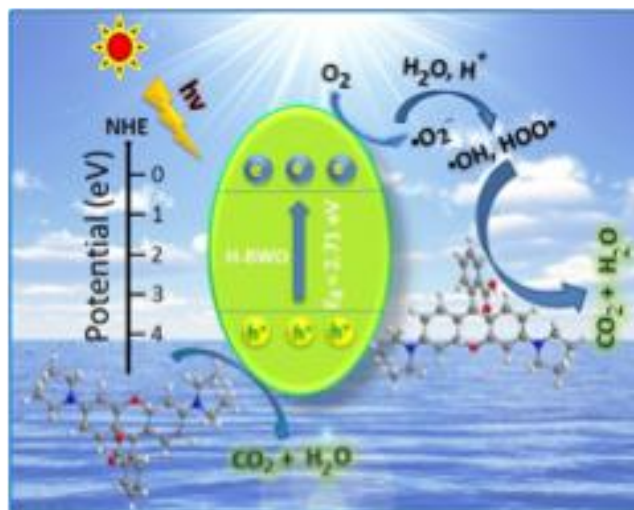


Figure 2.3 Photodegradation of organic pollutant by  $\text{Bi}_2\text{WO}_6$ . (Wang et al., 2015)

## 2.7 Modifications of Bi<sub>2</sub>WO<sub>6</sub>

Even though photocatalytic performance of Bi<sub>2</sub>WO<sub>6</sub> could be largely ameliorated through morphological control and atomic modulation, however, the charge carrier pairs separation efficiency are not meet the satisfactory level owing to the single component present in the photocatalysis process which implies that recombination rate is considerably high. According to Orimolade et al. (2021), unaltered Bi<sub>2</sub>WO<sub>6</sub> has weak photocatalytic effectiveness when exposed to light in the visible spectrum. That is because primarily unaltered Bi<sub>2</sub>WO<sub>6</sub> has a tendency of rapid recombination of photogenerated charge carriers, that severely restricts the synthesis of reactive oxygen species in photocatalysis. The relatively high kinetic of charge carrier recombination than redox reaction on catalyst surface, lead to decrease in quantum efficiency of photocatalytic performance (Zhang & Zhu, 2012). As a result, the majority of current studies has focused on altered Bi<sub>2</sub>WO<sub>6</sub>. In general, single Bi<sub>2</sub>WO<sub>6</sub> has relatively narrow bandgap which is within the range of 2.6 to 2.9 eV, therefore it has some restrictions in terms of visible light absorbance, notably single Bi<sub>2</sub>WO<sub>6</sub> photocatalyst could merely absorb photon energy with visible light that wavelength less than 450 nm. Apart from that, active sites on Bi<sub>2</sub>WO<sub>6</sub> catalyst surface for sake of redox reactions are insufficient in which restricts adsorption reaction of organic contaminants and possess limited reduction ability (Chen et al., 2021; Wang et al., 2022). Recently, the most common approaches consisted of morphological control, doping with metal and non-metal elements, atomic modulation, crystal defects as well as nanocomposite fabrication. Moreover, morphological control and atomic modulation are not such efficient in enhancing of migration and separation of charge carriers and recombination rate is considerably high. Therefore, coupling of Bi<sub>2</sub>WO<sub>6</sub> with metal-based, carbon-based or semiconductor material at its active facets to facilitate the greater photocatalytic activity while maximize the absorbance of photon energy from sunlight with broader visible light wavelength and increase photogenerated carriers separation (Chen et al., 2021; Shen et al., 2020).

Not only that, in p-n semiconductor photocatalytic system, Conventional type I (with a straddling gap) and II (with a staggered gap) heterojunctions are generally circumvented due to the problems of photo-excited electrons and holes has possibility to aggregate in the similar catalyst and charge carriers pairs unable to separate

efficiently, consequently hinders the photocatalytic activity. This scenario could lead to a decline in overall redox capability of the heterojunction photocatalyst owing to the decreased oxidation-reduction potential on the semiconductor (Low et al., 2017). For sake of increasing charge carrier separation efficiency and coping with ultrafast electron-hole recombination rate, Z-scheme photocatalytic system was suggested to resolve the problem of tendency of redox reaction that triggered at the relatively low oxidation and reduction potential. According to Figure 2.4, direct Z-scheme heterojunction photocatalyst capable of achieve spatial separation of photo-induced electrons and holes with a greater redox potential and even optimize the oxidation-reduction potential of reactions under sunlight irradiation. It is relatively simple for transferring electrons from the conduction band of photocatalyst II (PS-II) to the positive holes-rich valence band of photocatalyst I (PS-I) owing to electrostatic attraction between charged particles (Iwase et al., 2011). Not only that, the relatively low negative CB position of  $\text{Bi}_2\text{WO}_6$  single photocatalyst restricts production of  $\text{O}_2^{\bullet-}$  radicals.

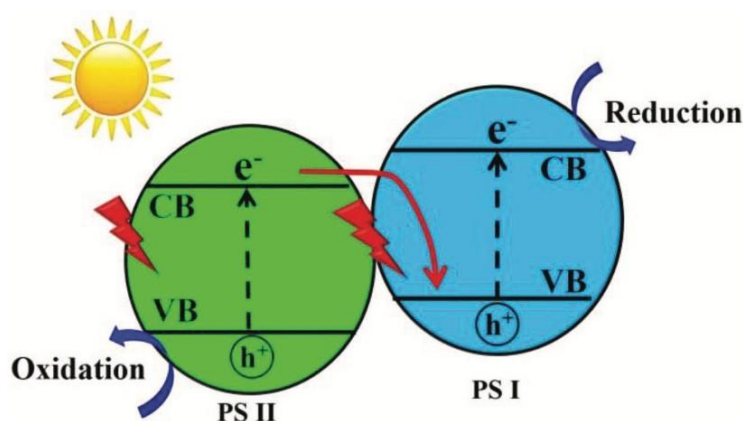


**Figure 2.4 Schematic illustration of electron-hole separation on a direct Z-scheme heterojunction photocatalyst under light irradiation (Low et al., 2017).**

Spinel ferrite ( $\text{MFe}_2\text{O}_4$ ,  $\text{M} = \text{Co}, \text{Zn}, \text{Sn}, \text{Mn}, \text{Cu}$ ) has attracted increasing attention recently owing to their exceptional properties including great electromagnetism characteristic, great chemical stability, extraordinary physical hardness as well as ferromagnetic conduct (Huang et al., 2015). Tin ferrite ( $\text{SnFe}_2\text{O}_4$ ) has undergone extensive research in coupling with other suitable semiconductors in wastewater treatment field owing to its recyclability from reaction medium via

magnetic separation process.  $\text{SnFe}_2\text{O}_4$  is referred to as p-type semiconductor with relatively narrow bandgap (approximately 2.53 eV to 2.7 eV). In general, spinel ferrite has face-centered cubic lattice structure and yet magnetic properties of  $\text{SnFe}_2\text{O}_4$  is mainly relevant to cationic distribution between tetrahedral and octahedral sites in lattice structure (Chen et al., 2016). Due to presence of high content of  $\text{Sn}^{2+}$  and  $\text{Fe}^{3+}$  cations, that fairly distributed at octahedral and tetrahedral sites, respectively and thus provides better magnetic characteristic and non-toxic feature which allows this ferrite compound is more preferable applied in organic contaminant degradation (Mahmood et al., 2020). The narrower bandgap of  $\text{SnFe}_2\text{O}_4$  allows it has high photo-responsive with visible light adsorption. Yet, its CB level (-1.45 eV) is commonly lower than standard potential of  $\text{O}_2\cdot^-$  radicals (-0.33 eV), makes  $\text{SnFe}_2\text{O}_4$  more feasible in superoxide radicals formation which is a reactive oxygen species to induce oxidation of target pollutant molecules (Han et al., 2022). Thereby,  $\text{SnFe}_2\text{O}_4$  nanoparticles exhibits outstanding photocatalytic activity and potentially to couple with other semiconductor materials to form z-scheme or type II heterojunction photocatalytic system (Jiang et al., 2022).

Hydroxyapatite (HAp,  $\text{Ca}_{10}(\text{PO}_4)_6(\text{OH})_2$ ) is known as bio-compatible photocatalyst that is naturally occurring mineral form of calcium apatite and belongs to group of calcium phosphate. In fact, HAp has a relatively large bandgap which approximately 4.84 eV to 6 eV and exists in either hexagonal or monoclinic lattice structure (Castro et al., 2024; Chiatti et al., 2012). Nevertheless, presence of  $\text{Ca}^{2+}$  and  $\text{PO}_4^{2-}$  ions has evenly organised in HAp crystal structure plus  $\text{OH}^-$  ions fill up interstitial spaces, therefore HAp is capable of capturing and eliminating heavy metal ions in wastewater. Owing to wide bandgap, it indicates that single HAp could not act as photocatalyst to work alone in photocatalytic reaction under visible light as high-energy photons from UV-light are for photoexcitation and formation of exciton pairs. Well-ordered hexagonal structure of HAp implies inexistence of defect vacancies in the lattice structure and no trapping site to capture photoinduced electrons and holes (Piccirillo & Castro, 2017). However, the synthesis method of HAp plays significant role in surface modification in which active sites could be abundant and oxygen vacancies formation is induced during calcination process. The photocatalytic activity on dye degradation is enhanced if appropriate synthesis approaches is introduced since HAp is generally has exceptional adsorption capacity for sake of target molecules

attachment (Piccirillo & Castro, 2017).

The coupling of  $\text{Bi}_2\text{WO}_6$  with  $\text{SnFe}_2\text{O}_4$  supported over HAp to fabricate novel Z-scheme visible light-driven ternary composite in which further improve photocatalytic activity, facilitate the charge transfer, and minimize the recombination rate of photo-excited electrons and holes. HAp is considered as a good support material due to its abilities to provide high adsorption capacity to target species, large specific surface area as well as high stability in basic and acidic solution. Hence, combination of binary mixture ( $\text{SnFe}_2\text{O}_4/\text{Bi}_2\text{WO}_6$ ) on the complementary component namely HAp could fairly increase the photoactive component dispersion and ameliorate available active site for redox reaction (Tripathi et al., 2015; Yahya et al. 2018).

From Table 2.8 illustrates the photocatalytic performance of  $\text{Bi}_2\text{WO}_6$ -based heterojunction ternary photocatalyst on different kinds of pollutants. A novel Z-scheme  $\text{BiOBr}/\text{Bi}/\text{Bi}_2\text{WO}_6$  has successfully synthesized by Chen et al. (2021) via hydrothermal method which is applied in organic dye degradation under visible light. 20%  $\text{BiOBr}/\text{Bi}/\text{Bi}_2\text{WO}_6$  nanocomposite with layered microsphere structure, yet high specific surface area as well as pore volume result in more active surface available for adsorption-desorption reaction of organic contaminants. The successful coupling of  $\text{Bi}/\text{Bi}_2\text{WO}_6$  with  $\text{BiOBr}$  is indicated by decreased PL intensity and recombination tendency of photo-induced charge carrier pairs in photoluminescence (PL) analysis. This ternary composite having narrower band gap of 2.53 eV has maximized utilization of solar energy and achieved the highest degradation efficiency of RhB (98.02%) as compared with pure  $\text{Bi}_2\text{WO}_6$  within 60 minutes. When looking into reusability of photocatalyst, the degradation efficiency is decreased from 98.02% to 87.33% after 4 consecutive cycles which might owing to the reasons of mutation in configuration of its active sites as well as the incomplete removal of organic pollutant after each cycle, end up in a loss in specific surface area or pores blockage.

Apart from that, Z-scheme heterojunction of a new  $\text{Bi}_2\text{S}_3@\text{Bi}_2\text{WO}_6/\text{WO}_3$  has revealed by Liu et al. (2021) provides complementary impact of oxygen vacancy and heterojunction photocatalytic system. 12wt%- $\text{Bi}_2\text{S}_3@\text{Bi}_2\text{WO}_6/\text{WO}_3$  ternary composite exhibits the greatest photocurrent density, implies that high separation effectiveness for photogenerated electrons and holes and led to improved photocatalytic activity.

Although the surface area of ternary composite is positively affected by the content of  $\text{Bi}_2\text{S}_3$  and 20wt% of  $\text{Bi}_2\text{S}_3$  present in the ternary composite has the highest surface area of  $24.67 \text{ m}^2/\text{g}$ , however it does not proportional to the capacity of organic pollutant adsorption. Therefore, 12wt%- $\text{Bi}_2\text{S}_3@ \text{Bi}_2\text{WO}_6/\text{WO}_3$  has shown the greatest RhB and colourless tetracycline degradation efficiency of 96% and 81%, respectively. Nevertheless, loading amount of  $\text{Bi}_2\text{S}_3$  exceeds 20wt%, photodegradation performance starts to decline. This is because of  $\text{Bi}_2\text{S}_3$  is potentially function as recombination facilitator which promote the photo-excited charge carriers recombination and thus inhibit the increase of photodegradation of organic pollutant. According to their findings, this novel ternary composite demonstrate exceptional stability and could maintain outstanding degradation efficiency after 3 consecutive cycles.

According to Tahir et al. (2021), has successfully fabricated novel heterojunction of photocatalyst (Mn-doped  $\text{Bi}_2\text{WO}_6\text{-MoS}_2\text{-GO}$ , in short Mn-BMG) by combining Mn-doped  $\text{Bi}_2\text{WO}_6$  supported over graphene oxide (GO) with binary metal sulphide  $\text{MnO}_2$ . Doping of  $\text{Mn}^{2+}$  ion into  $\text{Bi}_2\text{WO}_6$  enhances its specific surface area available for attachment of contaminants molecules, which can be clearly observed on the specific surface area of Mn-doped ternary composite ( $9.624 \text{ m}^2/\text{g}$ ) is higher than synthesized composite without doping of Mn ( $6.630 \text{ m}^2/\text{g}$ ). Since electron-hole pairs recombination tendency is positively reflected on PL intensity. Doping has destroyed the oxygen vacancies that exist in lattice structure of formed composite, therefore, recombination rate of electron-hole pairs can be greatly suppressed even though it possesses narrower bandgap. This could be validated in dye degradation under sunlight irradiation. MB degradation efficiency using Mn-BMG has achieved the highest (97%) among all the samples. Presence of GO capable of increase specific surface area, elevate the semiconductor's photo-response under visible light irradiation as well as function as mediator for charge transfer. Nevertheless, this novel Mn-doped BMG not only demonstrates outstanding degradation efficiency, but also shows high stability to rectify its reusability. Reusability of photocatalyst is indicated by the negligible decline in photocatalytic activity after 5 successive cycles.

Last but not least, Cho et al. (2023) revealed that the newly synthesized  $\text{BiVO}_4/\text{Bi}_2\text{WO}_6/\text{WO}_3$  ternary nanocomposite formed via hydrothermal method provides the highest photodegradation performance with pseudo-first-order rate

constant of  $0.0283 \text{ min}^{-1}$  which is approximately 1.6 and 2 times greater than rate constant shown by binary composite ( $k$  value of  $\text{BiVO}_4/\text{Bi}_2\text{WO}_6 = 0.0175 \text{ min}^{-1}$ ) and single composite ( $k$  value of  $\text{BiVO}_4 = 0.0139 \text{ min}^{-1}$ ), respectively. The cascade heterojunction system on ternary nanocomposite promotes the electron transfer and separation process and lead to increase in photocatalytic activity while maintaining high structural stability as well as reusability after 5 consecutive photocatalytic reactions.  $\text{BiVO}_4/\text{Bi}_2\text{WO}_6/\text{WO}_3$  with  $\text{WO}_3$  content of 25% shows the capability of degrading ciprofloxacin (CIP) and tetracycline (TC) with efficiency of 67.5% and 33.2 % within 100 minutes and 75 minutes, respectively. Since this ternary composite has relatively short lifetime compared with pure and binary component, notably, shortened lifespan confirms that ternary heterojunction system may benefit exciton pair dissociation via a non-radioactive quenching route.

**Table 2.8: Photocatalytic performance of Bi<sub>2</sub>WO<sub>6</sub>-Based Heterojunction ternary Photocatalyst on different kinds of pollutant.**

Photocatalyst	Pollutant	Synthesis method	Light source	Reaction Condition		Degradation efficiency (%)	Reference
				Catalyst loading (g/L)	Initial concentration of pollutant		
BiOBr/Bi/Bi <sub>2</sub> WO <sub>6</sub>	Rhodamine-B	Hydrothermal	350 W Xenon lamp	1	10 mg/L	98.02 (60 min)	(Chen et al., 2021)
Bi <sub>2</sub> S <sub>3</sub> @Bi <sub>2</sub> WO <sub>6</sub> /WO <sub>3</sub>	Rhodamine-B	Hydrothermal	400 W Xenon lamp	1	20mg/L	96 (180 min)	(Liu et al., 2019)
	Tetracycline				10 mg/L	81 (240 min)	
Mn-doped Bi <sub>2</sub> WO <sub>6</sub> -MoS <sub>2</sub> -GO	Methylene Blue	Hydrothermal	Sunlight	0.05	10 mg/L	97 (60 min)	(Tahir et al., 2021)
BiVO <sub>4</sub> /Bi <sub>2</sub> WO <sub>6</sub> /WO <sub>3</sub>	Methylene	Hydrothermal	Visible light source	0.2	10 mg/L	98.2 (80 min)	(Cho et al., 2023)
	ciprofloxacin					67.5 (100 min)	
	Tetracycline					33.2 (75 min)	



## 2.8 Phytotoxicity

Phytotoxicity assessment is widely applied in measuring the toxicity of various kind of chemicals and compounds using plant seeds. In general, it is primarily employed to evaluate organic materials, biosolids, industrial wastewater, as well as water quality. This test is also applied to detect toxicity of contaminant in the environment due to its ease of operation, cost-effective and could get highly trusted findings (Mendes et al., 2021). Phytotoxicological assays can determine the degree of toxicity in a particular substance, however, they are unable to recognise the component that causes toxic effect. It nevertheless allows for comparing levels of toxicity amongst the examined substances using the germination index (GI). GI value is inversely correlated to the toxicity degree of the evaluated specimens. Notably, the smaller the GI, the higher the toxicity of the analysed substance, specifically due to the either entirely or partially suppresses the development of the germinated roots (Guidoni et al., 2018).

Kuruvilla et al. (2024) has carried out phytotoxicity studies (employed *Vigna radiata* as test organism) to evaluate the toxicity level of treated solution containing orange G (OG) organic dye. The application of *Vigna radiata* or mung bean is considered as a robust and accurate model system that directly assess negative impact towards plant development caused by organic contaminant. There are 2 containers has been prepared, namely negative control and positive control. For negative control, mung bean is hydrated with distilled water while positive control indicated the hydration of plant seeds with treated OG solution in which graphite incorporated Ni-Co/ ZnO (G-NC/ZnO) nanocomposite photocatalysts are being used. By using the formula provided (Eq. (2.13)), the phytotoxicity percentage can be measured. After 10 days of monitoring process, average radicle length cultured in untreated solution is merely 12 cm, germinated seeds that hydrated with treated solution can produce radicle length as high as 24 cm, which is almost similar to the negative control, namely 26 cm. based on the result, the phytotoxicity rate was reduced from initially 53.8% to 46.8%, cultured in untreated and treated OG solution, respectively. The reduction of phytotoxicity indicates the ability and viability of G-NC/ZnO photocatalyst in dye wastewater treatment.

$$\text{phytotoxicity \%} = \left( \frac{\text{radicle len}0\text{th of control} - \text{radicle len}0\text{th}}{\text{radicle len}0\text{th of control}} \right) \times 100\% \quad \text{Eq.(2.13)}$$

Mohamed et al. (2023) has studied the photocatalytic activity of titanium dioxide quantum dots (TDs) photocatalyst towards the Coomassie brilliant Blue R (CBBR) and toxicity level has also analysed using seed germination test in which *Lycopersicon esculentum* plant as indicator. The germination rate was determined using the following formula (Eq. (2.14)). TD1 photocatalyst has greater available reactive surface for adsorption-desorption of CBBR molecules as compared with TD2 photocatalyst. Thus, the germination rate of treated solution using TD1 composite is 80% which 3% greater than that of TD2 composite. The obvious disparity can be seen as CBBR dye is applied as control results to the lowest percentage of seed germination (29%). While the seed germination is enhanced to 59% (treated dye solution with TD1 photocatalyst) higher than 53% (treated dye solution with TD2 photocatalyst). Therefore, titanium dioxide photocatalyst is efficient for CBBR dye degradation due to its smaller particle size and active sites while demonstrating harmless impact to the environment.

$$\text{Germination rate}(\%) = \frac{G_s}{T_s} \times 100 \quad \text{Eq.(2.14)}$$

Where  $G_s$ = germinated seeds;  $T_s$ = total number of seeds.

## 2.9 Antibacterial Experiments

Antibacterial applications in wastewater treatment serve a significant function in reducing the effects of pollution, in addition protecting human health. Antibacterial compounds may be employed in wastewater treatment procedures including disinfection and microbial control to effectively locate and eradicate pathogenic and dangerous microorganisms. Chlorination using chlorine gas, ozonation used ozone gas, and ultraviolet (UV) radiation represent a few of traditional ways of sterilisation, whereby antibacterial compounds are utilized that degrade bacterial cell membranes, impede enzyme function, and impair that bacterium replication of DNA, resulting in the demise of microorganisms (Sun et al., 2019). Advanced oxidation processes (AOPs) especially heterogeneous photocatalysis has sparked extensive research on studying the feasibility as the antibacterial solution with principle of reactive oxygen species (ROS) formation under sunlight exposure. The main reasons include cost-effective, environmentally friendly, and sustainable technology photocatalysis are free of hazardous disinfection by-products even in an atmospheric condition (Rizzo et al., 2014). According to Ganguly et al. (2018), when semiconductor photocatalyst are employed as photoactive component and photon energy from visible light source initiate catalytic reaction that generate ROS to eliminate targeted bacterium and consequently converting them into  $\text{CO}_2$  and  $\text{H}_2\text{O}$ . Some semiconductors (for example: titanium dioxide ( $\text{TiO}_2$ )) act as promising antibacterial that employed as self-cleansing and self-infecting material (Buddiga et al., 2023). ROS such as hydroxyl radical ( $\bullet\text{OH}$ ) that generated could significantly destroy DNA and cell membrane and eventually interevent the bacterium's lifecycle.

For instance, the finding reported by Buddiga et al. (2023), revealed that antibacterial activity of 0.25wt% Zirconium (Zr)/ 1 wt% Phosphorous (P) co-doped  $\text{TiO}_2$  nanocomposite exhibits greater antibacterial activity where capable of showing inhibition zone of  $27 \pm 0.2\text{mm}$  for 129-pseudomonas mutant and  $24 \pm 0.3\text{mm}$  497-streptococcus mutant at concentration of  $400\mu\text{g/mL}$  as compared with un-doped  $\text{TiO}_2$  nanocomposite. This is ascribed to the high pore volume nature of co-doped photocatalyst provides high interfacial area for catalytic reaction to occur followed by oxidizing target bacteria with strong oxidizing agent, namely  $\bullet\text{OH}$  when catalyst

exposed to visible light. Apart from that, Awan et al. (2024) has studied the antibacterial performance of 25wt%-ZnWO<sub>6</sub>/NiWO<sub>6</sub> binary photocatalyst using foodborne bacterium *Escherichia Coli* (*E. coli*) as experimental strain that cultivated in Luria-Bertani (LB) agar. There is not any observable change of *E. coli* bacteria growth in the culture medium when placed in dark condition, and the quantities of colonies is obviously reduced upon sunlight exposure. This decline in activated bacterial counts indicates the photocatalytic disinfection effects that carried out by 25wt%-ZnWO<sub>6</sub>/NiWO<sub>6</sub>. This is due to the reason of oxidation reaction of *E. coli* with ROS such as •OH and O<sub>2</sub>•<sup>-</sup> once the photoexcitation process is initiated by visible light photon energy and bacteria DNA and mitochondria is eventually destroyed.

## 2.10 Summary of Literature Review

Clean water shortage that deteriorated by the water contamination issue has become an alarming topic in the worldwide. The presence of harmful bacteria and microorganism and organic dyes in the greywater should be eliminated from water bodies for sake of securing clean water quality and minimize the stress from water shortage which announced in the Sustainable Development Goal 6 (SDG 6), namely guarantee the accessibility and long-term sustainability of water supplies and sanitation for every individual. In the last few decades, heterogeneous photocatalysis has been extensively studied in aspect of environmental remediation and water reclamation via the application of suitable semiconductor as photoactive component. The pollutant level and bacterial growth can be greatly decreased through visible-light driven photocatalysis. In this research, a novel Z-scheme heterojunction ternary nanocomposite is constructed by coupling Bi<sub>2</sub>WO<sub>6</sub> with SnFe<sub>2</sub>O<sub>4</sub> and supported over HAp. Based on my knowledge, this ternary nanocomposite has yet to be synthesized in previous research and therefore it is first time to investigate its superior chemical and physical properties compared with single photocatalysts. This novel Z-scheme heterojunction photocatalytic system is expected to exhibit improved photocatalytic activity as HAp expands the available reactive surface for absorption-desorption reaction of organic pollutant and harmful bacterium. In this regard, the solvothermal method has been employed as fabrication technique to determine viability of proposed photocatalyst. Since there are few research applied solar light as the main energy source. Thereby, in this studies the experiment is conducted under visible light

irradiation by placing under the sunlight to maximize the photoexcitation process.

## CHAPTER 3

### METHODOLOGY

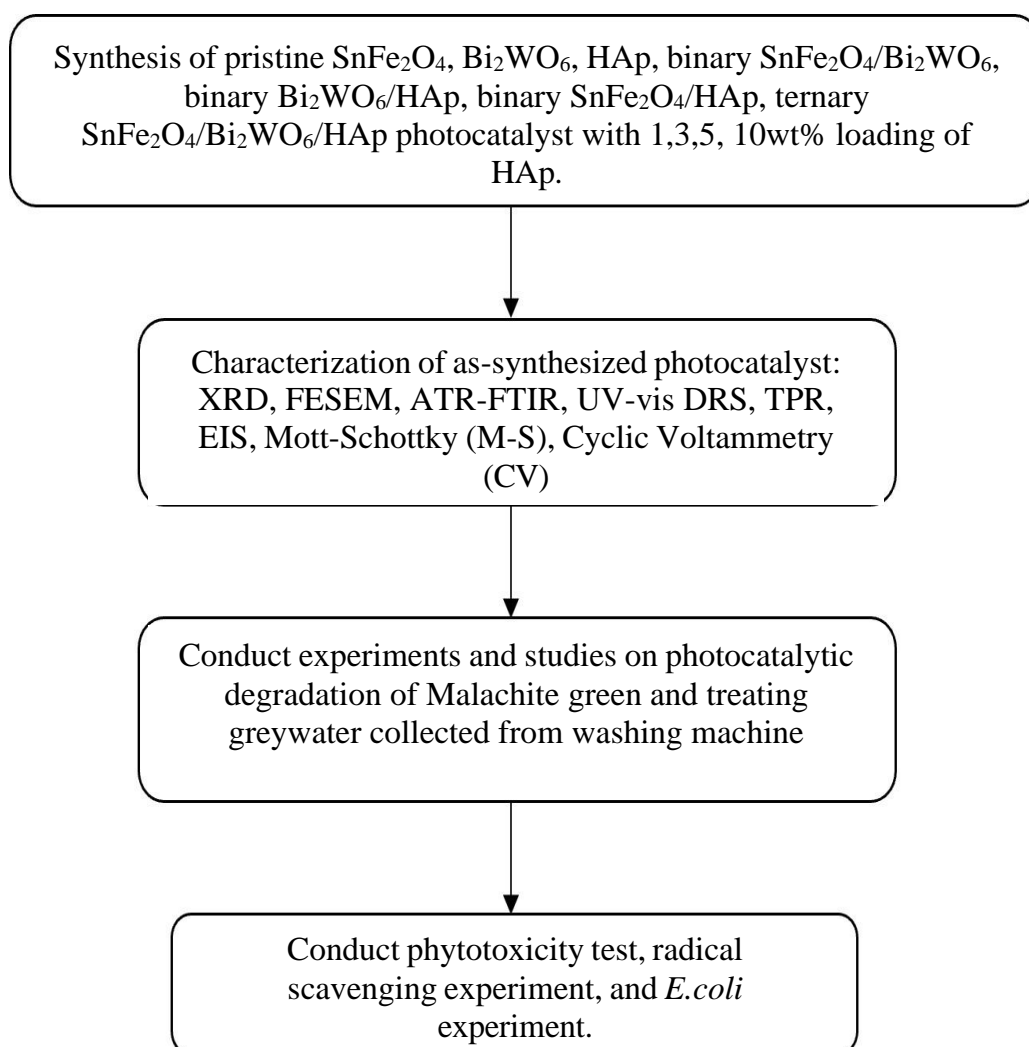


**Figure 3.1: Overall Experimental Flowchart**

### 3.2 Materials and Chemicals

Table 3.1 lists out the chemical materials employed in the current study.

**Table 3.1: List of Materials and Chemicals used.**

<b>Materials/Chemicals</b>	<b>Purity (%)</b>	<b>Supplier/Source</b>	<b>Application</b>
Bismuth nitrate pentahydrate [Bi(NO <sub>3</sub> ) <sub>3</sub> •5H <sub>2</sub> O]	98.0	R&M Chemicals	Bismuth precursor
Sodium tungstate dihydrate [Na <sub>2</sub> WO <sub>6</sub> •2H <sub>2</sub> O]	98.0	R&M Chemicals	Tungsten precursor
Tin (IV) Chloride Pentahydrate [SnCl <sub>4</sub> •5H <sub>2</sub> O]	98.0	HIMEDIA	Tin precursor
Iron (III) Chloride Hexahydrate [FeCl <sub>3</sub> •6H <sub>2</sub> O]	99.0	R&M Chemicals	Iron precursor
Hydroxyapatite [Ca <sub>10</sub> (PO <sub>4</sub> ) <sub>6</sub> (OH) <sub>2</sub> ]	-	Bovine Bone	Photocatalyst synthesis
Sodium Hydroxide [NaOH]	98.0	Chemiz	Photocatalyst synthesis; pH adjustor
Potassium Hydroxide [KOH]	85.0	Chemiz	pH adjustor
Methylene Blue [C <sub>16</sub> H <sub>18</sub> ClN <sub>3</sub> S]	82.0	ChemSol	Model pollutant for photodegradation of organic pollutant.
Rhodamine B [C <sub>28</sub> H <sub>31</sub> ClN <sub>2</sub> O <sub>3</sub> ]	90.0	QReC	Model pollutant for photodegradation of organic pollutant.

Malachite green [C <sub>23</sub> H <sub>25</sub> ClN <sub>2</sub> ]	-	R&M Chemicals	Model pollutant for photodegradation of organic pollutant.
Ethyl Alcohol [C <sub>2</sub> H <sub>5</sub> OH]	99.7	R&M Chemicals	Impurities removal during filtration; Radical Scavenger
Ethylene Glycol [C <sub>2</sub> H <sub>6</sub> O <sub>2</sub> ]	99.5	R&M Chemicals	Solvent used in photocatalyst fabrication.
Distilled Water [H <sub>2</sub> O]	-	Gainson Advanced Technology	Solvent used in photocatalyst fabrication.
Sodium Hypochlorite [NaOCl]	11%Cl	Progressive Scientific	Solvent used for sterilization of green bean for phytotoxicity test.
Sodium Sulphate [Na <sub>2</sub> SO <sub>4</sub> ]	99.8	Bendosen	Radical Scavenger
Ethylenediaminetetraacetic [C <sub>10</sub> H <sub>16</sub> N <sub>2</sub> O <sub>8</sub> ]	99.0	System Chemicals	Radical Scavenger
Benzoquinone [C <sub>6</sub> H <sub>4</sub> O <sub>2</sub> ]	98.0	Acros Organic	Radical Scavenger
Hydrochloric Acid [HCl]	37.0	LabScan	Cleaning FTO glass for photoelectrochemical test
Nafion [C <sub>7</sub> HF <sub>13</sub> O <sub>5</sub> S•C <sub>2</sub> F <sub>4</sub> ]	-	Aldrich	Medium for photoelectrochemical test



### 3.3 Preparation of Photocatalyst

For synthesizing pristine  $\text{SnFe}_2\text{O}_4$ , 0.85 mmol of  $\text{SnCl}_2 \cdot 5\text{H}_2\text{O}$  (0.894 g) and 1.70 mmol of  $\text{FeCl}_3 \cdot 6\text{H}_2\text{O}$  (1.38 g) were dissolved into 150 ml of ethylene glycol solution. The solution was then stirred for 30 minutes ensure powders was completely dissolved. After being stirred, 4M of NaOH solution (15 ml) was placed into solution and continue stirred vigorously at 550 rpm for 1 hour. The mixture solution was turned into yellowish and then transferred into a 200ml Teflon-lined stainless-steel autoclave and subjected to heat at  $180^\circ\text{C}$  for 15 hours. After heating, the autoclave was removed from oven and allowed to cool down to room temperature. The dark brown precipitate was filtered and washed repeatedly with distilled water and ethyl alcohol for several times. The precipitates were then dried in oven at  $70^\circ\text{C}$  for 12 hours. The precipitates were collected from dried filter paper and finely ground using mortar and pestle. The complete preparation process of  $\text{SnFe}_2\text{O}_4$  photocatalyst was illustrated in Figure 3.2.

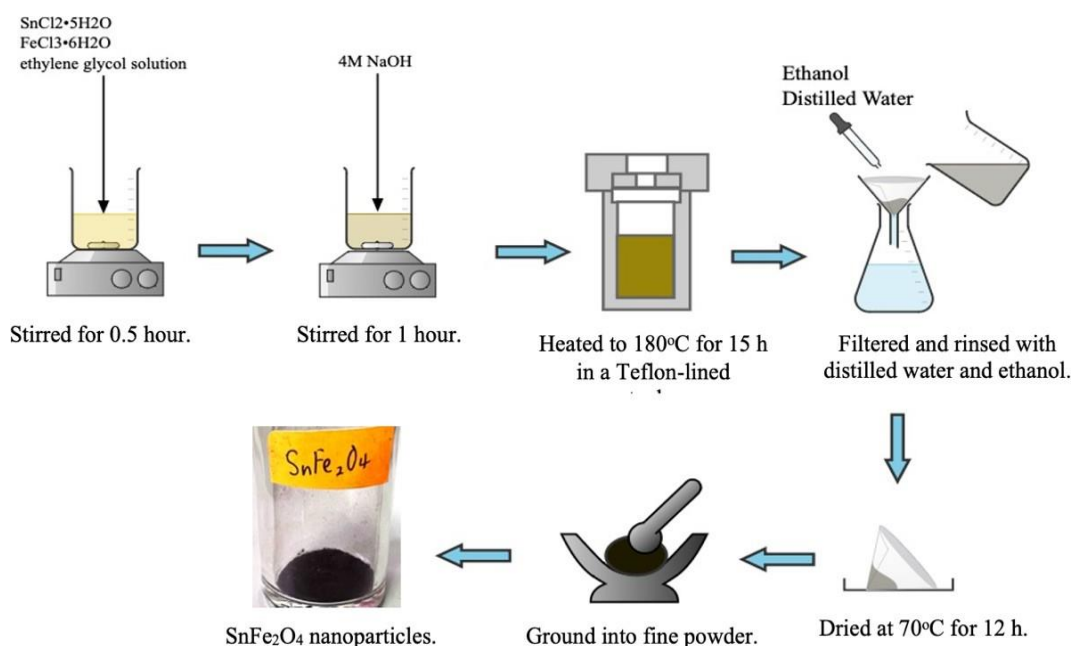


**Figure 3.2: Synthesis of  $\text{SnFe}_2\text{O}_4$  photocatalyst.**

For Synthesizing pristine  $\text{Bi}_2\text{WO}_6$ , 2 mmol of  $\text{Bi}(\text{NO}_3)_3 \cdot 5\text{H}_2\text{O}$  (1.94 g) was dissolved in 60 ml of ethylene glycol solution and labelled as solution A. Then 1 mmol of  $\text{Na}_2\text{WO}_4 \cdot 2\text{H}_2\text{O}$  (0.66 g) was dissolved into 60 ml of ethylene glycol solution and labelled as solution B. Solution B was added slowly into solution A using pipette, mixed solution was magnetically stirred at 450rpm for 30 minutes to ensure powders

were dissolved completely into solution. After being stirred, 4M of NaOH solution was added for pH adjustment until reach to pH value of 4.0. The mixture solution was turned into off white colour suspension and then transferred into a 200ml Teflon-lined stainless-steel autoclave and subjected to heat at 180°C for 18 hours. After heating, the autoclave was placed to cool down to room temperature. The pale-yellow precipitate was filtered and washed repeatedly with distilled water and ethyl alcohol for several times. The precipitates were then dried in oven at 70°C overnight. The precipitates were collected from dried filter paper and finely ground using mortar and pestle. The complete preparation process of  $\text{Bi}_2\text{WO}_6$  photocatalyst was illustrated in Figure 3.3.

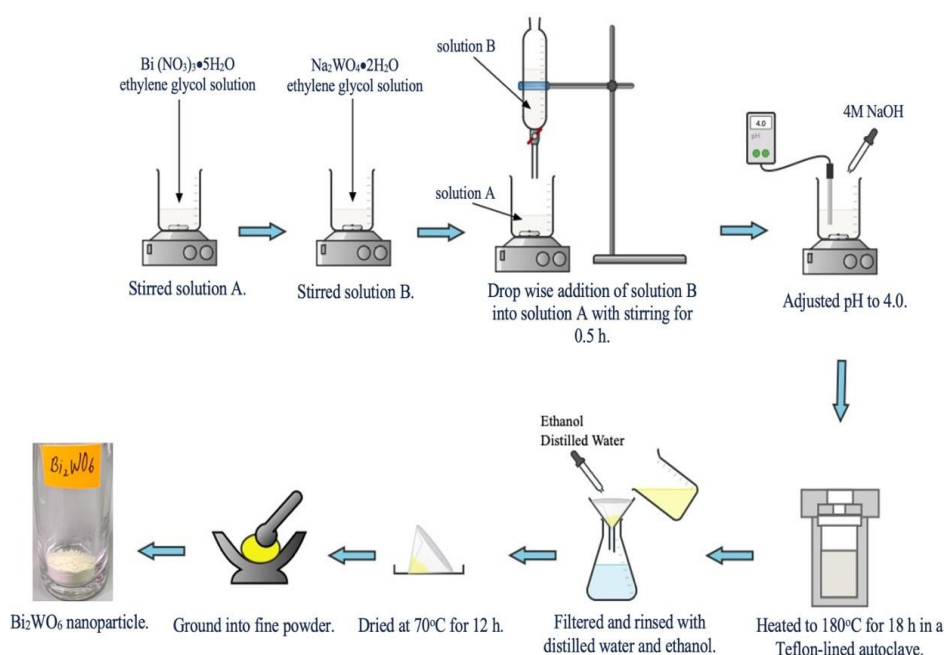


**Figure 3.3: Synthesis of  $\text{Bi}_2\text{WO}_6$  photocatalyst.**

For 7.5wt%-  $\text{SnFe}_2\text{O}_4/\text{Bi}_2\text{WO}_6$  binary composite fabrication, 2 mmol of  $\text{Bi}(\text{NO}_3)_3 \cdot 5\text{H}_2\text{O}$  (1.94 g) was dissolved in 60 ml of ethylene glycol solution and labelled as solution A. Then 1 mmol of  $\text{Na}_2\text{WO}_4 \cdot 2\text{H}_2\text{O}$  (0.66 g) was dissolved into 60 ml of ethylene glycol solution and labelled as solution B. Solution B was added slowly into solution A using pipette, mixed solution was magnetically stirred at 450 rpm for 30 minutes to ensure powders were dissolved completely into solution. After being stirred, 0.0976 g of  $\text{SnFe}_2\text{O}_4$  was added into mixed solution and underwent ultrasonication process in water bath for 30 minutes. 4M of NaOH solution was added for pH adjustment until reach to pH value of 4.0. The mixture solution was turned into

brown suspension and then transferred into a 200ml Teflon-lined stainless-steel autoclave and subjected to heat at 180°C for 18 hours. After heating, the autoclave was placed to cool down to room temperature. The light brown precipitate was filtered and washed repeatedly with distilled water and ethyl alcohol for several times. The precipitates were then dried in oven at 70°C overnight. The precipitates were collected from dried filter paper and finely ground using mortar and pestle. The complete preparation process of 7.5wt%-SnFe<sub>2</sub>O<sub>4</sub>/Bi<sub>2</sub>WO<sub>6</sub> binary composite was illustrated in Figure 3.4.

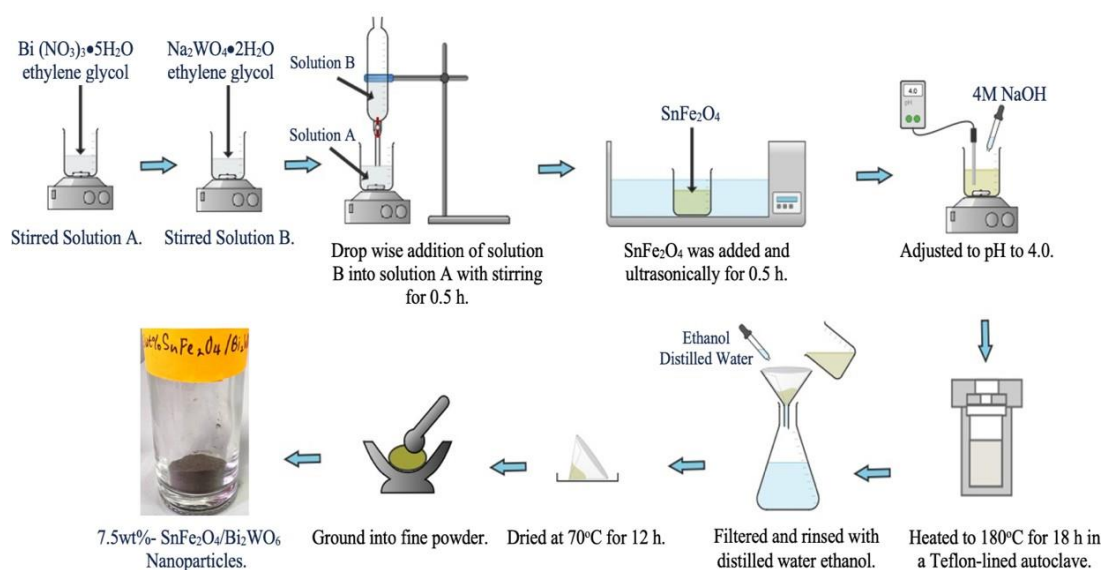


**Figure 3.4: Synthesis of 7.5wt%-SnFe<sub>2</sub>O<sub>4</sub>/Bi<sub>2</sub>WO<sub>6</sub> binary composite.**

For fabricating bovine-bone based HAp powder, bovine bone was collected, and the soft tissues attached on its surface was removed. The cleaned bovine bone was washed with tap water and wiped the remaining fluid using dry tissues before drying at 80°C for 4 hours. The cleaned bovine bone was sawed into tiny pieces and wiped with dry tissues to remove impurities generated during sawing process. Tiny pieces of bovine bone were ground into powdered form using Retsh ZM200 Ultra-centrifugal mill. Powdered bovine bone was sieved with 250µm mesh-sized sieve and then sent for calcination at 750°C for 2 hours. The white colour bovine bone powder was turned into dark brown colour and subsequently finely ground with mortar and pestle. Then 1 g of dark brown powder was weighed and added into 1M KOH aqueous solution (100 ml) and magnetically stirred overnight at room temperature. The solution was filtered, and precipitates was washed with distilled water for several times to remove residual KOH solution to ensure pH value close to 7.0. Collected dark brown

precipitates was dried at 80°C for 2 hours before sending for calcination at 750°C for 2 hours. HAp powder underwent second calcination process, colour changed from dark brown into white colour. Complete preparation process of HAp powder was illustrated in Figure 3.5.

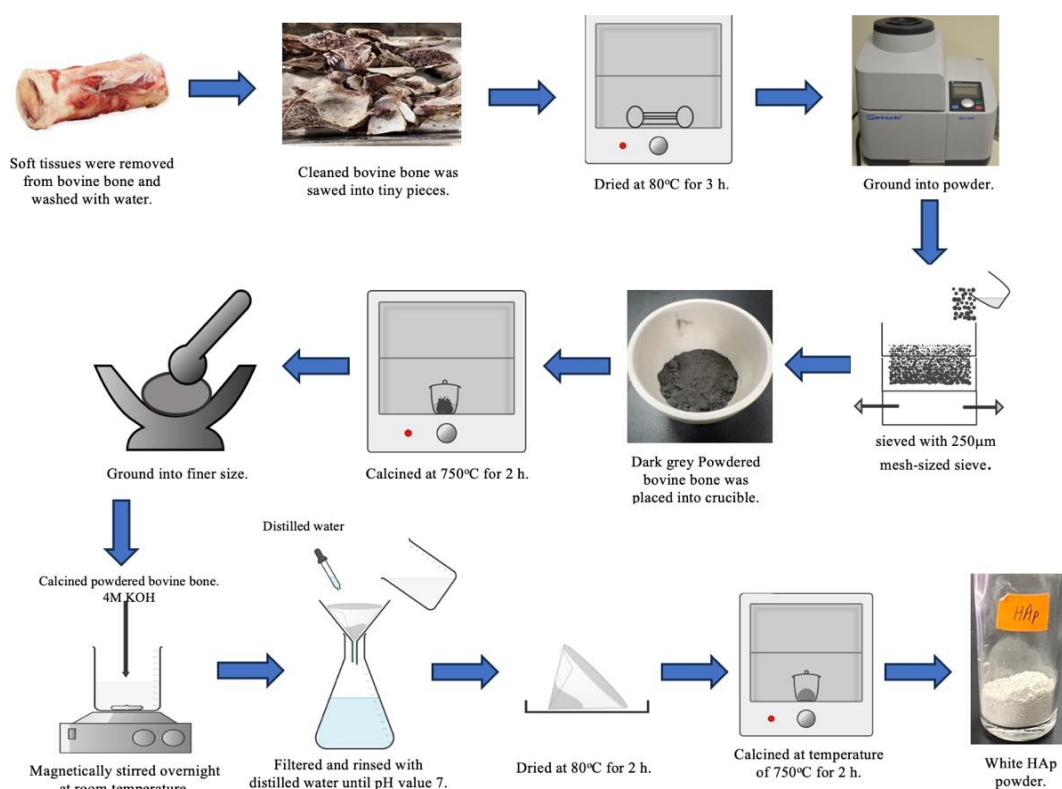


**Figure 3.5: Synthesis of HAp powder.**

For 7.5wt%-SnFe<sub>2</sub>O<sub>4</sub>/Bi<sub>2</sub>WO<sub>6</sub>/HAp ternary composite fabrication, 1 g of 7.5wt%- SnFe<sub>2</sub>O<sub>4</sub>/Bi<sub>2</sub>WO<sub>6</sub> powder was dissolved into 100 ml of distilled water, followed by HAp powder. The HAp powder amount was varied corresponding to its weight percentage, namely 1 wt% (0.010 g), 3 wt% (0.031 g), 5 wt% (0.053 g) and 10 wt% (0.111g). Mixture solution was then stirred ultrasonically for 3 hours. The sonicated solution was centrifuged at 3000 rpm for 5 min and subsequently dried at 80oC overnight. Complete fabrication process of powdered 7.5wt%-SnFe<sub>2</sub>O<sub>4</sub>/Bi<sub>2</sub>WO<sub>6</sub>/HAp ternary composite was illustrated in Figure 3.6. This approach was also employed for synthesis of other binary composites, namely SnFe<sub>2</sub>O<sub>4</sub>/HAp- 1wt% and Bi<sub>2</sub>WO<sub>6</sub>/HAp- 1wt%.

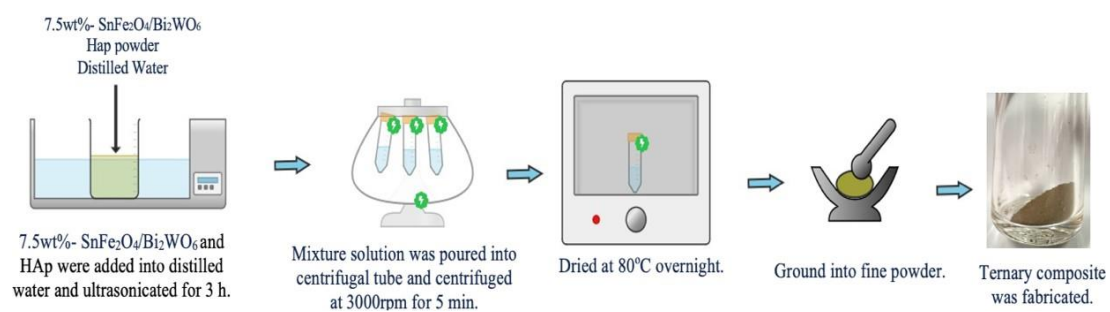


**Figure 3.6: Synthesis of 7.5wt%-SnFe<sub>2</sub>O<sub>4</sub>/Bi<sub>2</sub>WO<sub>6</sub>/HAp ternary composite.**

### **3.4 Characterization**

#### **3.4.1 X-ray Diffraction (XRD)**

The crystallographic structure of as-fabricated photocatalysts were analyzed using a Smimadzu XRD-6000 machine at Faculty of Science, UTAR Kampar. XRD on photocatalyst nanocomposites works on the principle that X-rays incident on a crystalline material undergo diffraction, resulting in a pattern of constructive and destructive interference unique to the substance's crystal lattice. By analysing the resulting diffraction pattern, XRD offers critical information on the crystal structure, phase composition, and crystallite size of photocatalyst nanocomposites, assisting in the understanding of their structural characteristics and potential photocatalytic activity. The XRD data were scanned at  $2\theta$  ranged from  $10^\circ$  to  $90^\circ$ .

#### **3.4.2 Field Emission Scanning Electron Microscopy (FESEM) and Energy Dispersive X-ray (EDX) Spectroscopy**

The surface morphology and elemental composition of as-fabricated photocatalysts were determined using a Quanta FEG 450 FESEM equipped with an Oxford X-Max 20 EDX supplied by the United Kingdom. The analysis was conducted at Faculty of Science, UTAR Kampar. The dried sample was uniformly distributed and mounted on an aluminium sample stub with the use of a double-sided carbon adhesive tape. FESEM employs a focused electron beam to scan the surface of materials, resulting in high-resolution images of intricate microstructures. When paired with EDX Spectroscopy, FESEM enables elemental analysis by detecting characteristic X-rays emitted when a concentrated electron beam interacts with the sample, providing valuable insights into the elemental composition and distribution within the microstructures of materials.

#### **3.4.3 Ultraviolet – Visible Diffuse Reflectance Spectroscopy (UV-vis DRS)**

UV-vis DRS analysis was performed to investigate the optical properties of the as-fabricated photocatalyst samples and to evaluate their band gap energy and absorption characteristics through a broad-spectrum light source to assess the diffuse reflectance

of a powdered sample in the UV and visible wavelength ranges. This analysis involved the use of JASCO V-730 UV-vis spectrophotometer available at Faculty of Engineering and Green Technology, UTAR Kampar.

#### **3.4.4 Fourier Transform Infrared Spectroscopy – Attenuated Total Reflectance (FTIR-ATR)**

FTIR-ATR was used to determine the functional groups in as-fabricated photocatalyst samples. The analysis was carried out using the Perkin Elmer Spectrum Two Universal ATR at Faculty of Science, UTAR Kampar. The ATR-FTIR data were scanned over the infrared wavelengths ranging from  $4000\text{ cm}^{-1}$  to  $400\text{ cm}^{-1}$ , and the amount of beam and frequencies at which the sample absorbed the infrared radiation were measured. It works by measuring the absorbance of infrared light as it interacts with a sample held in close proximity to an ATR crystal. The ATR crystal allows for higher sample-to-crystal contact, increasing the sensitivity and accuracy of the technique for analysing functional groups and molecular vibrations in materials.

#### **3.4.5 Transient Photocurrent Response (TPR), Electrochemical Impedance Spectroscopy (EIS), Mott-Schottky (M-S), and Cyclic Voltammetry (CV)**

The photoelectrochemical properties of the as-fabricated photocatalysts were measured via a Gamry Interface 1000 electrochemical workstation available at Faculty of Science, UTAR Kampar. TPR analysis determines time-dependent variations in photocurrent caused by illumination, providing insight into charge carrier dynamics and recombination rates in photocatalytic materials. EIS analysis characterises as-synthesized photocatalysts electrical impedance over a wide frequency range, providing insights into charge transfer mechanisms and interfacial features in electrochemical systems. M-S analysis evaluates the semiconductor-electrolyte interface by displaying capacitance versus applied potential, revealing information regarding carrier concentration and flat-band potential, thus band alignment of as-fabricated photocatalysts was investigated. CV analysis gives insight of on redox processes and electrochemical behaviour in photocatalytic materials by applying potential sweep to a working electrode to assess current response generated.

### 3.5 Photoactivity Test

The photodegradation performance of as-fabricated photocatalysts were evaluated through degradation of Malachite green (MG) and household greywater under visible light irradiation. For conducting of photodegradation of Malachite green in aqueous solution, 0.1g of photocatalyst powder was added into 100 ml of dye solution with initial concentration of 5mg/L to form suspension. The suspension was magnetically stirred in the dark condition for 1 hour to achieve adsorption-desorption equilibrium. 4 ml of suspension was collected and concentration of MG after equilibrium was measured using JASCO V-730 UV-vis spectrophotometer at the wavelength of 617 nm and recorded as the initial concentration ( $C_0$ ). Subsequently, the suspension was subjected to constant stirring under sunlight irradiation for 3 hours to evaluate the photocatalytic performance of as-synthesized photocatalysts, which was as depicted in Figure 3.7. Throughout the experiment, 4 ml of samples was collected at time interval of 20 minutes for measurement of MG concentration ( $C_t$ ) using the calibration curve of MG absorbance versus concentration (Distilled water + MG), which shown in Figure 3.8.



**Figure 3.7: Experiment Setup for photodegradation of Malachite Green dye in distilled water.**



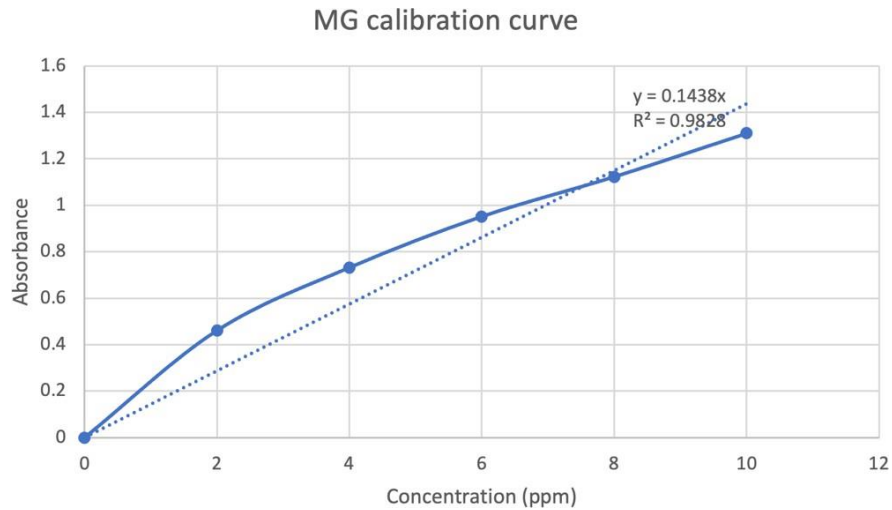


**Figure 3.8: MG calibration curve of Absorbance versus concentration (Distilled water + MG).**

In addition, the photocatalytic degradation of household greywater was conducted by adding 0.1 g of as-fabricated photocatalysts in 100 ml of greywater collected with initial concentration of 5mg/L. The suspension was put in the dark with constant stirring at 650 rpm for 1 hour to achieve adsorption-desorption equilibrium. After that, the 4 ml of suspension was collected and concentration of MG after equilibrium was measured at the wavelength of 617 nm. The experiment was then carried out under sunlight irradiation for 3 hours, as shown in Figure 3.9. 4 ml of suspension was extracted at every 20 minutes and measured concentration of degraded suspension ( $C_t$ ) using the calibration curve of MG absorbance versus concentration (greywater + MG), which shown in Figure 3.10. Throughout the experiment, the photocatalytic efficiency was determined using the equation labelled as Eq. 3.1,

$$\text{Photocatalytic efficiency (\%)} = \frac{(C_0 - C_t)}{C_0} \times 100\%. \quad (3.1)$$

Where,

$C_0$  = concentration of MG suspension at time  $t = 0$ , in unit of mg/L

$C_t$  = concentration of MG suspension at time  $t$ , in unit of mg/L

$$\ln \frac{C_0}{C_t} = k_{app} t$$

Where

$C_0$  = concentration of MG suspension at time  $t = 0$ , in unit of mg/L

$C_t$  = concentration of MG suspension at time t, in unit of mg/L

$k_{app}$  = apparent reaction rate constant, in unit of  $\text{min}^{-1}$

t = reaction time, in unit of min



**Figure 3.9: Experiment Setup for photodegradation of Malachite Green dye in greywater.**

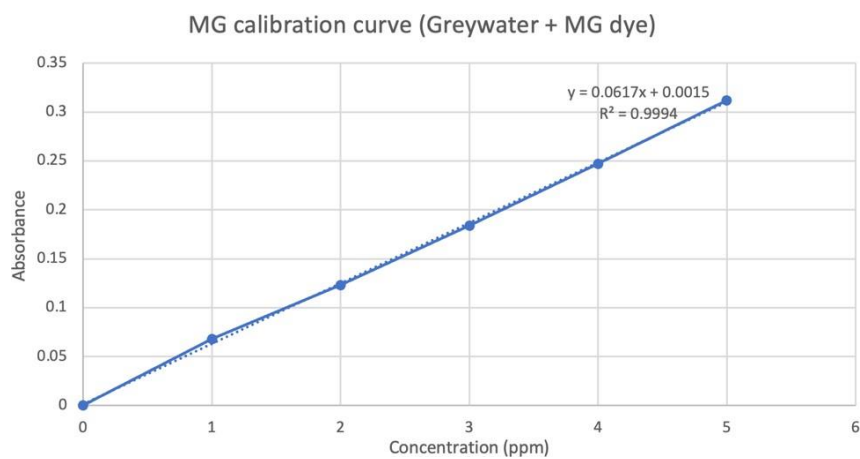


**Figure 3.10: MG calibration curve of Absorbance versus concentration (Greywater+ MG).**

### 3.6 Phytotoxicity Test

Phytotoxicity evaluation was carried out for photo-catalytically treated MG-greywater solution using commercially available mung bean seeds as phytotoxicity assessment indicator. Initially, the surface of green bean seeds was sterilized with acetic acid and rinsed with distilled water for several times. The sterilized seeds were then distributed in three transparent containers containing a layer of cotton wool wetted by distilled water (control) and MG-greywater solution (untreated and treated). The seed growth was subsequently monitored for 7 consecutive days. After 7 days, the sprouted seeds were taken out from the petri dishes and the radicle lengths were measured. The phytotoxicities of each sample was calculated according to Eq. (3.3).

$$\%phytotoxicity = \frac{\text{radicle length of control} - \text{radicle length of sample}}{\text{radicle length of control}} \times 100 \quad \text{Eq. (3.3)}$$

### 3.7 Radical Scavenging Experiment

The radical scavenging experiment was conducted to evaluate photodegradation performance of as-fabricated photocatalysts by elucidating the involvement of reactive oxygen species (ROS) in the photodegradation of MG and MG-containing greywater under sunlight irradiation. A more considerable loss in the photocatalytic efficiency after the addition of the scavenger indicated a more important role for the respective active species in photocatalysis. The test was carried out identically following the procedures for simultaneous photocatalytic activity experiment, except that 3 mM of various scavengers were added to 100 ml of MG-containing greywater before the addition of 0.1 g of photocatalyst. The scavengers applied in the experiment were ethyl alcohol (EtOH), ethylenediaminetetraacetic acid (EDTA), benzoquinone (BQ), and sodium sulphate (Na<sub>2</sub>SO<sub>4</sub>). The EtOH was used to scavenge hydroxyl radical ( $\bullet\text{OH}$ ), BQ was utilized to identify superoxide radical ( $\text{O}_2\bullet^-$ ), EDTA was applied to detect the photogenerated hole ( $h_{\text{VB}}^+$ ), and Na<sub>2</sub>SO<sub>4</sub> was used to scavenge photogenerated electron ( $e_{\text{CB}}^-$ ).

### **3.8 *E. coli* inactivation experiment**

Antibacterial experiment was carried out through the ability of the as-synthesized photocatalyst to inactivate the *E. coli* bacteria which is employed as experimental strain. Firstly, cultivation of *E. coli* in 100 mL of broth solution at 37°C with continual shaking in orbital shaker for 24 hours for bacterium activation. Then the culture medium was centrifuged at 4000 rpm for supernatant elimination. *E. coli* bacteria were washed two times with sterile NaCl saline solution and subsequently undergoes dilution process using saline water to  $10^7$  CFU/ml. 0.04 g of photocatalyst was added into test tube and the suspension solution was bubbled by air pump under visible light irradiation. The bacteria-containing solution was then dispersed equally over nutritional agar dishes at time intervals 60 minutes and total 180 minutes reaction time. Following a 24-hour incubation at 37 °C, the colony forming units (CFU) was assessed.

## CHAPTER 4

### RESULTS AND DISCUSSIONS

#### 4.1 Characterization

Catalyst characterization is significant for analyzing the properties of photocatalysts which provides better insights on morphological structure, chemical compositions, bandgap energy, effect of chemical loading and photocatalytic mechanism of composite material. Therefore, a wide range of characterization techniques were applied including Field Emission Scanning Electron Microscopy (FESEM), Energy Dispersive X-ray (EDX), X-ray Diffraction (XRD), Attenuated Total Reflectance – Fourier Transform Infrared Spectroscopy (ATR-FTIR), Ultraviolet-Visible Diffuse Reflectance Spectroscopy (UV-vis DRS), Transient Photocurrent Response (TPR), Electrochemical Impedance Spectroscopy (EIS), Mott-Schottky (M-S), and Cyclic Voltammetry (CV).

##### 4.1.1 Field Emission Scanning Electron Microscopy (FESEM)

The morphological analysis of as-fabricated photocatalysts was investigated through FESEM images. Looking into Figure 4.1(a), it indicated that  $\text{SnFe}_2\text{O}_4$  nanoparticles were nearly spherical structure, and the sizes of nanoparticles is uniformly consistent. Due to its excellent magnetization characteristics,  $\text{SnFe}_2\text{O}_4$  nanoparticles are interacted with one another and agglomerated to certain degree. Figure 4.1(b) clearly shows the FESEM image of  $\text{Bi}_2\text{WO}_6$  in broccoli-like morphological structure which indicates the as-synthesized photocatalyst is an aggregate of nanoparticles. This is

because nanoparticles generally have large surface area induces relatively high surface area and facilitate the Van der Waals force interaction among each other lead to aggregate entity (Gosens et al., 2010; Nedylakova et al., 2024). Figure 4.1(c) depicts the morphology of HAp, which demonstrate the smooth agglomerated nanostructure. The agglomeration of HAp particles is attributed to its relatively small particle sizes, large surface area incurs high tendency in formation of agglomerate owing to high molecular attraction. According to Figure 4.1(d), it demonstrated spherical structure of  $\text{SnFe}_2\text{O}_4$  nanoparticles has successfully attached on the broccoli-like structure formed by  $\text{Bi}_2\text{WO}_6$ , indicating the successful synthesis of binary composite of  $\text{SnFe}_2\text{O}_4/\text{Bi}_2\text{WO}_6$ . Since both of  $\text{SnFe}_2\text{O}_4$  and  $\text{Bi}_2\text{WO}_6$  are nanoparticles, thereby it is quite hard to differentiate as they are clumped together. Figure 4.1(e) shows the binary composite of  $\text{SnFe}_2\text{O}_4/\text{HAp}$ -1wt% in which  $\text{SnFe}_2\text{O}_4$  nanoparticles has fairly dispersed on the HAp nanoparticles, because HAp nanoparticles is comparatively larger however its loading is low. In addition, the presence of broccoli-like structure and smooth surface nanostructure indicates the successful integration of  $\text{Bi}_2\text{WO}_6$  and HAp. The surface morphology of ternary nanocomposite of 7.5wt%- $\text{SnFe}_2\text{O}_4/\text{Bi}_2\text{WO}_6/\text{HAp}$  with different loading (1wt%, 3wt%, 5wt%, and 10wt%) are illustrated in Figure 4.1(g) to (j), respectively. Since all materials are synthesized in nanostructure, and therefore, it has higher tendency to clump together and result in a large-sized agglomerate formation. For information, arrows in blue, yellow and red colour are used to point out  $\text{SnFe}_2\text{O}_4$ ,  $\text{Bi}_2\text{WO}_6$ , and HAp, respectively. Based on the FESEM analysis, it has signified the successful integration of HAp into binary nanocomposite ( $\text{SnFe}_2\text{O}_4/\text{Bi}_2\text{WO}_6$ ) in construction of novel ternary heterojunction composite.

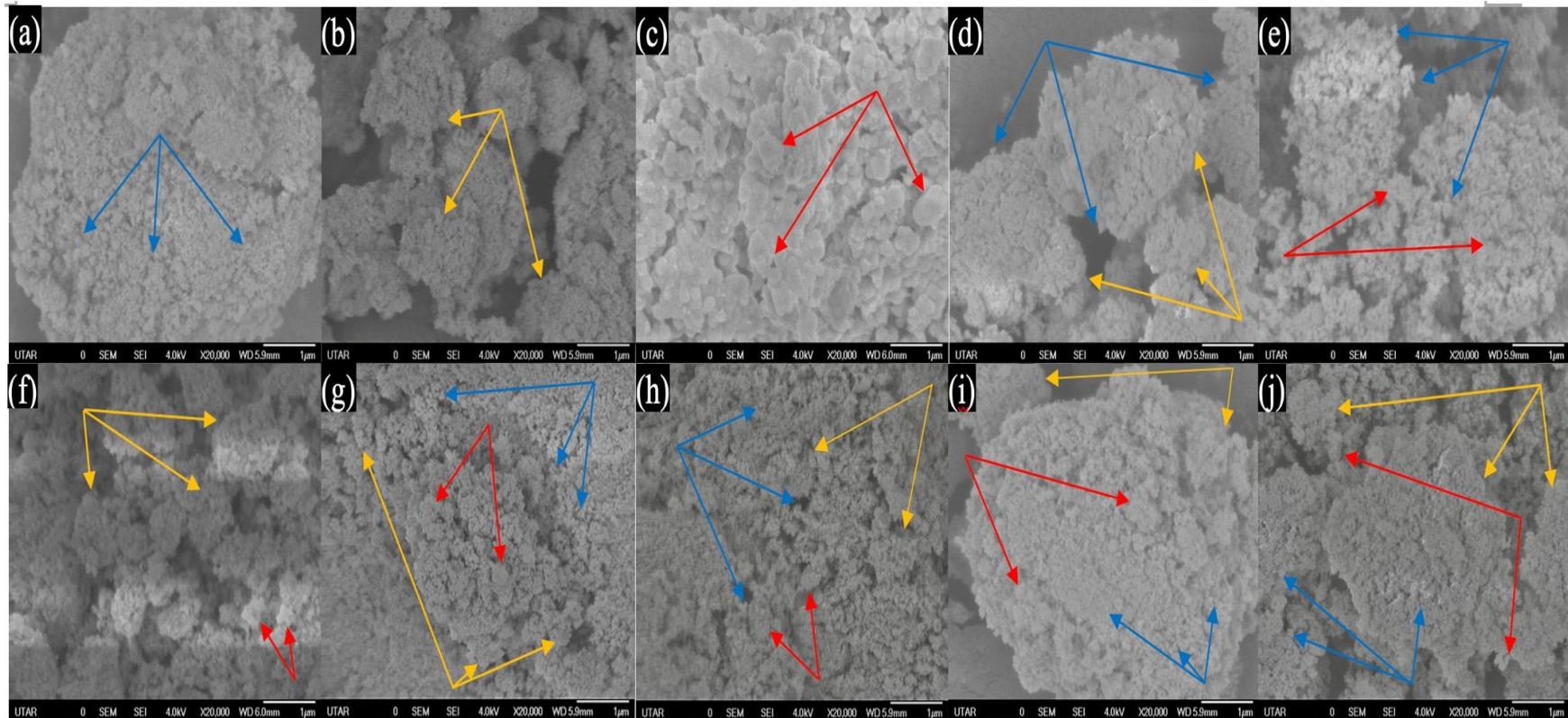


**Figure 4.1: FESEM images of as-synthesized photocatalysts; (a)  $\text{SnFe}_2\text{O}_4$ ; (b)  $\text{Bi}_2\text{WO}_6$ ; (c) HAp; (d) 7.5wt%- $\text{SnFe}_2\text{O}_4/\text{Bi}_2\text{WO}_6$ ; (e)  $\text{SnFe}_2\text{O}_4/\text{HAp}$ -1wt%; (f)  $\text{Bi}_2\text{WO}_6/\text{HAp}$ -1wt%; (g) 7.5wt%-  $\text{SnFe}_2\text{O}_4/\text{Bi}_2\text{WO}_6/\text{HAp}$ -1wt%; (h) 7.5wt%-  $\text{SnFe}_2\text{O}_4/\text{Bi}_2\text{WO}_6/\text{HAp}$ -3wt%; (i) 7.5wt%-  $\text{SnFe}_2\text{O}_4/\text{Bi}_2\text{WO}_6/\text{HAp}$ -5wt%; (j) 7.5wt%-  $\text{SnFe}_2\text{O}_4/\text{Bi}_2\text{WO}_6/\text{HAp}$ -10wt%. [Blue arrow represent  $\text{SnFe}_2\text{O}_4$ ; yellow arrow represent  $\text{Bi}_2\text{WO}_6$ ; red arrow represent HAp]**

#### 4.1.2 Energy Dispersive X-ray (EDX)

The elemental composition and distribution within as-fabricated photocatalyst was analysed using EDX spectroscopy. Figure 4.2 illustrates EDX spectra and elemental mapping of  $\text{SnFe}_2\text{O}_4$  nanocomposite in which elemental peaks of Sn, Fe and O associated with nonappearance of impurity peaks are detected. The presence of these three elements validates successful fabrication of single  $\text{SnFe}_2\text{O}_4$  nanocomposite and all elements involved are well-dispersed on surface. Figure 4.3 and Figure 4.4 depict the composition mapping of  $\text{Bi}_2\text{WO}_6$  and HAp, respectively. Referring to Figure 4.3, it shows elements (Bi, W, O) are present in pure  $\text{Bi}_2\text{WO}_6$ , while Figure 4.4 indicates the successful synthesis of HAp composed of 3 main elements namely Ca, P and O. Figure 4.5 to 4.7 exhibit the fabrication of binary nanocomposites, namely 7.5 wt%- $\text{SnFe}_2\text{O}_4/\text{Bi}_2\text{WO}_6$ ,  $\text{SnFe}_2\text{O}_4/\text{HAp}$ -1wt% and  $\text{Bi}_2\text{WO}_6/\text{HAp}$ -1wt% are satisfied, respectively. In addition, from Figure 4.8 to 4.11, they indicated successful synthesis of ternary nanocomposites with different loadings, which are 7.5 wt%- $\text{SnFe}_2\text{O}_4/\text{Bi}_2\text{WO}_6/\text{HAp}$ - (1wt%, 3wt%, 5wt%, and 10wt%). Interestingly, an increase in HAp loading is verified with the rise of HAp elements (Ca and P). Since three materials are produced in nanoparticle sizes which might not easily distinguished in term of morphological structure, however elemental mapping has significantly revealed the excellent dispersion throughout the composition supported with elementary table. As a result, homogeneous dispersion of elements within a ternary photocatalyst nanocomposites could guarantee competent photocatalytic performance without hindering the adsorption capacity.



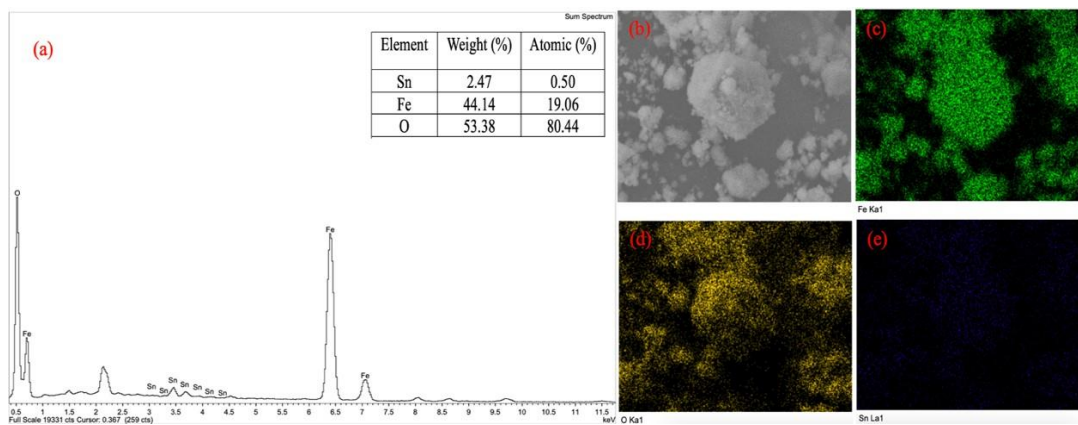


**Figure 4.2: (a) The EDX spectra of  $\text{SnFe}_2\text{O}_4$ ; (b)-(e) elemental dot mapping of  $\text{SnFe}_2\text{O}_4$ .**

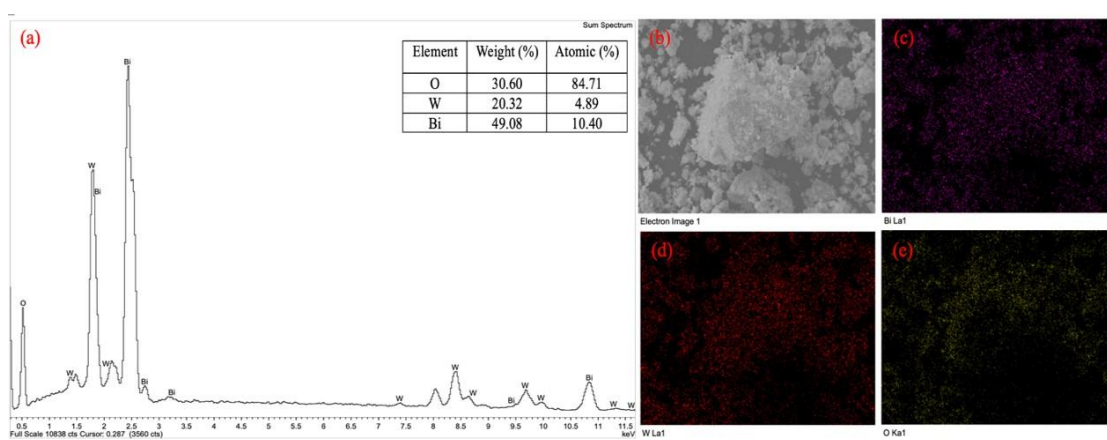


**Figure 4.3: (a) The EDX spectra of  $\text{Bi}_2\text{WO}_6$ ; (b)-(e) elemental dot mapping of  $\text{Bi}_2\text{WO}_6$ .**

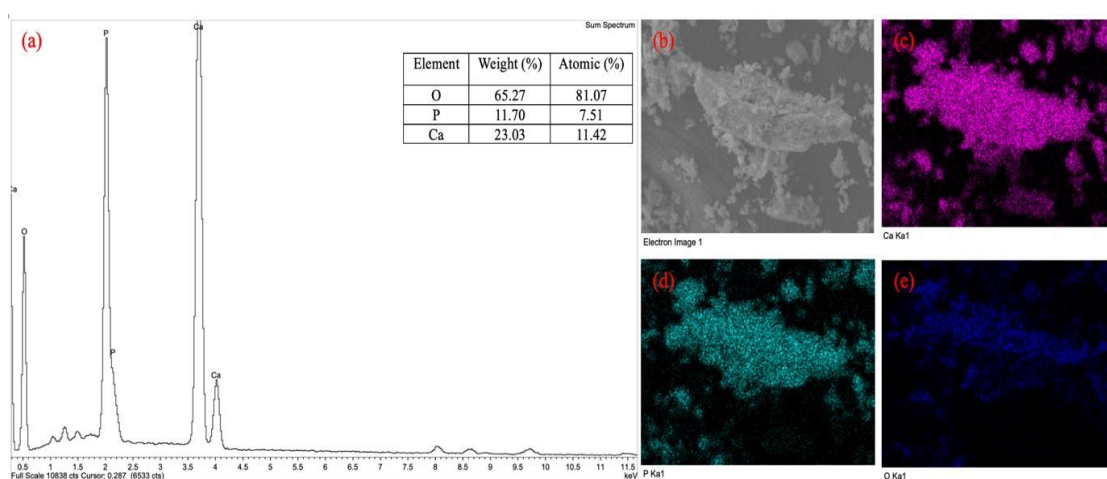


**Figure 4.4: (a) The EDX spectra of HAP; (b)-(e) elemental dot mapping of HAP.**

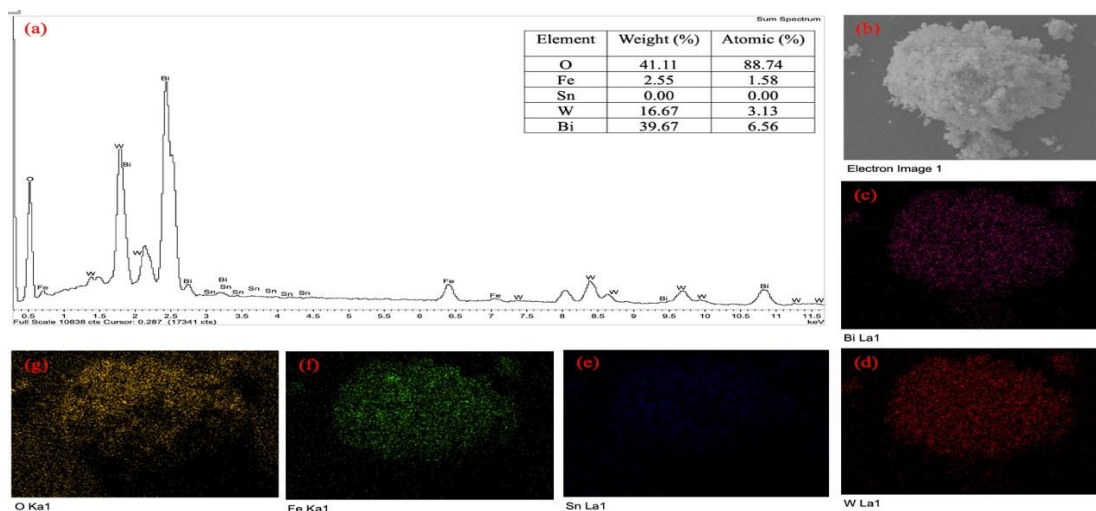


**Figure 4.5: (a) The EDX spectra of 7.5 wt%-SnFe<sub>2</sub>O<sub>4</sub>/Bi<sub>2</sub>WO<sub>6</sub>; (b)-(g) elemental dot mapping of 7.5 wt%-SnFe<sub>2</sub>O<sub>4</sub>/Bi<sub>2</sub>WO<sub>6</sub>.**

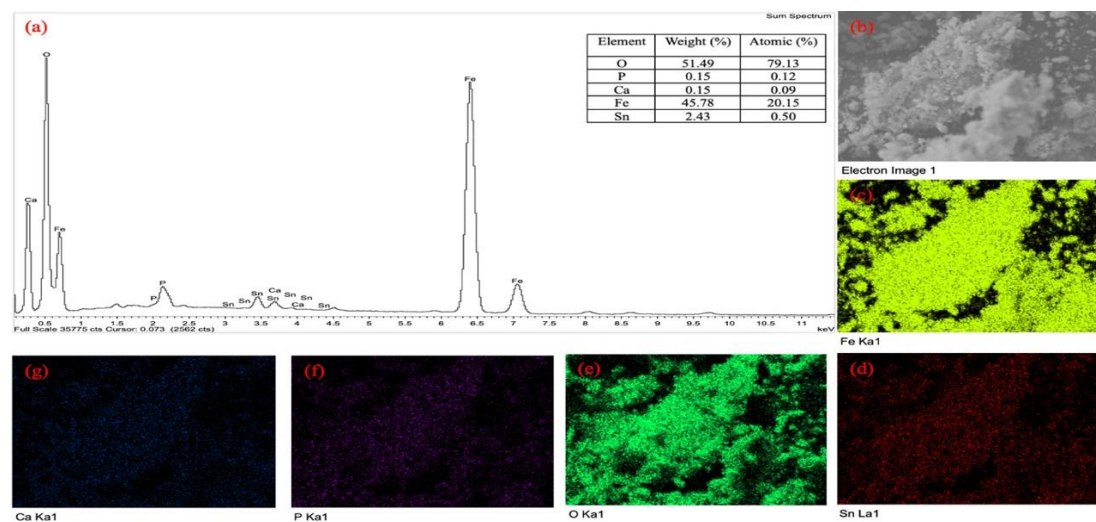


**Figure 4.6: (a) The EDX spectra of SnFe<sub>2</sub>O<sub>4</sub>/HAp-1 wt%; (b)-(g) elemental dot mapping of SnFe<sub>2</sub>O<sub>4</sub>/HAp-1 wt%.**

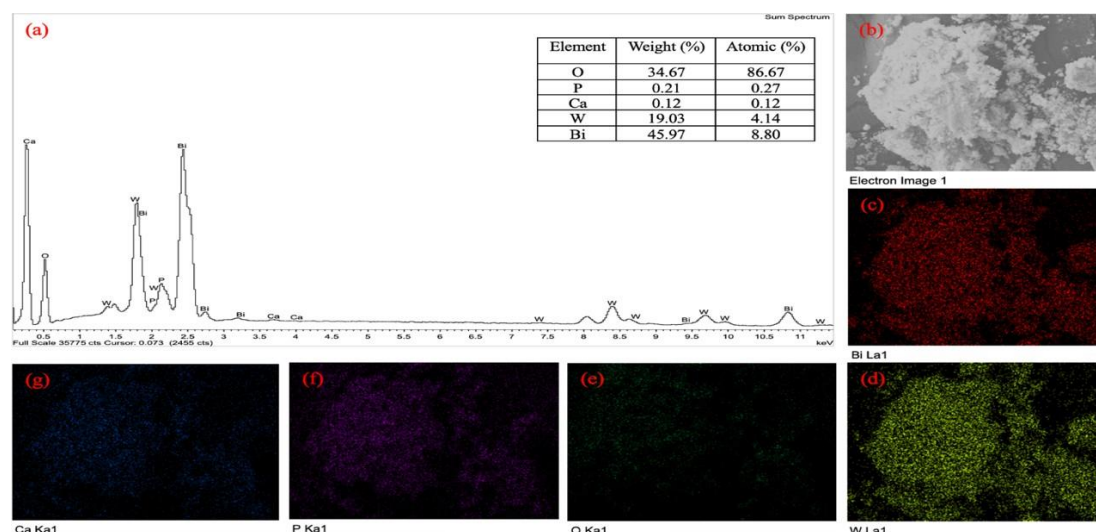


**Figure 4.7: (a) The EDX spectra of Bi<sub>2</sub>WO<sub>6</sub>/HAp-1 wt%; (b)-(g) elemental dot mapping of Bi<sub>2</sub>WO<sub>6</sub>/HAp-1 wt%.**

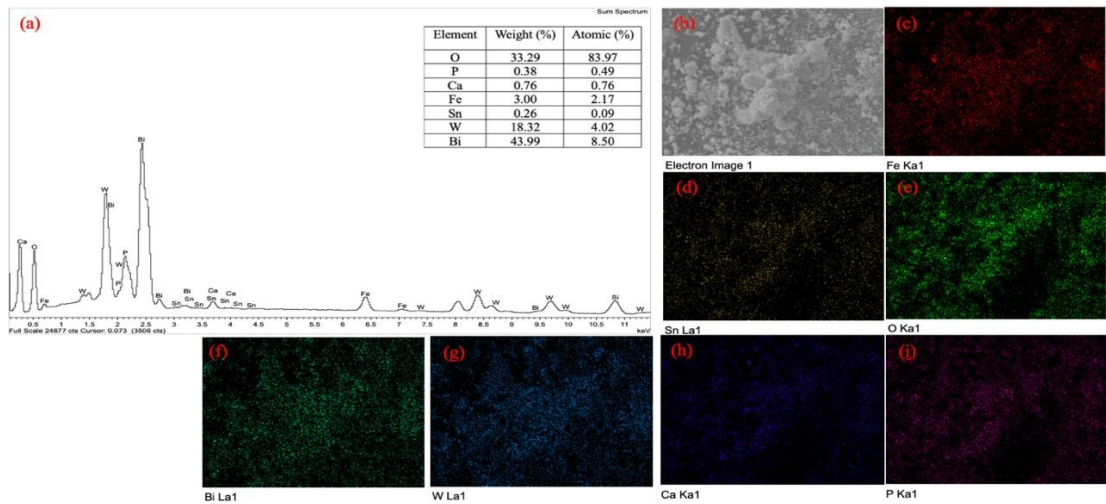


Figure 4.8: (a) The EDX spectra of 7.5 wt%-SnFe<sub>2</sub>O<sub>4</sub>/Bi<sub>2</sub>WO<sub>6</sub>/HAp-1 wt%; (b)-(i) elemental dot mapping of 7.5 wt%-SnFe<sub>2</sub>O<sub>4</sub>/Bi<sub>2</sub>WO<sub>6</sub>/ HAp-1 wt%.

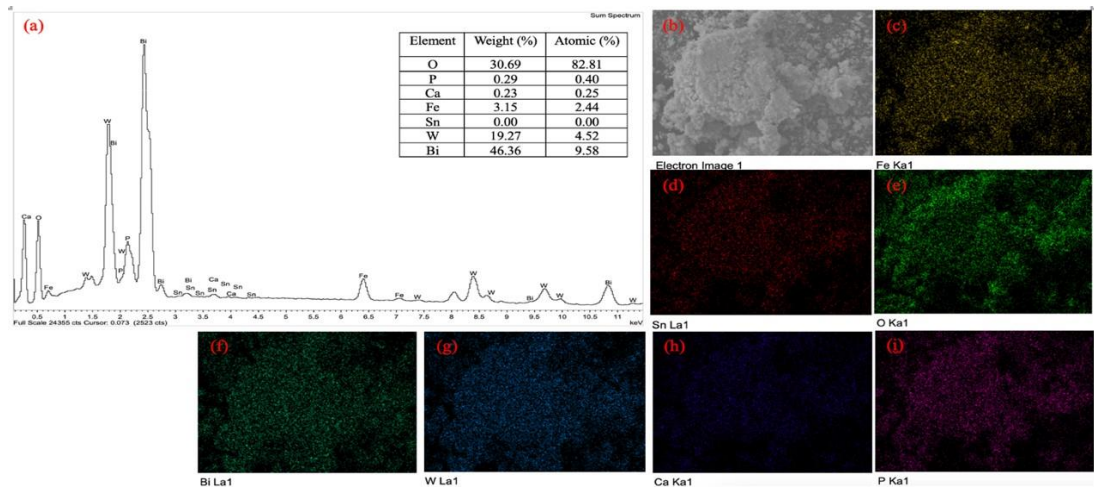


Figure 4.9: (a) The EDX spectra of 7.5 wt%-SnFe<sub>2</sub>O<sub>4</sub>/Bi<sub>2</sub>WO<sub>6</sub>/HAp-3 wt%; (b)-(i) elemental dot mapping of 7.5 wt%-SnFe<sub>2</sub>O<sub>4</sub>/Bi<sub>2</sub>WO<sub>6</sub>/ HAp-3 wt%.

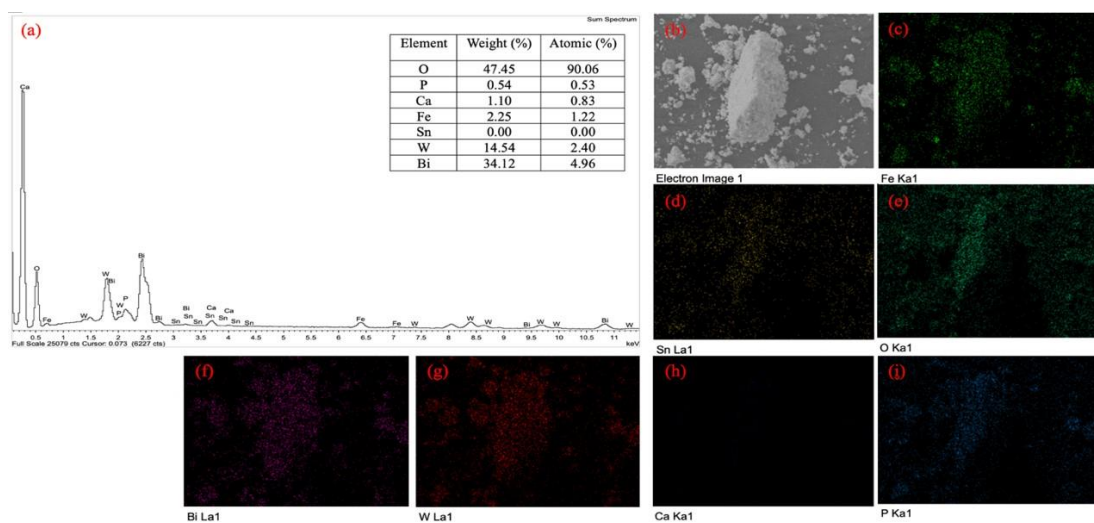
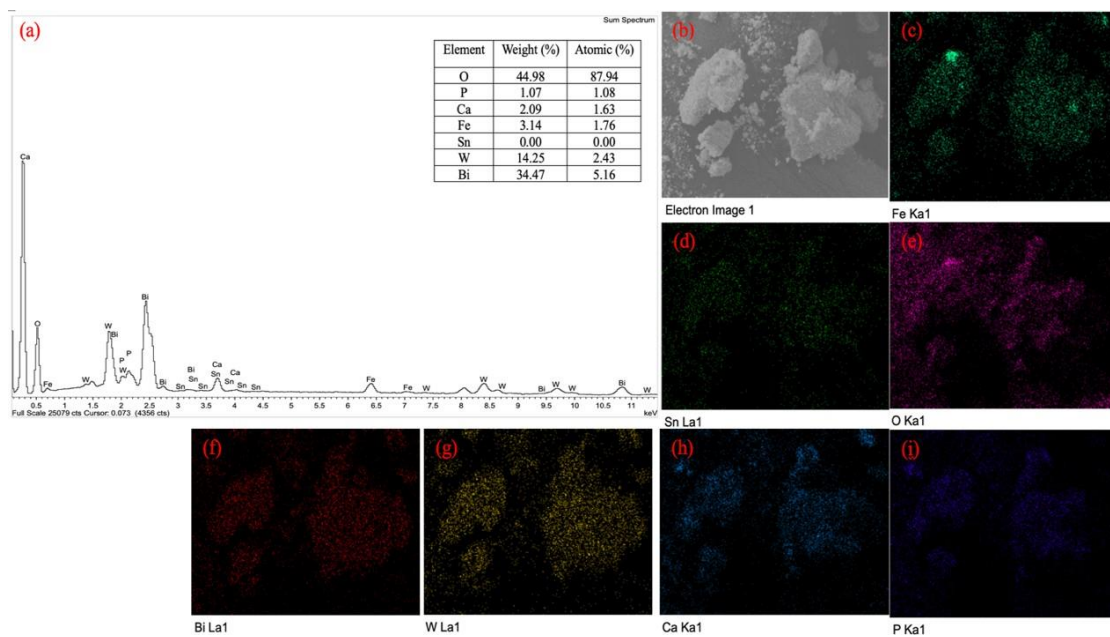


Figure 4.10: (a) The EDX spectra of 7.5 wt%-SnFe<sub>2</sub>O<sub>4</sub>/Bi<sub>2</sub>WO<sub>6</sub>/HAp-5 wt%; (b)-(i) elemental dot mapping of 7.5 wt%-SnFe<sub>2</sub>O<sub>4</sub>/Bi<sub>2</sub>WO<sub>6</sub>/ HAp-5 wt%.



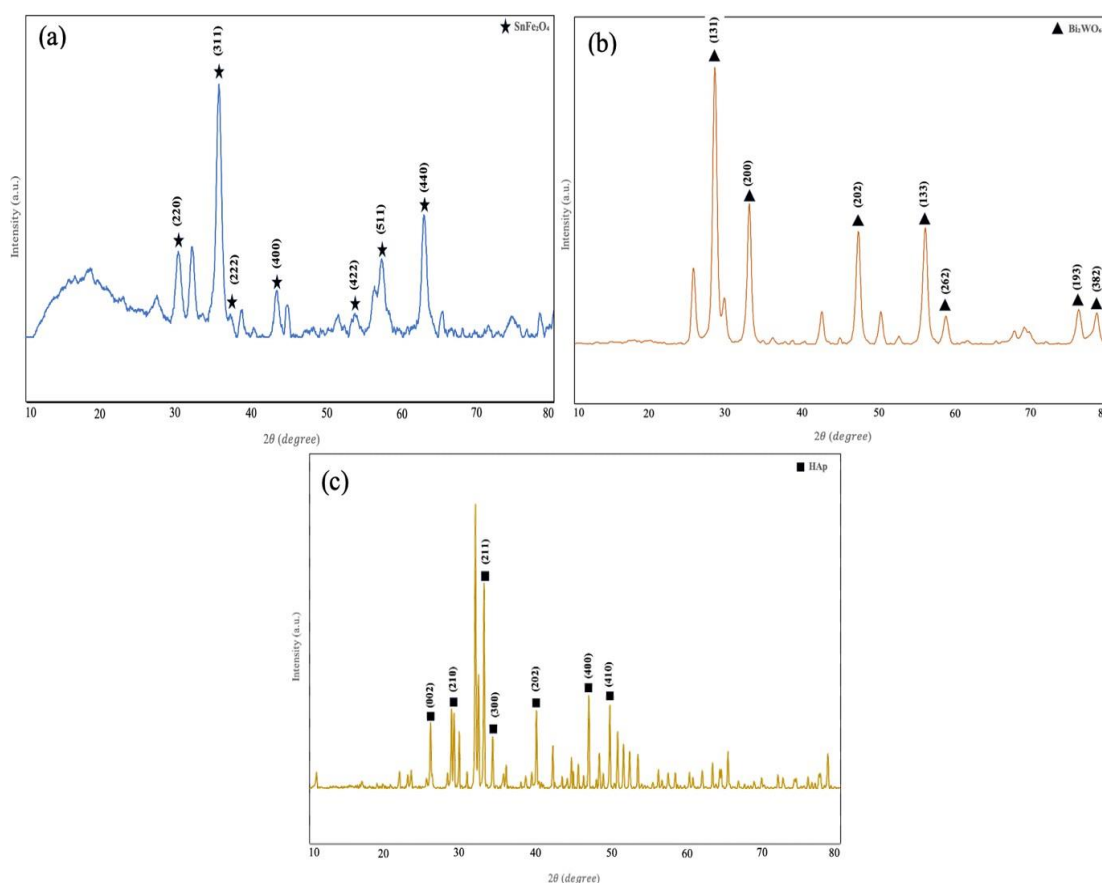
**Figure 4.11: (a) The EDX spectra of 7.5 wt%-SnFe<sub>2</sub>O<sub>4</sub>/Bi<sub>2</sub>WO<sub>6</sub>/HAp-10 wt%; (b)-(i) elemental dot mapping of 7.5 wt%-SnFe<sub>2</sub>O<sub>4</sub>/Bi<sub>2</sub>WO<sub>6</sub>/ HAp-10 wt%.**

### 4.1.3 X-ray Diffraction (XRD)

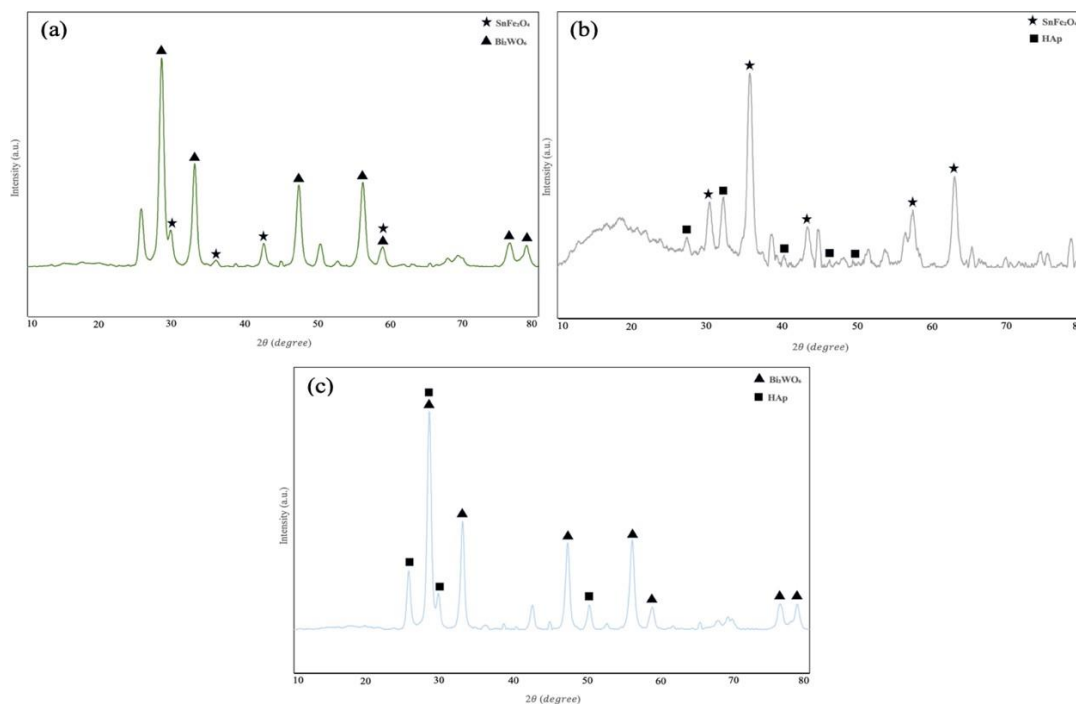
XRD analytical technique is mainly used for determining diffraction patterns and intensities to give insights on the atomic arrangement comprised of phase composition, crystallinity and crystal orientation. As demonstrated in Figure 4.12 (a), the characteristic diffraction peaks of single  $\text{SnFe}_2\text{O}_4$  located at  $2\theta$  of  $30.11^\circ$ ,  $35.45^\circ$ ,  $37.14^\circ$ ,  $43.12^\circ$ ,  $53.48^\circ$ ,  $57.01^\circ$ , and  $62.29^\circ$  are corresponded to the (220), (311), (222), (400), (422), (511), and (440) crystal planes of  $\text{SnFe}_2\text{O}_4$  (JCPDS NO.11-0614), respectively, implying the successful fabrication of single  $\text{SnFe}_2\text{O}_4$  photocatalyst which kept consistent with the finding of the cubic crystal lattice structure of  $\text{SnFe}_2\text{O}_4$  (Ma et al., 2023; Jia et al., 2016). For another single photocatalyst  $\text{Bi}_2\text{WO}_6$  depicted in Figure 4.12 (b) has clearly illustrated the strong diffraction peaks at  $2\theta$  angle of  $28.20^\circ$ ,  $32.80^\circ$ ,  $47.10^\circ$ ,  $55.90^\circ$ ,  $58.60^\circ$ ,  $75.90^\circ$ , and  $78.50^\circ$  which was indexed to the (131), (200), (202), (133), (262), (193), and (382) crystal planes which indicated  $\text{Bi}_2\text{WO}_6$  was in orthorhombic phase is successfully synthesized (JCPDS NO. 39-0256) (Cho et al., 2023). From figure 4.12 (c), all the diffraction peak of HAp can be observed at  $2\theta$  angle of  $26.08^\circ$ ,  $28.69^\circ$ ,  $29.10^\circ$ ,  $31.96^\circ$ ,  $34.26^\circ$ ,  $40.0^\circ$ ,  $46.88^\circ$ , and  $49.66^\circ$  which corresponded to diffraction plane index of (002), (102), (210), (211), (202), (310), (400), and (410), respectively. These detected intense peaks match with HAp in typical hexagonal configuration phase (JCPDS-09-0432) (Palanisamy et al., 2023). The sharp and strong intense peaks indicates that HAp is highly crystalline nanomaterial.

Figure 4.13 (a), (b) and (c) demonstrate the successful preparation of binary nanocomposite photocatalysts, namely 7.5 wt%- $\text{SnFe}_2\text{O}_4/\text{Bi}_2\text{WO}_6$ ,  $\text{SnFe}_2\text{O}_4/\text{HAp}$ -1wt%, and  $\text{Bi}_2\text{WO}_6/\text{HAp}$ -1wt%, respectively. In contrast, Figure 4.14 (a) to (d) illustrate the as-fabricated ternary nanocomposite catalyst with varying HAp loadings (1, 3, 5, and 10wt%). The composite catalyst has similar XRD spectra of that single  $\text{Bi}_2\text{WO}_6$  which attributed to the large percentage content of  $\text{Bi}_2\text{WO}_6$  that play role in ternary photocatalyst. Notably, due to the low concentration of HAp loading, it is quite difficult to detect the distinguished diffraction peaks that belongs to HAp. Plus there are several diffraction peaks that overlapped with other two composite materials, namely  $\text{Bi}_2\text{WO}_6$  and  $\text{SnFe}_2\text{O}_4$ , which cause HAp diffraction peaks easily be influenced when HAp combined with binary nanocomposite of 7.5 wt%- $\text{SnFe}_2\text{O}_4/\text{Bi}_2\text{WO}_6$  via physical mixing method.

Nevertheless, there are no distinct shifts of sharp and strong diffraction peaks when the HAp loading is increased. This can be explained by the change in HAp loading has no brings on significant change in lattice parameter as well as crystallinity of as-synthesised composite. The inconspicuous right shift of diffraction peaks of lattice plane of  $\text{Bi}_2\text{WO}_6$ , namely (131), (200), and (133) implies that little contraction owing to lattice strain. When the HAp loading is increased from 1 to 10wt%, the strength of as-mentioned diffraction peaks belong to  $\text{Bi}_2\text{WO}_6$  is gradually reduced which might be attributed to the interaction between  $\text{Bi}_2\text{WO}_6$  and HAp. Apart from that, no additional diffraction peaks are detected in the ternary heterostructure of  $\text{SnFe}_2\text{O}_4/\text{Bi}_2\text{WO}_6/\text{HAp}$ , reflecting the high purity of composite catalyst are successfully generated.



**Figure 4.12: (a) The XRD spectra of as-fabricated single photocatalysts: (a)  $\text{SnFe}_2\text{O}_4$ ; (b)  $\text{Bi}_2\text{WO}_6$ ; and (c) HAp.**



**Figure 4.13:** (a) The XRD spectra of as-fabricated binary photocatalysts: (a) 7.5 wt%-SnFe<sub>2</sub>O<sub>4</sub>/ Bi<sub>2</sub>WO<sub>6</sub>; (b) Bi<sub>2</sub>WO<sub>6</sub>/HAp-1wt%; and (c) SnFe<sub>2</sub>O<sub>4</sub>/HAp-1wt%.

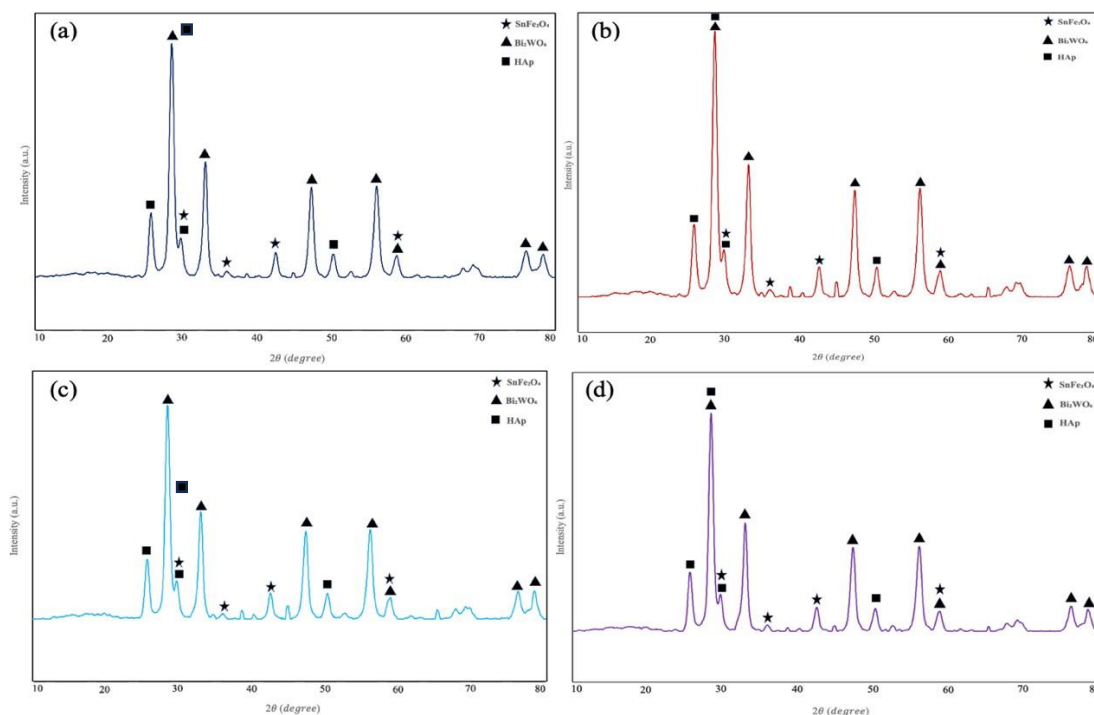


**Figure 4.14:** (a) The XRD spectra of as-fabricated ternary photocatalysts with different HAp loading: (a) 7.5 wt%-SnFe<sub>2</sub>O<sub>4</sub>/Bi<sub>2</sub>WO<sub>6</sub>/HAp-1wt%; (b) 7.5 wt%-SnFe<sub>2</sub>O<sub>4</sub>/Bi<sub>2</sub>WO<sub>6</sub>/HAp-3wt%; and (c) 7.5 wt%-SnFe<sub>2</sub>O<sub>4</sub>/Bi<sub>2</sub>WO<sub>6</sub>/HAp-5wt%; 7.5 wt%-SnFe<sub>2</sub>O<sub>4</sub>/Bi<sub>2</sub>WO<sub>6</sub>/HAp-10wt%.

#### 4.1.4 Attenuated Total Reflectance – Fourier Transform Infrared Spectroscopy (ATR-FTIR)

ATR-FTIR spectroscopy technique is employed for identifying the functional groups as well as chemical bonds that detected within a sample. Therefore, ATR-FTIR absorption peaks of as-synthesized samples are demonstrated in Figure 4.15. From aspect of single photocatalyst of  $\text{SnFe}_2\text{O}_4$ , the characteristic bands at  $436\text{ cm}^{-1}$  and  $543\text{ cm}^{-1}$  are generally rectified as the stretching vibration of Fe-O and Sn-O bonds, respectively in spinel ferrite structure. While the absorption peak at  $1090\text{ cm}^{-1}$  is corresponding to vibration of Sn and Fe in tetrahedral and octahedral sites (Sargazi et al., 2021). The other absorption bands at  $1415\text{ cm}^{-1}$ ,  $1573\text{ cm}^{-1}$ ,  $3349\text{ cm}^{-1}$  are considered as the stretching and bending of -OH groups owing to the atmospheric moisture and the absorbed water molecules during filtration process (Esmaili et al., 2022; Xiao et al., 2021). In addition, for dominant nanomaterial,  $\text{Bi}_2\text{WO}_6$  illustrate its characteristic intense peaks at  $439\text{ cm}^{-1}$  and  $548\text{ cm}^{-1}$  are accredited to stretching vibration of Bi-O bond (Nguyen et al., 2024). The other bands of  $\text{Bi}_2\text{WO}_6$  at  $692\text{ cm}^{-1}$  is considered as bridging vibration of the corner-sharing  $\text{WO}_6$  octahedron while peaks at  $1071\text{ cm}^{-1}$  and  $1405\text{ cm}^{-1}$  can be assigned as the stretching vibration of oxygen located at W-O-W bond (Cho et al., 2023). Peaks at  $1555\text{ cm}^{-1}$  is attributed to stretching of -OH group. The broad band located at around  $3382\text{ cm}^{-1}$  corresponds to stretching of -OH group of absorbed water molecules. Furthermore, the bending vibration of  $\text{PO}_4^{3-}$  group belong to HAp was observed at  $473\text{ cm}^{-1}$  and synthesis of HAp is confirmed as characteristic bands at  $562\text{ cm}^{-1}$  and  $598\text{ cm}^{-1}$  are corresponded to O-P-O bond bending (Palanisamy et al., 2023). Not only that, intense absorption peaks at  $962\text{ cm}^{-1}$ ,  $1020\text{ cm}^{-1}$ , and  $1087\text{ cm}^{-1}$  are contributed to asymmetric stretching of  $\text{PO}_4^{3-}$  group (Caldas et al., 2023). As HAp is also underwent the cleaning process with distilled water and therefore, peaks at  $1415\text{ cm}^{-1}$  and  $1555\text{ cm}^{-1}$  are known as in-plane bending of O-H bonds (Padmanabhan et al., 2019; Xiao et al., 2021). The broad band located at  $3284\text{ cm}^{-1}$  which is within the range of  $3400$  to  $3500\text{ cm}^{-1}$ , implies that formation of hydrogen bonds could enhance the heterogeneous interfacial charge transfer. The absorption peaks of binary nanocomposites, namely  $7.5\text{wt}\%-\text{SnFe}_2\text{O}_4/\text{Bi}_2\text{WO}_6$ ,  $\text{SnFe}_2\text{O}_4/\text{HAp}-1\text{wt}\%$ , and  $\text{Bi}_2\text{WO}_6/\text{HAp}-1\text{wt}\%$  are nearly matched to the peaks of corresponding components. It implies that the washing process with distilled water is effective in removing impurities and prevent existence of uncorrelated functional



groups on the catalyst surface (Nguyen et al., 2024). Notably, the absorption peak intensity at around  $1055\text{ cm}^{-1}$  of  $\text{SnFe}_2\text{O}_4/\text{HAp-1wt\%}$  and  $1058\text{ cm}^{-1}$  of  $\text{Bi}_2\text{WO}_6/\text{HAp-1wt\%}$  are sharply diminished which is attributable to the low content of HAp lead to decrease in diffraction spot of  $\text{PO}_4^{3-}$  group.

When HAp loading is rose from 1 to 10 wt%, the characteristic peak of HAp at  $600\text{ cm}^{-1}$  is become appeared started from 5 wt% HAp loading and peak intensity at around  $1043\text{-}1057\text{ cm}^{-1}$  is strengthened. This is probably due to the reason of increase in HAP amount per unit volume of  $\text{PO}_4^{3-}$  functional group associated with O-P-O bonds. The distinctive small sharp peak at  $963\text{ cm}^{-1}$  was found when HAp loading is 10wt%, implies that the  $\text{PO}_4^{3-}$  group concentration is elevated. It also provides solid proof on supporting increment in HAp loading could offer additional crystalline structure for formation of ternary heterojunction nanocomposite. Yet, an increase in  $\text{PO}_4^{3-}$  group could lead to positive electromagnetic impact that distributed on conduction band, eventually enhances rate of electron-hole pair separation (Naciri et al., 2023).

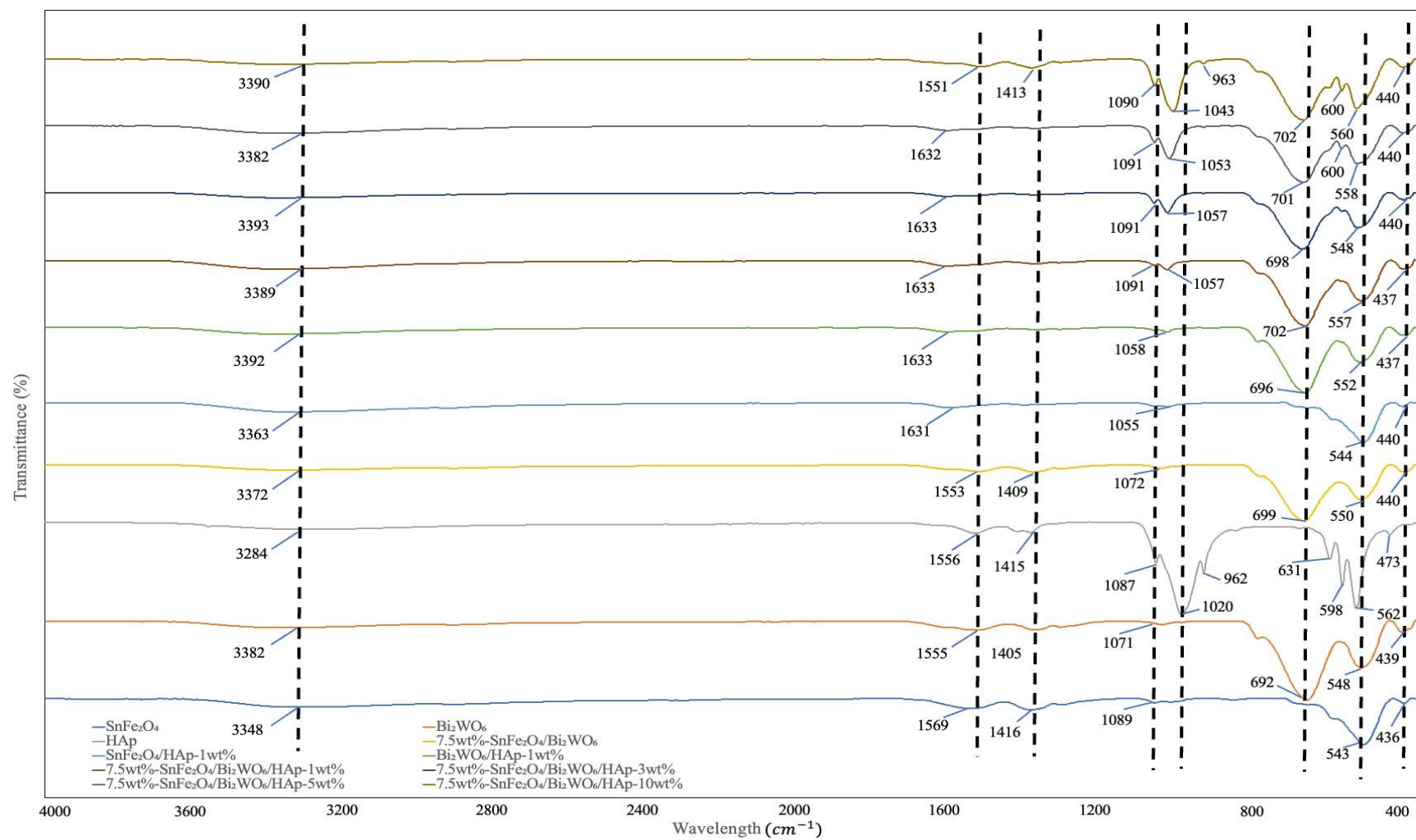


**Figure 4.15: The ATR-FTIR spectra of as-fabricated photocatalysts.**

#### 4.1.5 Ultraviolet-visible Diffuse Reflectance Spectroscopy (UV-vis DRS)

UV-vis DRS was employed to analyse optical characteristics and bandgap energy of the as-synthesized photocatalysts, namely SnFe<sub>2</sub>O<sub>4</sub>, Bi<sub>2</sub>WO<sub>6</sub>, HAp, SnFe<sub>2</sub>O<sub>4</sub>/HAp-1wt%, Bi<sub>2</sub>WO<sub>6</sub>/HAp-1wt%, SnFe<sub>2</sub>O<sub>4</sub>/Bi<sub>2</sub>WO<sub>6</sub>/HAp-1wt%, and SnFe<sub>2</sub>O<sub>4</sub>/Bi<sub>2</sub>WO<sub>6</sub>/HAp-10wt%. As depicted in Figure 4.16, For ternary composite, its visible-light absorption range has shifted to longer wavelength that covered the visible-light spectrum (>400nm) especially HAp loading is 1wt% present in the nanostructure. When the HAp loading increases, the photosensitivity is more restricted on the UV-light absorption, therefore it can be explained that excessive amount of HAp could reduce tendency in harvesting photon energy across a broad spectrum of wavelength covering visible light. It was proven by the fact of absorption intensity in visible light region of ternary composite SnFe<sub>2</sub>O<sub>4</sub>/Bi<sub>2</sub>WO<sub>6</sub>/HAp-1wt% is the highest as compared to binary and single composite materials. For binary composite, obviously the light absorption spectrum of Bi<sub>2</sub>WO<sub>6</sub>/HAp-1wt% is greater than that of SnFe<sub>2</sub>O<sub>4</sub>/HAp-1wt%, because the coupling of Bi<sub>2</sub>WO<sub>6</sub> with HAp could provide a more reliable intermediate energy levels that feasible for photon absorption in a more wide-range visible light spectrum. Nevertheless, HAp has the lowest photoresponsivity in the visible light region owing to its large bandgap characteristic. Thereby, it implies that a large amount of photon energy is needed to harvest for photo-excitation of electrons from VB to CB band edge. In brief, the synergistic effect displayed via incorporation of SnFe<sub>2</sub>O<sub>4</sub> and Bi<sub>2</sub>WO<sub>6</sub> with small quantity of HAp suggest that a suitable bandgap energy could be generated, match the visible light spectrum, and enhance the optical properties. The formation of ternary heterojunction system promote more efficient charge transfer and charge carrier separation, result in higher photocatalytic activities under sunlight irradiation.

Energy bandgap ( $E_g$ ) of as-fabricated photocatalyst can be calculated by applying the following equation (4.1) (Haryński et al., 2022).

$$(\alpha h\nu)^{1/n} = A (h\nu - E_g) \quad (4.1)$$

Where

$\alpha$  = absorption coefficient

$E_g$  = optical band gap of a semiconductor

$h$  = Planck's constant,  $J\cdot s$

$\nu$  = frequency

$n$  = Tauc exponent ( $n = 1/2$  for direct transitions and  $n = 2$  for indirect transitions)

$A$  = proportionality constant

The Tauc exponent,  $n$  is equal to 2 because the dominating semiconductor material  $Bi_2WO_6$  is an indirect bandgap semiconductor (Liu & Fan, 2018). By plotting Tauc plot  $[(\alpha h\nu)^2$  versus  $E_g]$  to estimate the energy bandgap through drawing a tangent line on the wavelength axis. As shown in Figure 4.17, the estimated energy bandgap of  $SnFe_2O_4$ ,  $Bi_2WO_6$ , HAp,  $SnFe_2O_4/HAp-1wt\%$ ,  $Bi_2WO_6/HAp-1wt\%$ ,  $SnFe_2O_4/Bi_2WO_6/HAp-1wt\%$ , and  $SnFe_2O_4/Bi_2WO_6/HAp-10wt\%$  are 2.68 eV, 2.88 eV, 3.8 eV, 3.2 eV, 3.57 eV, 3.1 eV, and 3.46 eV, respectively. Notably,  $SnFe_2O_4/Bi_2WO_6/HAp-1wt\%$  demonstrates a significant reduction of energy bandgap as compared with pure HAp, at the same time this ternary composite has outstanding ability of harnessing visible light for photoexcitation and formation of exciton pairs. Ternary composite with 1 wt% HAp loading has relatively narrower energy bandgap as compared with binary composites, presumably the combination of materials with complementary band structure allowed for higher excitation of photogenerated exciton pairs, enhancing sunlight utilisation efficacy and giving rise to greater photocatalytic performance.

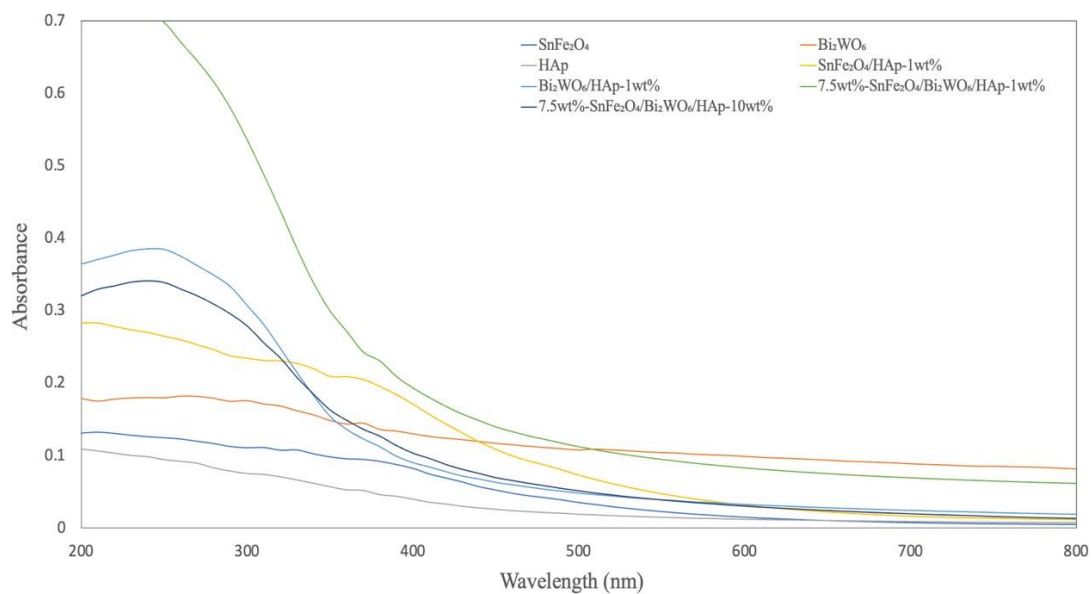


**Figure 4.16: UV-vis absorbance spectra of the as-synthesized photocatalysts.**

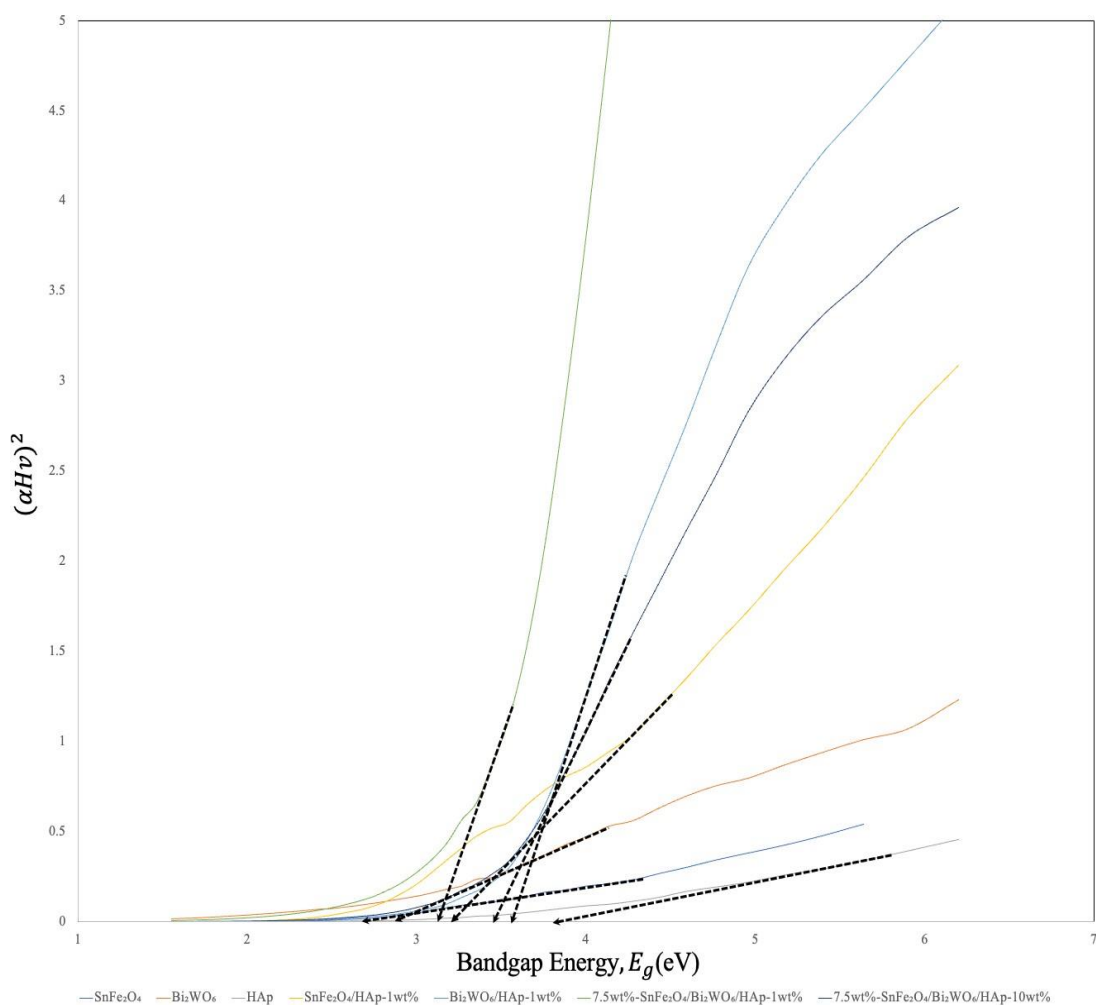


**Figure 4.17: Energy analysis of the as-synthesized photocatalysts via Tauc plot.**

#### 4.1.6 Transient Photocurrent Response (TPR), Electrochemical Impedance Spectroscopy (EIS), Mott-Schottky (M-S), and Cyclic Voltammetry (CV)

Transient photocurrent response of as-prepared photocatalyst analysis is employed for characterizing and evaluate the dynamic behaviours of photo-excited excitons pairs within the material structure when exposed to visible light. This study is basically used to clarify the electron transfer efficacy and provides an understanding of the photocatalytic activity. Figure 4.18 displayed the transient photocurrent response of as-synthesized photocatalysts for five consecutive on-off light cycles. Except pristine HAp showed inconspicuous photocurrent response due to its large energy bandgap, other as-fabricated samples has successfully showed consistent photocurrent response characteristic during visible light repetition switch on-off, implying that these photocatalyst are photosensitive and persistent under visible-light irradiation. As delving into pure semiconductor materials, the light turned on allowed the immediate increase of photocurrent density to respective maximum value, and maintained at steady state for 30 seconds before experiencing abrupt decrease when the light source switched off. The high initial photocurrent density demonstrates that photoexcited charge carriers can be generated rapidly and separated efficiently when illuminated. However, pristine  $\text{Bi}_2\text{WO}_6$  has exhibited higher photosensitivity characteristics compared with pure  $\text{SnFe}_2\text{O}_4$  due to higher surge of photocurrent density once the light turned on. At the meantime, the similar outcome also reflected on the binary composites namely  $\text{SnFe}_2\text{O}_4/\text{HAp-1wt\%}$  and  $\text{Bi}_2\text{WO}_6/\text{HAp-1wt\%}$ . This indicates that  $\text{Bi}_2\text{WO}_6/\text{HAp-1wt\%}$  displays better photoinduced charge carrier separation and transfer within the sample than  $\text{SnFe}_2\text{O}_4/\text{HAp-1wt\%}$ . Ternary composites, 7.5wt%- $\text{SnFe}_2\text{O}_4/\text{Bi}_2\text{WO}_6/\text{HAp-1wt\%}$  demonstrates much greater photocurrent intensities than that of binary composites. It can be attributable to the incorporation of small amount of HAp could greatly improve separation efficiency of photoinduced excitons pairs. Nevertheless, photocurrent densities of ternary composites are progressively reduced when HAp loading is increased which is ascribed to the large energy bandgap of HAp cause the reduction in visible-light photon absorption capability and thus less likely to provides efficient conversion of photon energy into electrical current.

While electrochemical impedance spectroscopy (EIS) analysis was employed for understanding the interfacial properties and charge transfer efficiency of

photocatalyst. Theoretically, charge transfer efficiency is represented by the arc radius formed by the photocatalyst. The smaller the arc of radius in the Nyquist plot indicates the greater the charge carrier separation efficiency as well as interfacial charge transfer. As depicted in Figure 4.19, pristine SnFe<sub>2</sub>O<sub>4</sub> has the smallest radius as compared with pure Bi<sub>2</sub>WO<sub>6</sub> and HAp. This is ascribed to the excellent ferroelectricity which has better electrical response (Salih & Mahmood, 2023). Notably, 7.5wt%-SnFe<sub>2</sub>O<sub>4</sub>/Bi<sub>2</sub>WO<sub>6</sub>/HAp-1wt% has the second smallest arc semicircle as compared to single and binary composites, implies that lower resistance during electron transfer which is extremely beneficial to the photo-electrocatalytic activity. It indicates that incorporation of these three photocatalysts are feasible for facilitating the mobility of photogenerated charge carriers and suppressing the recombination of electron-hole pairs. According to the EIS analysis, Bi<sub>2</sub>WO<sub>6</sub> and HAp had the relatively large semicircle radii as compared to SnFe<sub>2</sub>O<sub>4</sub> in its Nyquist spectra signified the interfacial charge flow resistance is comparatively larger and therefore charge-transfer reaction not easily be triggered at the catalyst's surface (Zhang et al., 2020). For binary composite, semicircle radius of Bi<sub>2</sub>WO<sub>6</sub>/HAp-1wt% is relatively larger than SnFe<sub>2</sub>O<sub>4</sub>/HAp-1wt% and this outcome is corresponding to comparison made in single composite. In short, the construction of ternary heterojunction system of 7.5wt%-SnFe<sub>2</sub>O<sub>4</sub>/Bi<sub>2</sub>WO<sub>6</sub>/HAp-1wt% has exhibits outstanding photoconversion efficiency, expedited photoexcited charge carriers separation and transfer, potentially enhancing the photocatalytic activity as compared with single and binary composites.

Cyclic voltammetry (CV) is used to elucidate the reaction mechanism of as-fabricated photocatalyst and give insight on redox potentials. As depicted in figure 4.20, the anodic peak current ( $I_{pa}$ ) at anodic peak potential ( $E_{pa}$ ) for SnFe<sub>2</sub>O<sub>4</sub>/Bi<sub>2</sub>WO<sub>6</sub>/HAp-1wt% was the highest (67 $\mu$ A/cm<sup>2</sup>) as compared to other photocatalysts. Since the peak current for pristine SnFe<sub>2</sub>O<sub>4</sub>, Bi<sub>2</sub>WO<sub>6</sub> and HAp were 57.5  $\mu$ A/cm<sup>2</sup>, 45.6 $\mu$ A/cm<sup>2</sup> and 29  $\mu$ A/cm<sup>2</sup>, respectively. The higher the anodic peak current, the greater the redox potential and more efficient in interfacial electron transfer. The high current densities shown by SnFe<sub>2</sub>O<sub>4</sub>/Bi<sub>2</sub>WO<sub>6</sub>/HAp-1wt% revealed that this photocatalyst has comparatively larger electrochemical active area which was feasible for electron migration (Shin et al., 2014; Rafat et al., 2021). In short, the incorporation of HAp into SnFe<sub>2</sub>O<sub>4</sub>/Bi<sub>2</sub>WO<sub>6</sub> to form ternary heterojunction and more

photoinduced electrons could be transfer from valence band to conduction band level, eventually lead to effective organic pollutant degradation through redox reaction.

Moreover, flat-band potential ( $E_{FB}$ ) and donor concentration was estimated using x-intercept of linear portion of Mott-Schottky plot. Figure 4.21 (a) to (c) depicts the result of as-synthesized photocatalyst, revealing that pristine  $\text{SnFe}_2\text{O}_4$ ,  $\text{Bi}_2\text{WO}_6$  and HAp were p-type semiconductor with the negative slopes of linear plot. The  $E_{FB}$  of pristine  $\text{SnFe}_2\text{O}_4$ ,  $\text{Bi}_2\text{WO}_6$  and HAp were estimated and determined to be -0.09 eV, 0.47 eV, and 0.55 eV, respectively. By inferring the difference between the band edge of conduction band and  $E_{FB}$  was negligible, therefore the value of  $E_{FB}$  was kept consistent with the conduction band (CB) potential. In other words, band alignment and energy band position of semiconductor materials can be deduced using the following Eq. (4.2),

$$E_{VB} = E_{CB} + E_0 \quad (4.2)$$

Based on the energy bandgap ( $E_g$ ) that was estimated using Tauc plot, namely  $\text{SnFe}_2\text{O}_4$  (2.68 eV),  $\text{Bi}_2\text{WO}_6$  (2.88 eV) and HAp (3.8 eV) can be used to calculate the respective valence band (VB) potential,  $E_{VB}$ . Thus,  $E_{VB}$  for  $\text{SnFe}_2\text{O}_4$ ,  $\text{Bi}_2\text{WO}_6$ , HAp were computed to be 2.59 eV, 3.35 eV and 4.35 eV, respectively. The bandgap alignment of ternary composite of 7.5wt%- $\text{SnFe}_2\text{O}_4/\text{Bi}_2\text{WO}_6/\text{HAp}$ -1wt% is feasible for construction of Z-scheme heterojunction system with excellent redox capability.



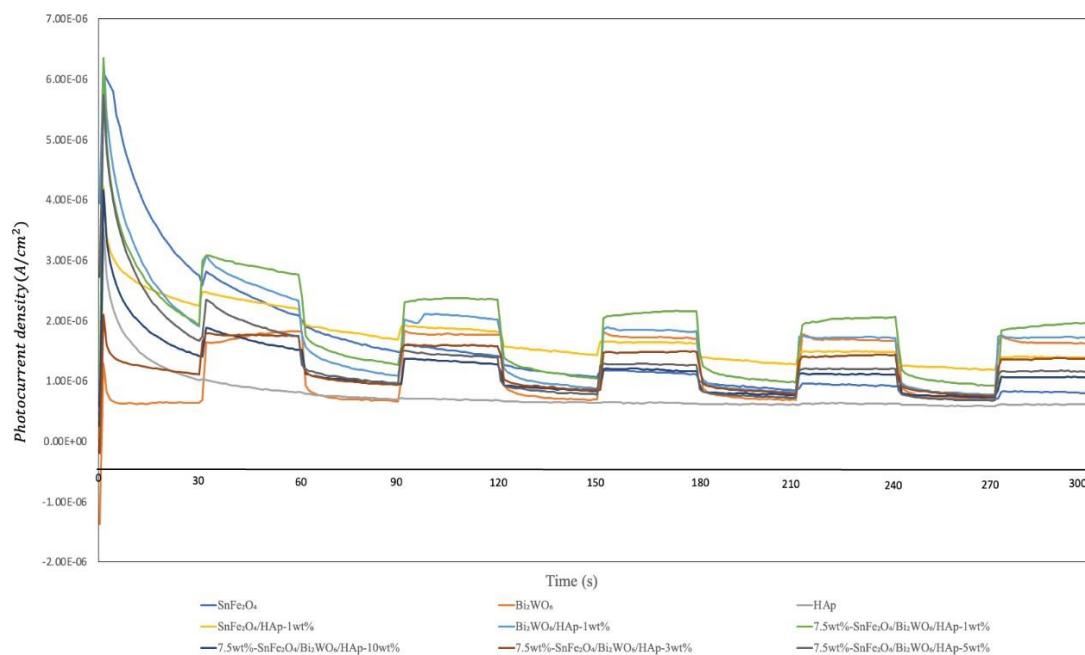


**Figure 4.18: Transient Photocurrent Response of the as-synthesized photocatalysts.**

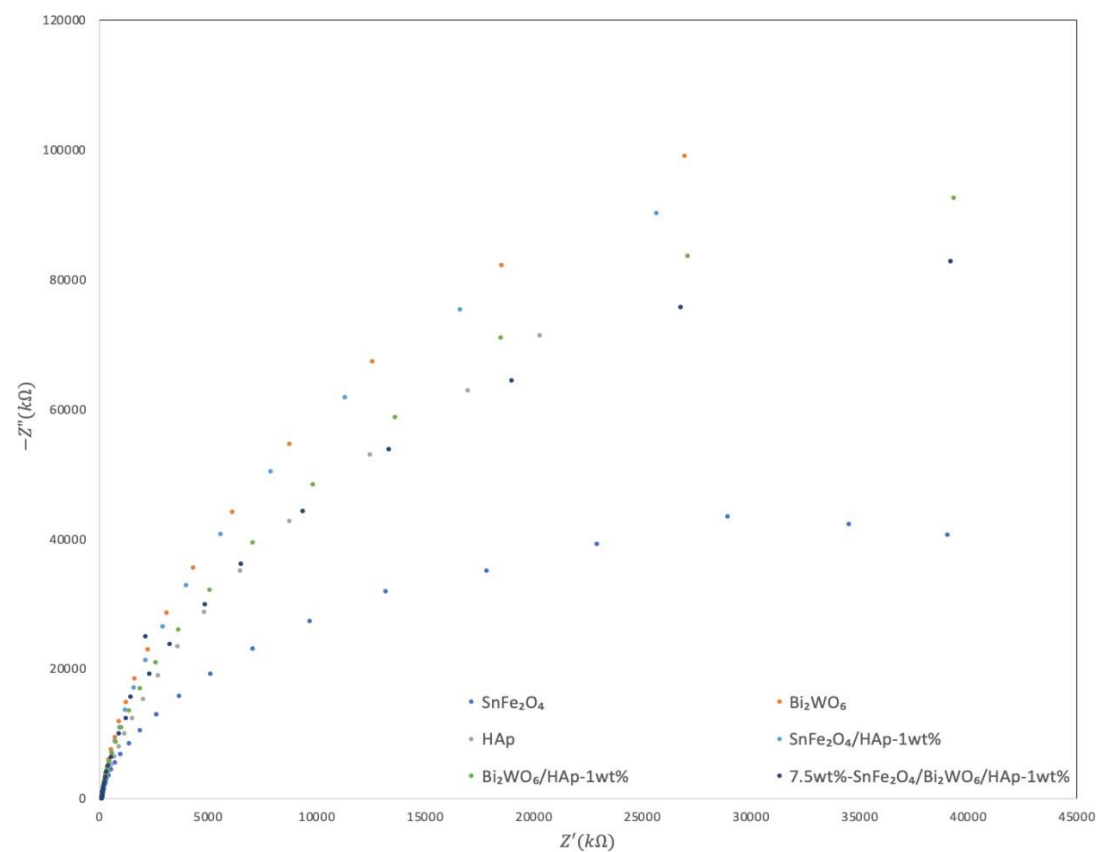


**Figure 4.19: Electrochemical Impedance Spectroscopy analysis of the as-fabricated photocatalysts.**

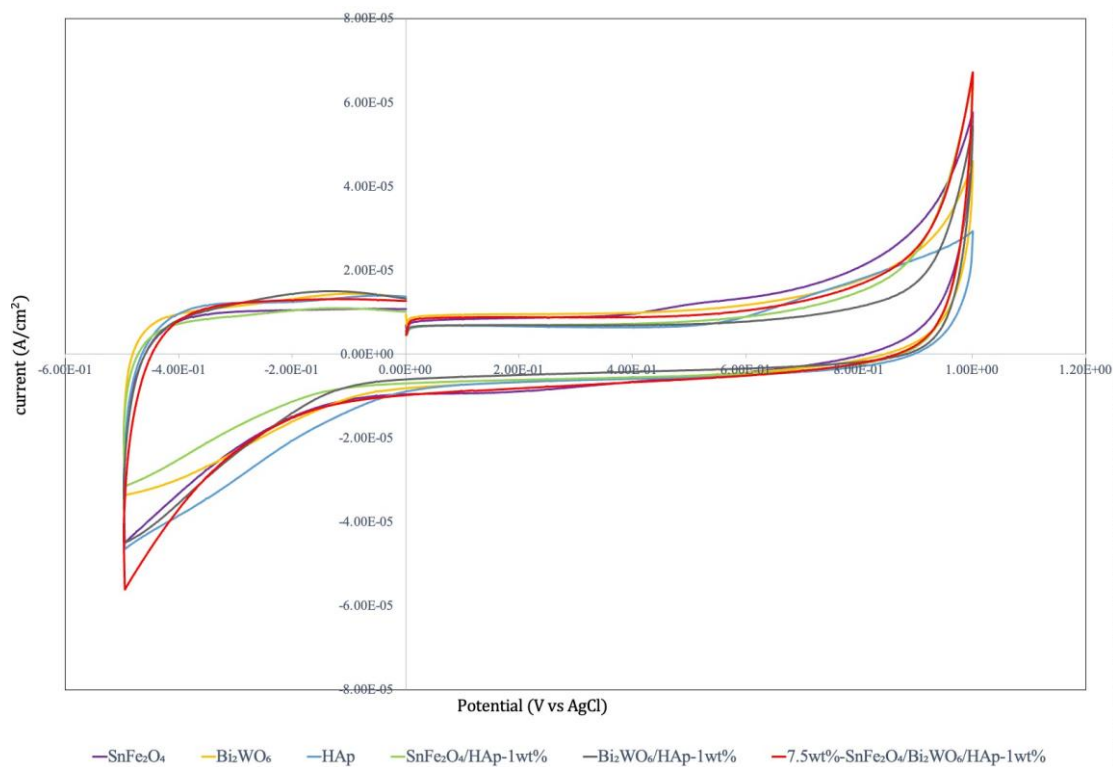


**Figure 4.20: Cyclic voltammetry of the as-synthesized photocatalysts.**

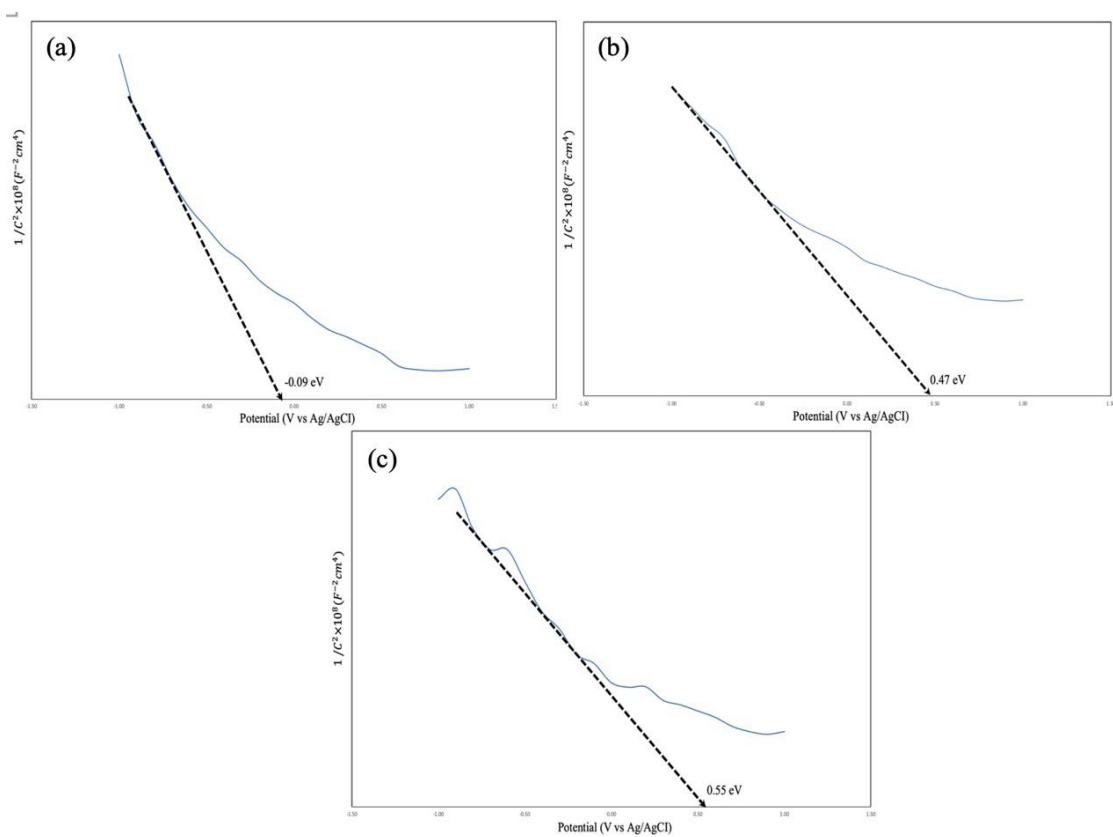


**Figure 4.21: Mott-Schottky analysis of as-prepared photocatalysts: (a) pristine SnFe<sub>2</sub>O<sub>4</sub>; (b) pristine Bi<sub>2</sub>WO<sub>6</sub>; (c) pristine HAp.**

## 4.2 Solar Photocatalytic Activities

### 4.2.1 Photodegradation of Malachite Green (MG)

Figure 4.22 (a) depicts the degradation profiles of malachite green in distilled water using as-fabricated photocatalyst. According to this result, all of the photocatalysts are basically photosensitive and responsive to the light showed stability in degradation of organic dyes under sunlight irradiation. Based on the dark test result, the blank control containing certain quantity of photocatalyst demonstrated insignificant decline in dye concentration with time. It implied that MG dyes has negligible effect on self-degradation by adsorption and it also reflected that all of the degradation performance were initiated by the visible light photon energy absorption and contributed to the photocatalytic decomposition. The concentration of MG dyes solution progressively reduced by all the photocatalysts within the time period of 180 minutes. Notably, the photocatalytic performance of ternary composite 7.5wt%-SnFe<sub>2</sub>O<sub>4</sub>/Bi<sub>2</sub>WO<sub>6</sub>/HAp-1wt% is remarkably excellent (84.63% MG dye removal efficiency) as compared with other ternary composite with HAp loading of 3wt%, 5wt% and 10wt% (removal efficiency of 69.43%, 69.72% and 44.25%, respectively). Performance of 7.5wt%-SnFe<sub>2</sub>O<sub>4</sub>/Bi<sub>2</sub>WO<sub>6</sub>/HAp-1wt% is also greater than binary and single composite. This infers that incorporation of HAp into 7.5wt%-SnFe<sub>2</sub>O<sub>4</sub>/Bi<sub>2</sub>WO<sub>6</sub> has successfully enhanced the charge carrier separation efficiency and more efficient in removing organic contaminants via redox reaction. Further addition of HAp in the formation of ternary composite was unlikely to give rise to positive effect on the degradation efficiency, hence the greater the HAp content, the lower the photocatalytic activity of photocatalyst under light illumination. This result was kept consistent with the analysis of transient photocurrent response (TPR). It can be explained that the addition of excessive amount of HAp could cause alternation and hinder the active sites on the composite's surface, result in decline in specific surface area available for absorption-desorption reaction of target species (Chen et al., 2021).

Moreover, the quantitative experiment data was employed for sake of studying the reaction dynamic of MG photocatalytic decomposition process through fitting into Langmuir Hinshelwood kinetic model using pseudo-first-order equation. As depicted

in Figure 4.22 (b),  $\ln\left(\frac{C}{C_0}\right)$  has linear relationship with time (t) where  $C_0$  and  $C$  were initial concentration and concentration at time t, respectively, inferring that all the curve exhibited were obeyed the first-order kinetics. the slope upon the linear regression is known as apparent first-order reaction rate constant  $k_{app}$ . The reaction rate constant  $k_{app}$  that formed by all the as-prepared samples are plotted in Figure 4.22 (c). In general, the higher the value k, indicates the greater the photodecomposition performance. The reaction rate constant k were arranged in order of  $\text{SnFe}_2\text{O}_4/\text{Bi}_2\text{WO}_6/\text{HAp-1wt\%} > \text{Bi}_2\text{WO}_6/\text{HAp-1wt\%} > \text{HAp} > \text{SnFe}_2\text{O}_4/\text{HAp-1wt\%} > \text{SnFe}_2\text{O}_4/\text{Bi}_2\text{WO}_6/\text{HAp-3wt\%} > \text{SnFe}_2\text{O}_4/\text{Bi}_2\text{WO}_6/\text{HAp-5wt\%} > \text{Bi}_2\text{WO}_6 > \text{SnFe}_2\text{O}_4/\text{Bi}_2\text{WO}_6/\text{HAp-10wt\%} > \text{SnFe}_2\text{O}_4$ . According to Figure 4.22 (c), obviously ternary composite of  $\text{SnFe}_2\text{O}_4/\text{Bi}_2\text{WO}_6/\text{HAp-1wt\%}$  has the greatest reaction rate constant,  $k_{app}$  ( $0.0088 \text{ min}^{-1}$ ) which was nearly 5.17 times higher than  $\text{SnFe}_2\text{O}_4$  ( $0.0017 \text{ min}^{-1}$ ), 1.6 times greater than  $\text{Bi}_2\text{WO}_6$  ( $0.0056 \text{ min}^{-1}$ ) and 1.3 times larger than HAp ( $0.0072 \text{ min}^{-1}$ ). Interestingly, the HAp loading of 1 wt% was the optimum amount present in the ternary composite. Notably, the discrepancy between photocatalytic performance of HAp and TPR analysis was ascribed to the composition of light source. As the TPR analysis was conducted under the visible light illumination, in the stark contrast, the photodegradation of MG-dye solution was carried out under sunlight irradiation in which comprised of UV light that play significant role in photoexcitation of charge carrier pair generation. Therefore, the photodecomposition of dye solution by pristine HAp was expected, to be higher than pristine  $\text{SnFe}_2\text{O}_4$  and  $\text{Bi}_2\text{WO}_6$  owing to the formation of P-OH radicals when lattice oxygen is dissolved and react with  $\text{PO}_4^{3-}$  group and electrons at catalyst surface (Manoj et al., 2019).

Furthermore, figure 4.22 (d) demonstrated the initial absorption peak of MG was at 617 nm and its progressive decrease in absorption peak when reaction time was extended from 0 to 180 minutes with the presence of  $\text{SnFe}_2\text{O}_4/\text{Bi}_2\text{WO}_6/\text{HAp-1wt\%}$ . Based on the observation, the UV-vis spectra of MG and its characteristic peak was shifted to shorter wavelength (centred at 617 nm to 611 nm) and diminished with time. It represents that MG is successfully mineralized by attacking the main functional group of dye molecules and eventually broken down the target species into less harmful products, namely  $\text{CO}_2$ ,  $\text{H}_2\text{O}$ ,  $\text{NH}_4^+$ ,  $\text{HNO}_2$  and  $\text{HNO}_3$  (Rahman et al., 2008). The inset of Figure 4.22 (d) exhibited the colour change of MG solution within 180

minutes. The transition from dark to light shade revealed that a constant decomposition of dye molecule and successfully transformed into simpler molecular compounds.

Bahadoran et al. (2021) has studied the formation of novel binary composite  $\text{Bi}_2\text{WO}_6/\text{ZnBiO}_4$  (BWO/ZBO) with different loading of  $\text{ZnBiO}_4$  on MG dye degradation under visible light illumination. Based on their findings, flake-like heterojunction are constructed via sonochemical assisted hydrothermal approaches. Within 240 minutes of visible light irradiation, the BWO/ZBO-20wt% exhibited the highest removal efficiency of MG dye (86%) which was almost 2.3 times and 2 times larger than pristine ZBO (37%) and BWO (44%), respectively. BWO/ZBO-20wt% has shown the highest photocatalytic activity with reaction rate constant  $k_{app} = 0.0131 \text{ min}^{-1}$  which was much greater than pure BWO ( $0.0042 \text{ min}^{-1}$ ) and ZBO ( $0.0029 \text{ min}^{-1}$ ). The increment of ZBO content more than 20wt% showed insignificant effect on improving degradation efficiencies of organic dyes, it was explained with BWO surface has been fully occupied by ZBO particles and overlapping scenario happened which eventually avoid the light from reaching to the catalyst surface. Therefore, further increase of ZBO content was meaningless in ameliorating the interfacial interaction, lead to reduction of photocatalytic mineralization of dye molecules once the compounding material exceeds the optimum amount. In addition, the earlier studies carried out by Chen et al. (2021) on  $\text{Bi}_2\text{WO}_6$  dominant ternary composite had presented comparable outcomes. A novel  $\text{BiOBr}/\text{Bi}/\text{Bi}_2\text{WO}_6$  was successfully synthesized via hydrothermal method. Based on their findings, the Rhodamine-B (RhB) was employed as target species. The pollutant degradation efficiency of 20%  $\text{BiOBr}/7\% \text{ Bi}/\text{Bi}_2\text{WO}_6$  showed the highest rate of 98.06% which was much greater than its binary composite, 7%  $\text{Bi}/\text{Bi}_2\text{WO}_6$  of 84.65% and ternary composite with different loading of  $\text{BiOBr}$  (10wt% and 30wt%) within 60 minutes of visible light illumination. It was supported with kinetic reaction studies where the  $k_{app}$  of 20%  $\text{BiOBr}/7\% \text{ Bi}/\text{Bi}_2\text{WO}_6$  was  $0.046 \text{ min}^{-1}$  which was 3.7 times larger than pristine BWO ( $0.01256 \text{ min}^{-1}$ ) and 1.9 times larger than 7%  $\text{Bi}/\text{Bi}_2\text{WO}_6$  ( $0.02432 \text{ min}^{-1}$ ). This outstanding pollutant removal effectiveness was ascribed to the perfect match of band position between  $\text{BiOBr}$  and  $\text{Bi}/\text{Bi}_2\text{WO}_6$ , largely reduce the photogenerated electron-hole pair recombination rate while enhanced the interfacial charge transfer. Ternary composite with 20wt% loading of  $\text{BiOBr}$  was considerably achieved the optimum photodecomposition activity. Because when the  $\text{BiOBr}$  content is added more than 30 wt%, could hinder the active site on

catalyst surface and minimize the contact between the visible light and BWO, insufficient photon energy absorption result in reduction of photocatalytic activity of dye mineralization.

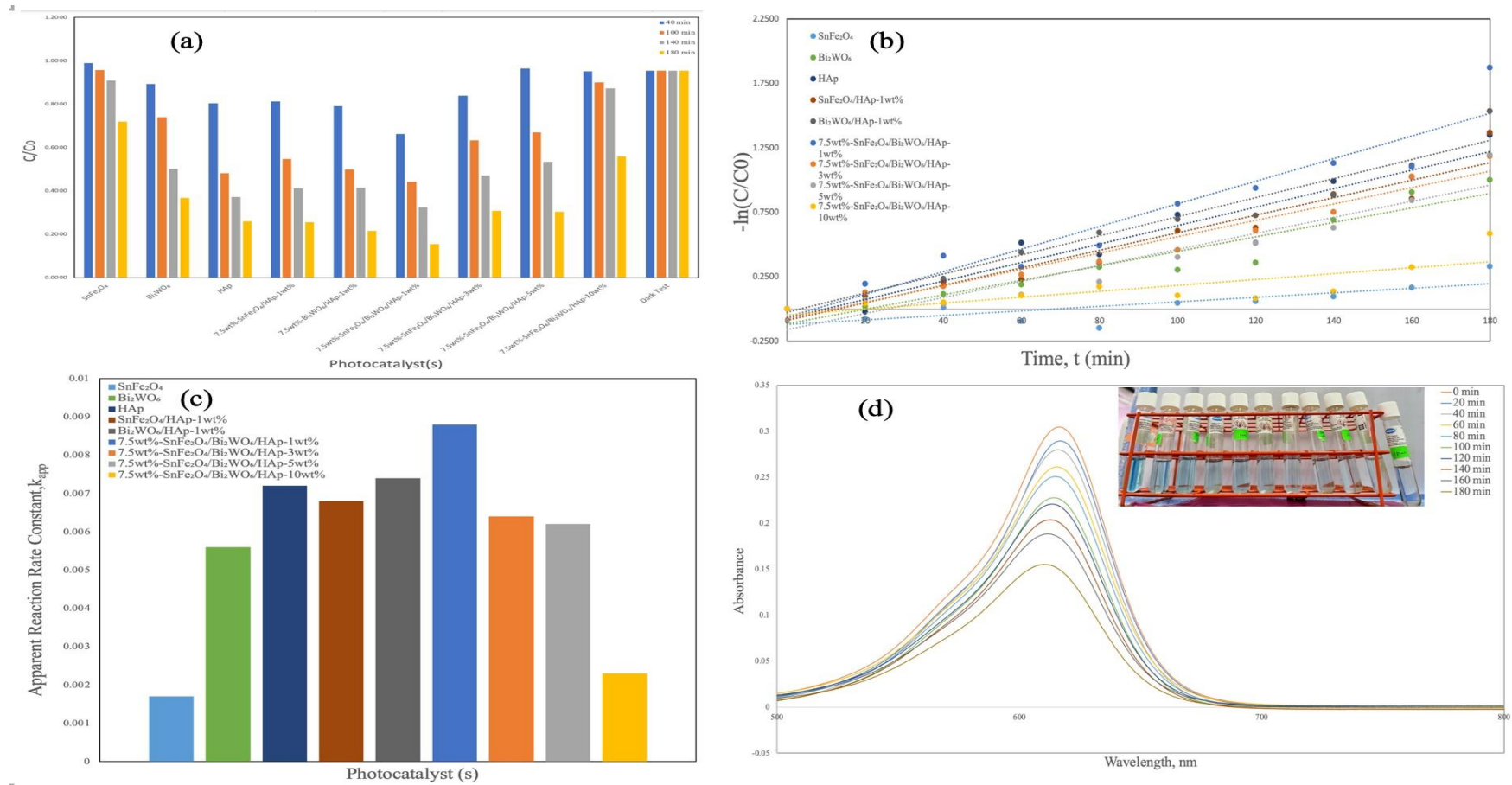


**Figure 4.22:** (a) Degradation profiles of Malachite Green over as-synthesized photocatalyst; (b) Kinetic study for the photodegradation of Malachite Green; (c) Apparent reaction rate constant,  $k_{app}$  over as-synthesized photocatalyst; (d) Absorption spectra of Malachite Green over  $7.5\text{wt}\%-\text{SnFe}_2\text{O}_4/\text{Bi}_2\text{WO}_6/\text{HAp}$ -1wt% ternary composite with the decolourization inset.

#### 4.2.2 Photodegradation of greywater containing Malachite Green (MG)

Photodecomposition of MG dye molecules in greywater has been evaluated and analysed in this section. Figure 4.23 (a) exhibited that the degradation profile of MG in greywater by as-prepared photocatalysts. Accordingly, the removal efficiency under sunlight illumination over 7.5wt%-SnFe<sub>2</sub>O<sub>4</sub>/Bi<sub>2</sub>WO<sub>6</sub>/HAp-1wt% was the highest (99.59%) which was greater than all the binary and single composites, namely SnFe<sub>2</sub>O<sub>4</sub> (34.6%), Bi<sub>2</sub>WO<sub>6</sub> (60.52%), HAp (46.61%), SnFe<sub>2</sub>O<sub>4</sub>/HAp-1wt% (66.42%), and Bi<sub>2</sub>WO<sub>6</sub>/HAp-1wt% (92.14%). The incorporation of HAp with 7.5wt%-SnFe<sub>2</sub>O<sub>4</sub>/Bi<sub>2</sub>WO<sub>6</sub> could form the Z-scheme heterojunction in which the band position of HAp is complementary with that binary composite, result in improved reduction of charge-carrier recombination and accelerated the interfacial charge transfer rate.

As depicted in Figure 4.23 (b) and (c), the reaction rate constant  $k_{app}$  were estimated using the Langmuir Hinshelwood kinetic model and obeyed pseudo-first-order kinetic. Based on the graph shown,  $k_{app}$  value of SnFe<sub>2</sub>O<sub>4</sub>/Bi<sub>2</sub>WO<sub>6</sub>/HAp-1wt%, Bi<sub>2</sub>WO<sub>6</sub>/HAp-1wt%, SnFe<sub>2</sub>O<sub>4</sub>/HAp-1wt%, Bi<sub>2</sub>WO<sub>6</sub>, HAp, and SnFe<sub>2</sub>O<sub>4</sub> were 0.0211 min<sup>-1</sup>, 0.0129 min<sup>-1</sup>, 0.0058 min<sup>-1</sup>, 0.0051 min<sup>-1</sup>, 0.0034 min<sup>-1</sup>, and 0.0023 min<sup>-1</sup>, respectively. Obviously,  $k_{app}$  of aforementioned ternary composite has the highest reaction rate constant which was nearly 9.17 times higher than SnFe<sub>2</sub>O<sub>4</sub>, 4.14 times greater than Bi<sub>2</sub>WO<sub>6</sub> and 6.2 times larger than HAp. It is mainly influenced by the initial pH of the dye-containing aqueous solution. Although the point of zero charge (pH<sub>pzc</sub>) of as-fabricated photocatalyst (Bi<sub>2</sub>WO<sub>6</sub> as dominant material) have not been examined, however pH of greywater is slight alkaline (pH > 7) due to the presence of high concentration surfactants, chemical agents and detergent. The initial pH of aqueous solution is presumably higher than pH<sub>pzc</sub>, catalyst surface became negatively charged. The engagement between negatively-charged photocatalyst interface and positively-charged dye molecules became intensive, inferring that strong electrostatic force of attraction was formed. Apart from that, the alkaline condition is more feasible for generation of reactive oxygen species (ROS) including hydroxyl radicals (•OH) and hydroxide ions (OH<sup>-</sup>) which were the main active species for sake of organic contaminant removal (El Aouni et al., 2024). Combining the large quantities of ROS possibly produced in greywater and strong interaction between target species and



active site of photocatalyst, undoubtedly give rise to a large increment of photodecomposition efficiencies within reaction time of 180 minutes.

Furthermore, figure 4.23 (d) demonstrated gradual decrease in absorption intensities when reaction time was extended from 0 to 180 minutes with the presence of SnFe<sub>2</sub>O<sub>4</sub>/Bi<sub>2</sub>WO<sub>6</sub>/HAp-1wt%. Based on the observation, the UV-vis spectra of MG and its characteristic peak was shifted to even shorter wavelength (centred at 629 nm to 601 nm) and diminished with time as compared with the time. Comparing with previous absorption spectra of MG in deionized water, initial characteristic peak of MG in greywater was shifted to longer wavelength. It phenomenon was attributed to the matrix effect as the varied chemical composition in washing machine greywater could impact the refractive index as well as dielectric constant and thus it relocation of absorption peak occurred. Besides, as shown in Figure 4.24, the reduction of absorption peak represents that MG is successfully mineralized by ROS which attacking the main functional group of dye molecules converted into (4-(dimethylamino) cyclohexa-2,5-dien-1-yl) (4-(dimethylamino) phenyl) (phenyl) methanol, eventually degraded into less harmful products, namely CO<sub>2</sub>, H<sub>2</sub>O, NH<sub>4</sub><sup>+</sup>, HNO<sub>2</sub> and HNO<sub>3</sub> (Rahman et al., 2008; Saad et al., 2020). The inset of Figure 4.23 (d) exhibited the colour change of MG solution within 180 minutes. The transition from heavy to light colour intensity suggested that a constant decomposition of dye molecule and successfully transformed into basic components.

Zhao et al. (2021) has suggested the incorporation of Bi<sub>2</sub>WO<sub>6</sub> with ZnCdS to form binary heterojunction with suitable band position. The binary composite was fabricated with different ZnCdS loading (1 wt%, 1.3wt% and 1.5wt%) via three-step methods. Among as-mentioned photocatalyst, the photocatalytic performance of binary photocatalyst with 1.3wt% ZnCdS was considerably optimum which exhibited as high as 94% of MG dye removal efficiency with reaction rate constant  $k_{app} = 0.0534 \text{ min}^{-1}$  within 50 minutes under visible light illumination. This was much more greater than removal efficiency of pristine ZnCdS of 63% associated with reaction rate constant at  $0.0161 \text{ min}^{-1}$ . It was concluded that although increment of ZnCdS particles increase specific surface area and active site for absorption-desorption reaction, but 1.3wt% loading of ZnCdS incorporated with Bi<sub>2</sub>WO<sub>6</sub> provided the optimum transport efficiency of photoinduced charge carrier simultaneously preventing recombination of

exciton pairs, and result in enhanced photocatalytic performance of photocatalyst. Furthermore, according to Piao et al. (2021), a novel multicomponent dual Z-scheme photocatalyst named  $\text{Bi}_2\text{MnO}_6/\text{Bi}_2\text{WO}_6/\text{AgI}/\text{Ag}$  was successfully constructed through combination of isoelectric point and continuous ion layer adsorption approaches. Notably, the recombination rate of photogenerated carriers in ternary composite of  $\text{Bi}_2\text{MnO}_6/\text{Bi}_2\text{WO}_6/\text{AgI}$  was greatly dampen through incorporation of Ag nanoparticles as co-catalyst by providing additional transfer pathway for photoexcited electrons. The dual Z-scheme heterojunction of  $\text{Bi}_2\text{MnO}_6/\text{Bi}_2\text{WO}_6/\text{AgI}/\text{Ag}$  exhibited the highest degree of degradation of MG dye (94.85%) under simulated solar light illumination. Presence of co-catalyst of Ag has promoted the redox reaction of degraded product including  $\text{NO}_2^-$  ions and finally converted into harmless gas  $\text{N}_2$ . In short, Ag nanoparticles are significantly enhanced the quantum efficiency and photodecomposition performance, thus  $\text{Bi}_2\text{MnO}_6/\text{Bi}_2\text{WO}_6/\text{AgI}/\text{Ag}$  photocatalyst was deem feasible and efficient in treatment of nitrogen-containing organic contaminant in effluent.

Table 4.1 has listed some studies for comparing the photocatalytic MG degradation over  $\text{Bi}_2\text{WO}_6$ -based photocatalyst. Based on these findings, the as-synthesized ternary composite 7.5wt%- $\text{SnFe}_2\text{O}_4/\text{Bi}_2\text{WO}_6/\text{HAp}$ -1wt% was proven to be feasible in dye degradation and exhibited outstanding photocatalytic activity in decomposition of organic contaminants.

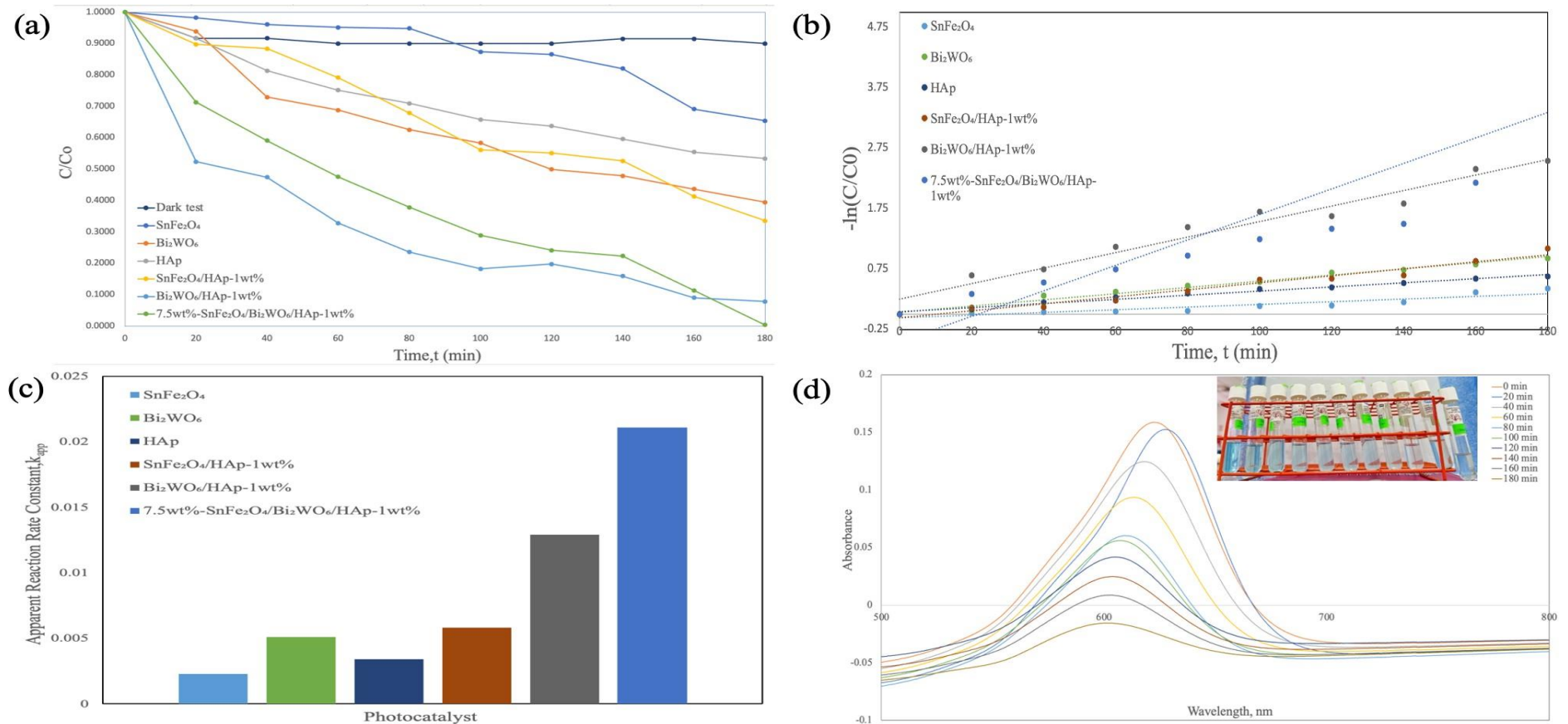


**Figure 4.23: (a) Degradation profiles of Malachite Green over as-synthesized photocatalyst in greywater; (b) Kinetic study for the photodegradation of Malachite Green in greywater; (c) Apparent reaction rate constant,  $k_{app}$  over as-synthesized photocatalyst; (d) Absorption spectra of Malachite Green in greywater over 7.5wt%- $\text{SnFe}_2\text{O}_4/\text{Bi}_2\text{WO}_6/\text{HAp}$ -1wt% ternary composite with the decolourization inset.**

**Table 4.1: Comparison of photocatalytic MG degradation over Bi<sub>2</sub>WO<sub>6</sub>-based photocatalyst.**

Photocatalyst	Pollutant	Synthesis method	Light source	Reaction Condition		Degradation efficiency (%)	Reference
				Catalyst loading (g/L)	Initial concentration of pollutant		
BiOBr/Bi/Bi <sub>2</sub> WO <sub>6</sub>	Malachite Green	Hydrothermal	350 W Xenon lamp	1	10 mg/L	98.02 (60 min)	(Chen et al., 2021)
BWO/ZBO-20wt%	Malachite Green	Sonochemical and hydrothermal	200 W Xenon lamp	0.5	10 mg/L	86% (240 min)	(Bahadoran et al., 2021)
Bi <sub>2</sub> WO <sub>6</sub> /ZnCdS-1.3wt%	Malachite Green	Three-step method	1000 W Xenon lamp	0.6	20 mg/L	94% (50 min)	(Zhao et al., 2021)
Bi <sub>2</sub> MnO <sub>6</sub> /Bi <sub>2</sub> WO <sub>6</sub> /AgI/Ag	Malachite Green	isoelectric point and continuous ion layer	300 W Xenon lamp	0.5	20 mg/L	94.85% (180 min)	Piao et al. (2021)
7.5wt%-SnFe <sub>2</sub> O <sub>4</sub> /Bi <sub>2</sub> WO <sub>6</sub> /HAp-1wt%	Malachite Green	Solvothermal	Sunlight	0.01	5 mg/L	99.59% (180 min)	current study

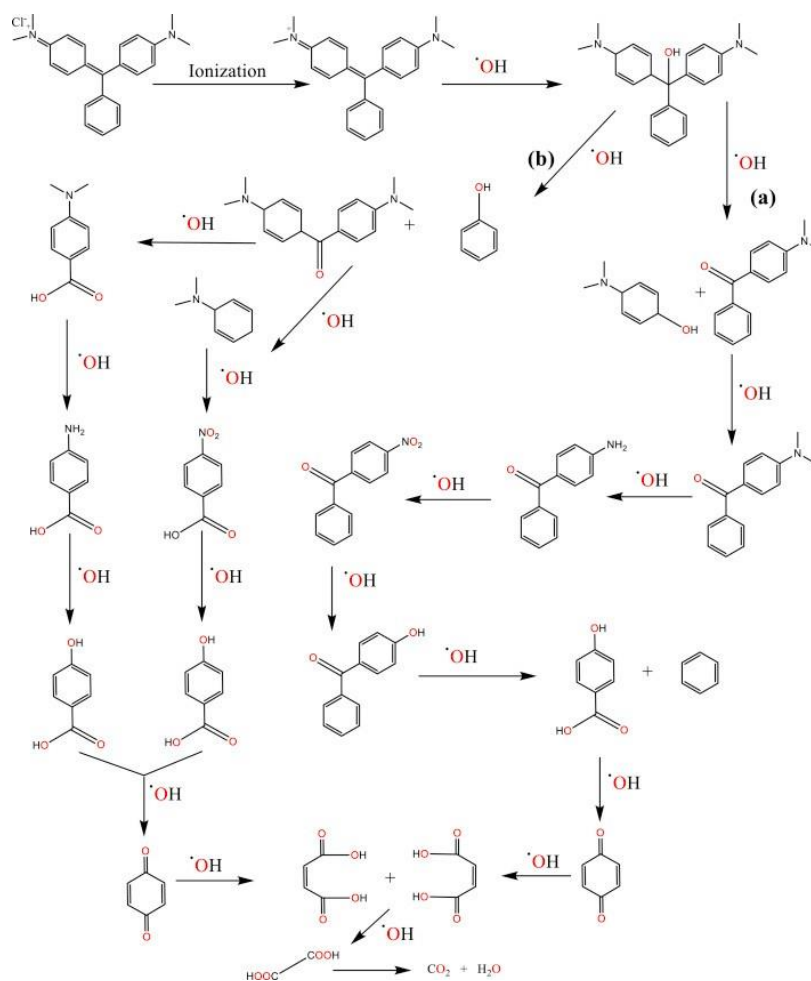


Figure 4.24 shows schematic diagram for the pathway of photocatalytic degradation of MG from complex structure to simpler molecular components.

### 4.3 Phytotoxicity Evaluation

To be noted that the greywater contains high concentration of contaminants which poses harmful impact towards the environment it was not properly treated. Although toxicity level of greywater varied depends on pollutants' concentration, it still cause irreversible damage to the ecological system especially the organic dyes are long-term persistence in water bodies which cannot be self-degraded, and eventually long time exposure to organic dye definitely magnified the detrimental harm to biodiversity. Therefore, phytotoxicity test are essential and meaningful to have a better understanding on effectiveness of photocatalytic treatment. The phytotoxicity of untreated and treated greywater were in terms of growth of mung beans after 7 consecutive days. The sanitized mung beans was cultivated into 3 different conditions, namely distilled water, untreated greywater and treated greywater containing MG through photocatalytic degradation over 7.5wt%-SnFe<sub>2</sub>O<sub>4</sub>/Bi<sub>2</sub>WO<sub>6</sub>/HAp-1wt% ternary composite. As depicted in Figure 4.25 (a)-(d), radicle length of mung beans that cultivated after 7 consecutive days were extracted out for measurement. While Figure 4.25 (e), shows that radicle length of mung beans watered with deionized water (control) is the greatest which could reach the average of 11 cm indicates that the mung beans were planted in a health condition. Interestingly, the untreated household greywater containing MG dye had a suppressive impact on the growth of mung beans, which reflects on the shortest radicle length at average of 2 cm long. Meanwhile, the mung beans that watered with photo-catalytically treated greywater displays a quite impressive result, as radicle length of mature mung beans (average of 9 cm) is much greater than that of mung beans cultivated with untreated solution.

As illustrated in Figure 4.25 (e), the radicle length of mung beans is applied in signifying the decline in phytotoxicity. As demonstrated in Figure 4.25 (e), the phytotoxicity level was placed in order of household greywater containing MG dyes > treated solution > control, with the percentage of 81.81%, 18.18%, and 0%, respectively. Remarkably, the treated greywater containing organic dyes with ternary nanocomposite photocatalytic treatment did not demonstrate negative impact on the germination and growth of mung beans, indicating non-toxicity of treated dyed greywater. This outcome exhibits that 7.5wt%-SnFe<sub>2</sub>O<sub>4</sub>/Bi<sub>2</sub>WO<sub>6</sub>/HAp-1wt% photocatalytic treatment not only effective in removing organic pollutant appeared in

greywater, but simultaneously lower the toxicity level, which has provides a safe and sustainable greywater treatment.

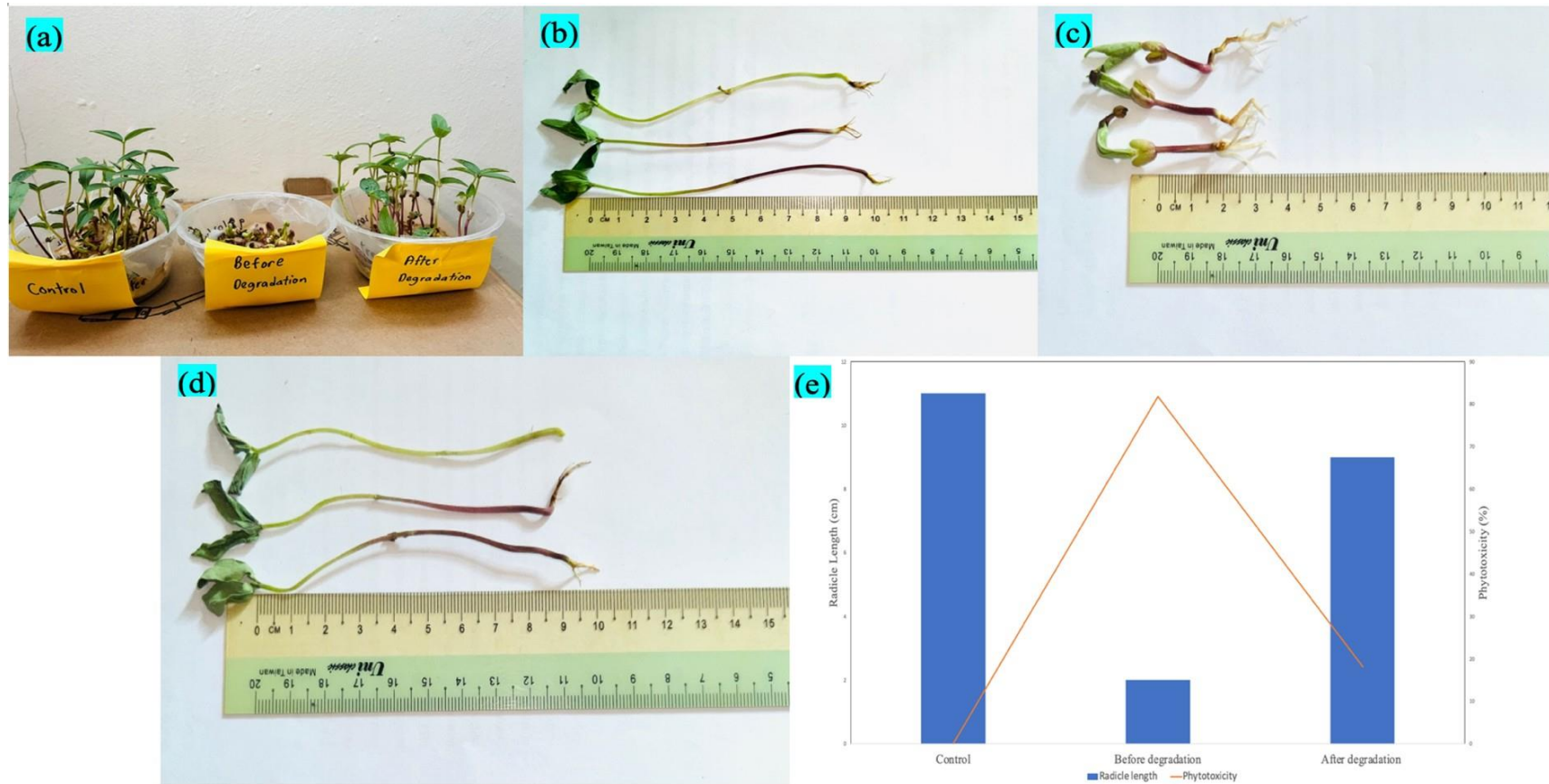


**Figure 4.25: (a) The growth of Mung Beans after 7 Days in different conditions; radicles length of Mung Beans at (b) distilled water; (c) untreated greywater; (d) treated greywater; (e) Phytotoxicity of MG dye in greywater before and after degradation using 7.5wt%-SnFe<sub>2</sub>O<sub>4</sub>/Bi<sub>2</sub>WO<sub>6</sub>/HAp-1wt% nanocomposite.**



#### 4.4 Radical Scavenging Experiment

Radical scavenging experiment was carried out to deduce the photocatalytic mechanism of the as-synthesized ternary composite namely 7.5wt%-SnFe<sub>2</sub>O<sub>4</sub>/Bi<sub>2</sub>WO<sub>6</sub>/HAp-1wt%. Throughout the photodegradation of greywater containing MG dye, the addition of four different types of radical trapping agents, namely EtOH, EDTA, BQ and Na<sub>2</sub>SO<sub>4</sub> were employed to scavenge •OH, h<sub>VB</sub><sup>+</sup>, O<sub>2</sub>•<sup>-</sup>, and e<sub>CB</sub><sup>-</sup>, respectively. According to the result shown in Figure 4.26, the main reactive species has been evaluated. When the 7.5wt%-SnFe<sub>2</sub>O<sub>4</sub>/Bi<sub>2</sub>WO<sub>6</sub>/HAp-1wt% was used as photocatalyst, the photodegradation performance of MG dye-containing greywater was progressively decreased by 39% and 45.4% after EDTA and EtOH were added into solution, respectively. However, the addition of Na<sub>2</sub>SO<sub>4</sub> has shown very slight impact on inhibiting the photocatalytic activities by neutralising the particular reactive oxygen species (ROS) as the degradation efficiency was dropped by approximately 11.85%. While there was a modest decrease in photodegradation efficiency (reduced by 17.98%) when scavenger of BQ was added. Therefore, it suggests that h<sub>VB</sub><sup>+</sup> and •OH play crucial role in the degradation of organic pollutant via redox reaction although these all of the radicals were engaged in degradation of organic dye under sunlight irradiation. The experiment outcome is matched with the findings conducted by Ma et al. (2023), in which •OH, h<sub>VB</sub><sup>+</sup>, O<sub>2</sub>•<sup>-</sup>, and e<sub>CB</sub><sup>-</sup> are participated in photocatalytic reaction.

Based on the obtained findings, a Z-scheme ternary heterojunction photocatalytic mechanism for degradation of MG dye-containing greywater over 7.5wt%-SnFe<sub>2</sub>O<sub>4</sub>/Bi<sub>2</sub>WO<sub>6</sub>/HAp-1wt% was proposed in Figure 4.27. The conduction band (CB) potential and valence band (VB) potential of SnFe<sub>2</sub>O<sub>4</sub> are 0.09 eV and 2.59 eV, respectively. Bi<sub>2</sub>WO<sub>6</sub> possess CB potential of 0.47 eV and VB potential of 3.35 eV. While HAp has CB potential of 0.55 eV and VB potential of 4.35 eV. The possible photodegradation mechanism is expected to follow the pathway as depicted. When the visible light is irradiated, electrons in the valence bands of photocatalysts (SnFe<sub>2</sub>O<sub>4</sub>, Bi<sub>2</sub>WO<sub>6</sub> and HAp) start to absorb the visible-light photon energy and undergo photoexcitation of electrons when the energy absorbed are greater than its respective energy bandgap (E<sub>g</sub>). At this moment, electrons filled in valence band of Bi<sub>2</sub>WO<sub>6</sub> and HAp are migrated to conduction band, respectively. The photoinduced electron-hole

pairs ( $e_{CB}^-$  &  $h_{VB}^+$ ) are formed. The photoinduced  $e_{CB}^-$  transfer from CB of  $Bi_2WO_6$  to VB of  $SnFe_2O_4$ , simultaneously the photogenerated  $e_{CB}^-$  is also migrated from CB of HAp to VB of  $SnFe_2O_4$ . Recombination of photogenerated  $e_{CB}^-$  and  $h_{VB}^+$  occurs at the VB of  $SnFe_2O_4$ . Since CB of  $SnFe_2O_4$  is more negative as compared with other two photocatalyst, therefore its strong reduction capability have been applied for conversion of MG into less harmful products, namely  $CO_2$  and  $H_2O$ . However, CB of  $SnFe_2O_4$  (-0.09 eV) is more negative than redox potential of  $O_2/O_2^{\bullet-}$  (-0.046 eV vs NHE). Therefore, reduction reaction of  $O_2$  was occurred to generate  $O_2^{\bullet-}$  (Hu et al., 2020; Piao et al., 2021; Andrés et al, 2023).  $e_{CB}^-$  was reacted with  $H^+$  and  $O_2$  to form  $H_2O_2$  through reduction reaction because of redox potential of  $O_2/H_2O_2$  (0.682 eV vs NHE) which is less negative than CB of  $SnFe_2O_4$  (-0.09 eV). This can be comprehended as oxygen reduction via reaction with two electrons and two photon with equation of  $[O_2+2e^-+2H^+ \rightarrow H_2O_2]$  that happened at surface of nanocomposite (Hu et al., 2020). Apart from that, VB of HAp (+ 4.35 eV) and  $Bi_2WO_6$  (+ 3.35 eV) is much more positive than redox potential of  $OH^-/\bullet OH$  (+ 2.38 eV vs NHE) and  $H_2O/\bullet OH$  (+ 2.72 eV vs NHE). Thereby,  $H_2O$  and  $OH^-$  are both undergo oxidation reaction by reacting with  $h_{VB}^+$  at the VB of HAp and  $Bi_2WO_6$  to form  $\bullet OH$ . Subsequently, this ROS will react with organic pollutant and convert them into  $CO_2$  and  $H_2O$ . In short, the dominant ROS ( $h_{VB}^+$  and  $\bullet OH$ ) play significant role in degradation of organic contaminant and the removal efficiency of 7.5wt%- $SnFe_2O_4/Bi_2WO_6/HAp$ -1wt% is positively affected by the increasing quantities of  $h_{VB}^+$  and  $\bullet OH$  radicals. The Z-scheme heterojunction formed by combination of  $SnFe_2O_4$ ,  $Bi_2WO_6$  and HAp could further improve the charge carrier separation efficiency, outstanding redox capability in eliminating organic pollutants and enhance the photocatalytic activities.

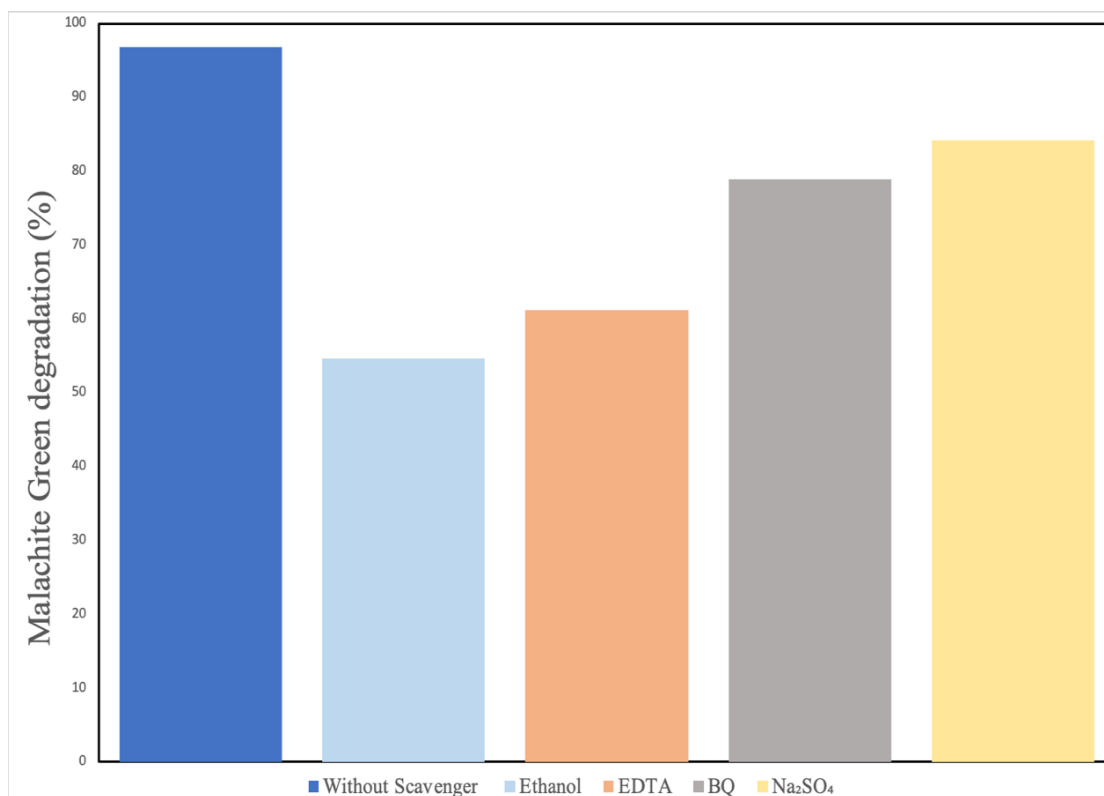


**Figure 4.26: Radical scavenging experiment over 7.5wt%-SnFe<sub>2</sub>O<sub>4</sub>/Bi<sub>2</sub>WO<sub>6</sub>/HAp-1wt% nanocomposite.**

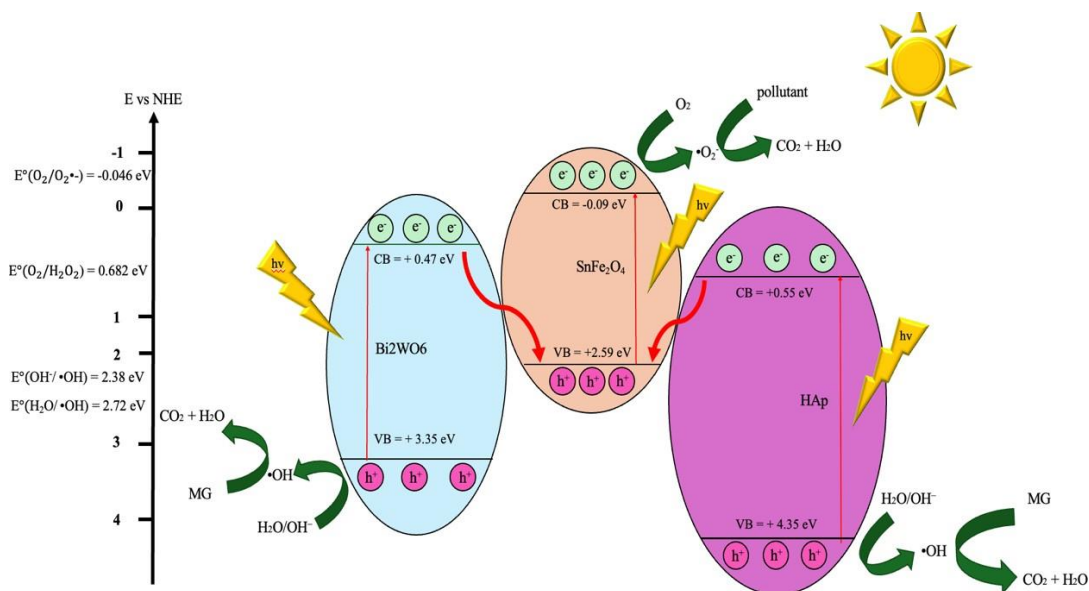


**Figure 4.27: Schematic illustration of charge carrier separation and transfer pathway and photocatalytic mechanism of Z-scheme 7.5wt%-SnFe<sub>2</sub>O<sub>4</sub>/Bi<sub>2</sub>WO<sub>6</sub>/HAp-1wt% nanocomposite heterojunction under sunlight irradiation.**

#### 4.5 Antibacterial Experiment

Based on the observation, pristine  $\text{SnFe}_2\text{O}_4$  and HAp has very low anti-microorganism capability since there was an insignificant reduction of number of *E.coli* colonies in the nutrient plates when irradiation time proceeded from 0 to 180 minutes. For pure HAp, its characteristic large energy bandgap cannot responsive towards to visible light source and therefore this single photocatalyst cannot effectively generate photoinduced electron-holes pairs, *E.coli* unable be removed owing to the quantum efficiency considerably lower. While rapid recombination rate of exciton pairs of pristine  $\text{SnFe}_2\text{O}_4$  is incapable of generating sufficient amount of reactive oxygen species to inhibit the growth of bacteria. In stark contrast, comparing the bacterial growth pattern at irradiation time of 0 min and 180 min, the ternary composite 7.5wt%-  $\text{SnFe}_2\text{O}_4/\text{Bi}_2\text{WO}_6/\text{HAp}$ -1wt% has successfully restrained the bacterial activity as the number of colonies was evidently reduced within 180 minutes irradiation time. The lowest number of colonies after incubated for 24 hours indicated that photocatalytic inactivation over ternary composite was the greatest as compared to single and binary photocatalysts. The synergistic effect between HAp and 7.5wt%- $\text{SnFe}_2\text{O}_4/\text{Bi}_2\text{WO}_6$  has greatly improved the generation of electron-hole pairs, result in producing high quantity of reactive oxygen species including hydroxyl radicals ( $\bullet\text{OH}$ ) and superoxide radical ( $\text{O}_2\bullet^-$ ) to inhibit the bacterium spread on the nutrient agar plate (Wang et al., 2024). Notably, the antibacterial performance of as-prepared samples were kept aligned with the outcome of photodegradation of MG in greywater

## CHAPTER 5

### CONCLUSION AND RECOMMENDATIONS

#### 5.1 Conclusion

In conclusion, a novel Z-scheme 7.5wt%-SnFe<sub>2</sub>O<sub>4</sub>/Bi<sub>2</sub>WO<sub>6</sub>/HAp-1wt% ternary nanocomposite was successfully fabricated via a solvothermal method. This novel Bi<sub>2</sub>WO<sub>6</sub>-based semiconductor photocatalyst has proven to be highly efficient in decomposition of malachite green (MG) in greywater under sunlight illumination. The as-fabricated nanocomposite was analysed using FESEM, EDX, XRD, ATR-FTIR, UV-vis DRS, TPR, EIS, M-S, and CV. Pristine SnFe<sub>2</sub>O<sub>4</sub>, Bi<sub>2</sub>WO<sub>6</sub>, HAp, Bi<sub>2</sub>WO<sub>6</sub>/HAp-1wt%, SnFe<sub>2</sub>O<sub>4</sub>/HAp-1wt% and 7.5wt%-SnFe<sub>2</sub>O<sub>4</sub>/Bi<sub>2</sub>WO<sub>6</sub>/HAp-(3wt%, 5wt%, 10wt%) were also prepared for comparative studies and characterized. The FESEM image has clearly exhibited HAp nanoparticles attached and clumped with binary composite of 7.5wt%-SnFe<sub>2</sub>O<sub>4</sub>/Bi<sub>2</sub>WO<sub>6</sub> which indicated the successful synthesis of ternary heterojunction. It was also found that nanocomposite has higher tendency to clump together and formed a large-sized agglomerate. EDX analysis has validated SnFe<sub>2</sub>O<sub>4</sub>, Bi<sub>2</sub>WO<sub>6</sub> and HAp present in the synthesized ternary samples. XRD has indicated the characteristic peaks of pristine components and no additional diffraction peaks are found, implying high purity of ternary heterostructure of 7.5wt%-SnFe<sub>2</sub>O<sub>4</sub>/Bi<sub>2</sub>WO<sub>6</sub>/HAp-1wt% was synthesized. The visible-light absorption region of 7.5wt%-SnFe<sub>2</sub>O<sub>4</sub>/Bi<sub>2</sub>WO<sub>6</sub>/HAp-1wt% were comparatively larger with appropriate energy bandgap to maximize visible-light utilization. The electrochemical tests of EIS, TPR and CV has demonstrated the incorporation of these three photocatalysts were feasible for promoting the mobility of photoinduced charger carriers and greatly suppressed the recombination rate of electron-hole pairs. Therefore,

SnFe<sub>2</sub>O<sub>4</sub>/Bi<sub>2</sub>WO<sub>6</sub>/HAp-1wt% exhibited exceptional photocatalytic decomposition of organic dye and 84.63% MG ( $k_{app} = 0.0088 \text{ min}^{-1}$ ) has been successfully degraded. Notably, the degradation of greywater containing MG was even higher with removal efficiency of 99.59% and  $k_{app}$  value of  $0.0211 \text{ min}^{-1}$ . This showed high reliability and viability of prepared photocatalyst in practical applications including greywater treatment. In addition, low phytotoxicity level (18.18%) over the as-synthesized ternary composite validated its high effectiveness in lowering the toxicity level and removing organic contaminant appeared in greywater. Based on M-S and radical scavenging result, the Z-scheme ternary heterojunction has successfully constructed in which  $h_{\nu B}^+$  and  $\bullet\text{OH}$  radicals were determined as main reactive oxygen species (ROS) in degradation of organic pollutant under visible light irradiation. The *E-coli* inactivation studies showed the ternary composite has the highest anti-microorganism capability and effectively in restraining the bacterium activity and growth, further showed its versatility and practicability in real-life conditions.

## 5.2 Recommendations

Upon completion of experiments, there are several recommendations can be implemented to improve the overall photocatalytic performance and discover its practical applications in near future,

- a) Some important parameters that significantly affecting photocatalytic degradation including pH, photocatalyst concentration, particle size and reaction temperature, should be further assessed to gain extensive understanding on the photocatalytic capabilities of 7.5wt%-SnFe<sub>2</sub>O<sub>4</sub>/Bi<sub>2</sub>WO<sub>6</sub>/HAp-1wt%.
- b) Examine other appropriate spinel ferrite materials to form new ternary composite for photocatalytic applications.
- c) Conduct the recycling experiment to examine the stability and reusability of 7.5wt%-SnFe<sub>2</sub>O<sub>4</sub>/Bi<sub>2</sub>WO<sub>6</sub>/HAp-1wt%.
- d) Investigate the photocatalytic activity of 7.5wt%-SnFe<sub>2</sub>O<sub>4</sub>/Bi<sub>2</sub>WO<sub>6</sub>/HAp-1wt% under the household lamp illumination for potential indoor applications.

- e) High resolution transmission emission microscopy (HRTEM) analysis could be employed to obtain a more detailed structural morphological information at atomic level while help in understanding the aggregation process.

## REFERENCES

- Ahmad, N. et al., 2024. Layered double hydroxide-functionalized humic acid and magnetite by hydrothermal synthesis for optimized adsorption of Malachite Green. *Kuwait Journal of Science*, 51(2), p.100206.
- Alsulaili, A.D. and Hamoda, M.F., 2015. Quantification and characterization of Greywater from schools. *Water Science and Technology*, 72(11), pp.1973–1980.
- Al-Tohamy, R. et al., 2022. A critical review on the treatment of dye-containing wastewater: Ecotoxicological and health concerns of textile dyes and possible remediation approaches for environmental safety. *Ecotoxicology and Environmental Safety*, 231, p.113160.
- Andrés, C.M. et al., 2023. Superoxide anion chemistry—its role at the core of the innate immunity. *International Journal of Molecular Sciences*, 24(3), p.1841.
- Awan, A.M. et al., 2024. Defects oriented hydrothermal synthesis of TiO<sub>2</sub> and MnTiO<sub>2</sub> nanoparticles as photocatalysts for wastewater treatment and antibacterial applications. *Heliyon*, 10(3).
- Ayoub, M. (2022) “Fenton process for the treatment of wastewater effluent from the edible oil industry,” *Water Science and Technology*, 86(6), pp. 1388–1401. doi:10.2166/wst.2022.283.
- Bahadoran, A., Farhadian, M., Hoseinzadeh, G. and Liu, Q., 2021. Novel flake-like Z-scheme Bi<sub>2</sub>WO<sub>6</sub>-ZnBi<sub>2</sub>O<sub>4</sub> heterostructure prepared by sonochemical assisted hydrothermal procedures with enhanced visible-light photocatalytic activity. *Journal of Alloys and Compounds*, 883, p.160895.
- Barişçi, S., 2018. Electrochemical ferrate(vi) synthesis with cast iron shavings and its potential application for household Graywater Recycling. *Journal of Environmental Engineering*, 144(9).
- Buddiga, L.R. et al., 2023. Structural, surface and optical properties of un-doped and Co-doped Titania Nano photocatalyst for application of antibacterial activity. *Inorganic Chemistry Communications*, 155, p.110980.
- Cai, G., Guo, L., Ge, H. and Wang, J., 2016. A facile method for a quantitative study of the mechanical force impact on fabric dye loss during domestic washing. *Journal of Surfactants and Detergents*, 19(4), pp.901–907.



- Caldas, A.M. et al., 2023. Fabrication of CN-HAp heterostructures from eggshells with improved photocatalytic performance in degrading of mixing dyes under sunlight. *Materials Science in Semiconductor Processing*, 165, p.107660.
- Castro, M.A.M. et al., 2024. Solar-enhanced photodegradation of dye and drug mixture and evaluation of phytotoxicity on seed germination and growth by an eggshell HAp/Nb<sub>2</sub>O<sub>5</sub> heterostructure. *Ceramics International*.
- Chen, L. et al., 2016. Facile synthesis of highly efficient graphitic-C<sub>3</sub>N<sub>4</sub>/ZnFe<sub>2</sub>O<sub>4</sub> heterostructures enhanced visible-light photocatalysis for spiramycin degradation. *Journal of Photochemistry and Photobiology A: Chemistry*, 328, pp.24–32.
- Chen, M., Huang, Y. and Lee, S.C., 2017. Salt-assisted synthesis of hollow Bi<sub>2</sub>WO<sub>6</sub> microspheres with superior photocatalytic activity for no removal. *Chinese Journal of Catalysis*, 38(2), pp.348–356.
- Chen, T., Liu, L., Hu, C. and Huang, H., 2021. Recent advances on Bi<sub>2</sub>WO<sub>6</sub>-based photocatalysts for environmental and Energy Applications. *Chinese Journal of Catalysis*, 42(9), pp.1413–1438.
- Chen, X. et al., 2021. The BiOBr/Bi/Bi<sub>2</sub>WO<sub>6</sub> photocatalyst with SPR effect and Z-scheme heterojunction synergistically degraded RhB under visible light. *Optical Materials*, 122, p.111641.
- Chiatti, F., Corno, M. and Ugliengo, P., 2012. Stability of the Dipolar (001) surface of hydroxyapatite. *The Journal of Physical Chemistry C*, 116(10), pp.6108–6114.
- Cho, E.-C. et al., 2023. Construction of BiVO<sub>4</sub>/Bi<sub>2</sub>WO<sub>6</sub>/WO<sub>3</sub> heterojunctions with improved photocatalytic capability in elimination of Dye and antibiotics and inactivation of *E. coli*. *Journal of the Taiwan Institute of Chemical Engineers*, 149, p.104991.
- Das, J. and Acharya, B.C., 2003. *Water, Air, and Soil Pollution*, 150(1/4), pp.163–175.
- Denchak, M., 2023, *Water pollution: Everything you need to know* [Online]. Available at: <https://www.nrdc.org/stories/water-pollution-everything-you-need-know#whatis> [Accessed: 4 February 2024].
- DEMİR, Ö. and AKTAŞ, E.S., 2022. Effects of advanced oxidation process on greywater treatment: An optimization study. *International Advanced Researches and Engineering Journal*, 6(3), pp.211–219.
- Department of Environment, 2009. Environmental quality industrial effluents regulations 2009. [online] Available at: <[https://www.doe.gov.my/portalv1/wpcontent/uploads/2015/01/Environmental\\_Quality\\_Industrial\\_Effluent\\_Regulations\\_2009\\_-\\_P.U.A\\_434-2009.pdf](https://www.doe.gov.my/portalv1/wpcontent/uploads/2015/01/Environmental_Quality_Industrial_Effluent_Regulations_2009_-_P.U.A_434-2009.pdf)> [Accessed 29 July 2022].

- Devi, M., Praharaj, S. and Rout, D., 2022. Industrial problems and solution towards visible light photocatalysis. *Nanostructured Materials for Visible Light Photocatalysis*, pp.535–567.
- Drumond Chequer, F.M. et al., 2013. Textile dyes: Dyeing Process and environmental impact. *Eco-Friendly Textile Dyeing and Finishing*.
- El Aouni, A. et al., 2024. Design of bismuth tungstate  $\text{Bi}_2\text{WO}_6$  photocatalyst for enhanced and environmentally friendly organic pollutant degradation. *Materials*, 17(5), p.1029.
- Elaouni, A. et al., 2023. Bismuth tungstate  $\text{Bi}_2\text{WO}_6$ : A review on structural, photophysical and photocatalytic properties. *RSC Advances*, 13(26), pp.17476–17494.
- Esmaili, S., Khazaei, A., Ghorbani-Choghamarani, A. and Mohammadi, M., 2022. Silica sulfuric acid coated on  $\text{SnFe}_2\text{O}_4$  mnps: Synthesis, characterization and catalytic applications in the synthesis of polyhydroquinolines. *RSC Advances*, 12(23), pp.14397–14410.
- Fijan, S., Fijan, R. and Šostar-Turk, S., 2008. Implementing sustainable laundering procedures for textiles in a commercial laundry and thus decreasing wastewater burden. *Journal of Cleaner Production*, 16(12), pp.1258–1263.
- FOMCA, 2010. MALAYSIANS Waste a Lot of Water – Water Waste. Malaysia.
- FOMCA, 2017, *Water recycle a sustainable water resources* [Online]. Available at: <https://fomca.org.my/v1/index.php/component/content/article/2-uncategorised/192-water-recycle-a-sustainable-water-resources> [Accessed: 7 February 2024].
- Forgacs, E., Cserháti, T. and Oros, G., 2004. Removal of synthetic dyes from Wastewaters: A Review. *Environment International*, 30(7), pp.953–971.
- Friedmann, D., 2023. Transient absorption spectroscopy insights into heterogeneous photocatalysis for water pollution remediation. *Applied Catalysis A: General*, 649, p.118943.
- Fu, H. and Zhao, Y., 2018. Efficiency droop in GaInN/GaN leds. *Nitride Semiconductor Light-Emitting Diodes (LEDs)*, pp.299–325.
- Ganguly, P., Byrne, C., Breen, A. and Pillai, S.C., 2018. Antimicrobial activity of photocatalysts: fundamentals, mechanisms, kinetics and recent advances. *Applied Catalysis B: Environmental*, 225, pp. 51–75.
- Gordanshekan, A. et al., 2023. A comprehensive comparison of green  $\text{Bi}_2\text{WO}_6/\text{G-C}_3\text{N}_4$  and  $\text{Bi}_2\text{WO}_6/\text{TiO}_2$  s-scheme heterojunctions for photocatalytic adsorption/degradation of Cefixime: Artificial neural network, degradation pathway, and toxicity estimation. *Chemical Engineering Journal*, 451, p.139067.

- Gosens, I. et al., 2010. Impact of agglomeration state of nano- and submicron sized gold particles on pulmonary inflammation. *Particle and Fibre Toxicology*, 7(1), p.37.
- Guidoni, L.L. et al., 2018. Home composting using different ratios of bulking agent to Food Waste. *Journal of Environmental Management*, 207, pp.141–150.
- Han, H. et al., 2022. A review on SnFe<sub>2</sub>O<sub>4</sub> and their composites: Synthesis, properties, and emerging applications. *Progress in Natural Science: Materials International*, 32(5), pp.517–527.
- Haryński, Ł., Olejnik, A., Grochowska, K. and Siuzdak, K., 2022. A facile method for Tauc exponent and corresponding electronic transitions determination in semiconductors directly from UV–vis spectroscopy data. *Optical Materials*, 127, p.112205.
- Hayat, H. et al., 2015. Comparative decolorization of dyes in textile wastewater using biological and Chemical treatment. *Separation and Purification Technology*, 154, pp.149–153.
- Haneef, H.F., Zeidell, A.M. and Jurchescu, O.D., 2020. Charge carrier traps in organic semiconductors: A review on the underlying physics and impact on electronic devices. *Journal of Materials Chemistry C*, 8(3), pp.759–787.
- Hu, Z., Lyu, J. and Ge, M., 2020. Role of reactive oxygen species in the photocatalytic degradation of methyl orange and tetracycline by Ag<sub>3</sub>PO<sub>4</sub> polyhedron modified with G-C<sub>3</sub>N<sub>4</sub>. *Materials Science in Semiconductor Processing*, 105, p.104731.
- Huang, S. et al., 2015. Synthesis of magnetic CoFe<sub>2</sub>O<sub>4</sub>/G-C<sub>3</sub>N<sub>4</sub> composite and its enhancement of photocatalytic ability under visible-light. *Colloids and Surfaces A: Physicochemical and Engineering Aspects*, 478, pp.71–80.
- Ibhadon, A. and Fitzpatrick, P., 2013. Heterogeneous photocatalysis: Recent advances and applications. *Catalysts*, 3(1), pp.189–218.
- İlkiz, B.A., Beceren, Y.İ. and Candan, C., 2021, *An approach to estimate dye concentration of domestic washing machine wastewater* [Online]. Available at: <https://doi.org/10.2478/aut-2019-0062> [Accessed: 27 November 2023].
- Ismail, N., Phang, S.W. and Yoon, L.W., 2023, *World Water Day 2023 - be like a hummingbird and act now - bernama*[Online]. Available at: <https://www.bername.com/en/thoughts/news.php?id=2176451> [Accessed: 5 February 2024].
- Iwase, A. et al., 2011. Reduced graphene oxide as a solid-state electron mediator in Z-scheme photocatalytic water splitting under Visible light. *Journal of the American Chemical Society*, 133(29), pp.11054–11057.

- Jafarova, V.N. and Orudzhev, G.S., 2021. Structural and electronic properties of zno: A first-principles density-functional theory study within LDA(GGA) and LDA(GGA)+U methods. *Solid State Communications*, 325, p.114166.
- Jiang, X. et al., 2022. Magnetically recoverable flower-like Sn<sub>3</sub>O<sub>4</sub>/SnFe<sub>2</sub>O<sub>4</sub> as a type-II heterojunction photocatalyst for efficient degradation of ciprofloxacin. *Journal of Alloys and Compounds*, 926, p.166878.
- Jia, Y. et al., 2016. One-pot solvothermal synthesis of magnetic SnFe<sub>2</sub>O<sub>4</sub> nanoparticles and their performance in the photocatalytic degradation of chlortetracycline with visible light radiation. *RSC Advances*, 6(80), pp.76542–76550.
- Karim, A.V., Krishnan, S. and Shriwastav, A., 2022. An overview of heterogeneous photocatalysis for the degradation of organic compounds: A special emphasis on photocorrosion and reusability. *Journal of the Indian Chemical Society*, 99(6), p.100480.
- Kongsuebchart, W. et al., 2006. Effect of crystallite size on the surface defect of nano-tio<sub>2</sub> prepared via solvothermal synthesis. *Journal of Crystal Growth*, 297(1), pp.234–238.
- Kotian, A. et al., 2024. 3d Pen with cotton cartridge for on-site detection of malachite green dye coating on Okra. *Journal of Food Composition and Analysis*, 128, p.106021.
- Kumar, N., Yadav, S., Mittal, A. and Kumari, K., 2021. Photocatalysis by zinc oxide-based nanomaterials. *Nanostructured Zinc Oxide*, pp.393–457.
- Lam, S.-M., Sin, J.-C., Abdullah, A.Z. and Mohamed, A.R., 2012. Degradation of wastewaters containing organic dyes photocatalysed by Zinc Oxide: A Review. *Desalination and Water Treatment*, 41(1–3), pp.131–169.
- Lam, S.-M. et al., 2024. Improved aquaculture wastewater treatment and concomitant power generation in a photoelectrocatalytic fuel cell equipped with S-scheme Fe<sub>2</sub>WO<sub>6</sub>/ZnO nanorod arrays photoanode and NiFe<sub>2</sub>O<sub>4</sub> cathode. *Separation and Purification Technology*, 329, p.125249.
- Lee, K.-T. and Lu, S.-Y., 2015. A cost-effective, stable, magnetically recyclable photocatalyst of ultra-high organic pollutant degradation efficiency: SnFe<sub>2</sub>O<sub>4</sub> nanocrystals from a carrier solvent assisted interfacial reaction process. *Journal of Materials Chemistry A*, 3(23), pp.12259–12267.
- Li, C. et al., 2015. A novel mesoporous single-crystal-like Bi<sub>2</sub>WO<sub>6</sub> with enhanced photocatalytic activity for pollutants degradation and oxygen production. *ACS Applied Materials & Interfaces*, 7(46), pp.25716–25724.
- Li, S. et al., 2022. Significantly enhanced photocatalytic activity by surface acid corrosion treatment and Au nanoparticles decoration on the surface of SnFe<sub>2</sub>O<sub>4</sub> nano-octahedron. *Separation and Purification Technology*, 299, p.121650.

- Li, S. et al., 2024. Research progress, trends, and updates on pollutants removal by Bi<sub>2</sub>WO<sub>6</sub>-based photocatalysts under visible light irradiation. *Heliyon*, 10(5).
- Liu, H. et al., 2019. Fabrication of Bi<sub>2</sub>S<sub>3</sub>@Bi<sub>2</sub>WO<sub>6</sub>/WO<sub>3</sub> ternary photocatalyst with enhanced photocatalytic performance: Synergistic effect of Z-scheme/traditional heterojunction and oxygen vacancy. *Journal of the Taiwan Institute of Chemical Engineers*, 95, pp.94–102.
- Liu, S. et al., 2010. Impacts of residence time during storage on potential of water saving for Grey Water Recycling System. *Water Research*, 44(1), pp.267–277.
- Liu, X. and Fan, H.-Q., 2018. Theoretical studies on electronic structure and optical properties of Bi<sub>2</sub>WO<sub>6</sub>. *Optik*, 158, pp.962–969.
- Liu, X. and Wang, J., 2024. Decolorization and degradation of various dyes and dye-containing wastewater treatment by electron beam radiation technology: An overview. *Chemosphere*, 351, p.141255.
- Liu, Y., Ding, Z., Lv, H., Guang, J., Li, S., Jiang, J., 2015. Hydrothermal synthesis of hierarchical flower-like Bi<sub>2</sub>WO<sub>6</sub> microspheres with enhanced visible-light photoactivity. *Materials Letters* 157, 158–162. <https://doi.org/10.1016/j.matlet.2015.05.024>
- Liu, Z., Khan, T.A., Islam, Md.A. and Tabrez, U., 2022. A review on the treatment of dyes in printing and dyeing wastewater by plant biomass carbon. *Bioresource Technology*, 354, p.127168.
- Loi, J.X. et al., 2022. Water quality assessment and pollution threat to safe water supply for three river basins in Malaysia. *Science of The Total Environment*, 832, p.155067.
- Low, J. et al., 2017. Heterojunction photocatalysts. *Advanced Materials*, 29(20).
- Lv, C. et al., 2024. Earth-abundant insulator hydroxyapatite-based composite for full-spectrum photocatalytic degradation of 2, 4- Dichlorophenol. *Applied Catalysis B: Environmental*, 340, p.123248.
- Ma, J. et al., 2023. Rational design of a novel magnetically recoverable and environment-friendly Z-scheme SnFe<sub>2</sub>O<sub>4</sub>/Bi<sub>2</sub>WO<sub>6</sub> heterojunction with enhanced photocatalytic performance for rhodamine B degradation and toxicity elimination. *Materials Today Chemistry*, 30, p.101538.
- Mączka, M. et al., 2010. Synthesis and electrical, optical and phonon properties of nanosized aurivillius phase Bi<sub>2</sub>WO<sub>6</sub>. *Materials Chemistry and Physics*, 120(2–3), pp.289–295.
- Madhusudan Reddy, K., Manorama, S.V. and Ramachandra Reddy, A., 2003. Bandgap studies on anatase titanium dioxide nanoparticles. *Materials Chemistry and Physics*, 78(1), pp.239–245.

- Mahmood, Q. et al., 2020. First-Principles Study of magnetic and thermoelectric properties of  $\text{SnFe}_2\text{O}_4$  and  $\text{SmCO}_2\text{O}_4$  spinels. *Journal of Solid State Chemistry*, 286, p.121279.
- Manoj, M., Mangalaraj, D., Meena, P. and Yuan, A., 2019. Facile development and structural investigations of HAp and HAp/TA nanostructures: Photocatalytic activity against TURQ Blue GL Dye. *Materials Research Express*, 7(1), p.015012.
- Mathew, D.D. and Ismail, N., 2023, *Much ado about Malaysia's water woes* [Online]. Available at: <https://www.thestar.com.my/news/nation/2023/05/02/much-ado-about-malysias--water-woes> [Accessed: 19 November 2023].
- Matos, C. et al., 2014. Wastewater and greywater reuse on irrigation in centralized and decentralized systems — an integrated approach on water quality, energy consumption and  $\text{CO}_2$  emissions. *Science of The Total Environment*, 493, pp.463–471.
- Mendes, P.M. et al., 2021. Phytotoxicity test in check: Proposition of methodology for comparison of different method adaptations usually used worldwide. *Journal of Environmental Management*, 291, p.112698.
- MIDA, 2023, *Lifestyle - MIDA: Malaysian Investment Development Authority* [Online]. Available at: <https://www.mida.gov.my/industries/manufacturing/lifestyle/> [Accessed: 9 February 2024].
- Mohamed, W.A.A. et al., 2023. Study of phytotoxicity, remarkable photocatalytic activity, recycling process and energy consumption cost of  $\text{TiO}_2$  quantum dots photocatalyst for photodegradation of Coomassie Brilliant Blue R Dye. *Optical Materials*, 137, p.113607.
- Mohammad, I., Jeshurun, A., Ponnusamy, P. and Reddy, B.M., 2022. Mesoporous graphitic carbon nitride/hydroxyapatite (G- $\text{C}_3\text{N}_4$ /HAp) nanocomposites for highly efficient photocatalytic degradation of rhodamine B dye. *Materials Today Communications*, 33, p.104788.
- Morel, A., Diener, S., 2006. Greywater Management in Low and Middle-income Countries, Review of Different Treatment Systems for Households or Neighbourhoods. Swiss Federal Institute of Aquatic Science and Technology (Eawag). Dübendorf, Switzerland
- Naciri, Y. et al., 2023.  $\text{Ba}_3(\text{PO}_4)_2$  photocatalyst for efficient photocatalytic application. *Global Challenges*, 8(1).
- Nedylakova, M., Medinger, J., Mirabello, G. and Lattuada, M., 2024. Iron oxide magnetic aggregates: Aspects of synthesis, computational approaches and applications. *Advances in Colloid and Interface Science*, 323, p.103056.

- Nguyen, H.C., Le, P.D., Cao, T.M. and Pham, V.V., 2024. Establishing Z-scheme Bi<sub>2</sub>WO<sub>6</sub>/G-C<sub>3</sub>N<sub>4</sub> interfaces toward efficient photocatalytic performance of NO<sub>x</sub> under Visible light. *Journal of Alloys and Compounds*, 989, p.174244.
- Oh, K.S. et al., 2018. A review of Greywater recycling related issues: Challenges and future prospects in Malaysia. *Journal of Cleaner Production*, 171, pp.17–29.
- Ong, Z.C. et al., 2019. Design of a compact and effective greywater treatment system in Malaysia. *DESALINATION AND WATER TREATMENT*, 146, pp.141–151.
- Orimolade, B.O., Idris, A.O., Feleni, U. and Mamba, B., 2021. Recent advances in degradation of pharmaceuticals using Bi<sub>2</sub>WO<sub>6</sub> mediated photocatalysis – A comprehensive review. *Environmental Pollution*, 289, p.117891.
- Oron, G. et al., 2014. Greywater use in Israel and worldwide: Standards and prospects. *Water Research*, 58, pp.92–101.
- Oteng-Peprah, M., Acheampong, M.A. and deVries, N.K., 2018. Greywater characteristics, treatment systems, reuse strategies and user perception—a review. *Water, Air, & Soil Pollution*, 229(8).
- O'Toole, J. et al., 2012. Microbial Quality Assessment of Household Greywater. *Water Research*, 46(13), pp.4301–4313.
- Padmanabhan, V.P. et al., 2019. Microwave synthesis of hydroxyapatite encumbered with ascorbic acid intended for drug leaching studies. *Materials Research Innovations*, 24(3), pp.171–178.
- Palanisamy, G. et al., 2023. Synergistic photocatalytic performance through Z-scheme charge transfer in organic dye degradation using α-MnO<sub>2</sub> nanorods and CO<sub>3</sub>O<sub>4</sub> nanoparticles combined with eggshell derived hydroxyapatite. *Colloids and Surfaces A: Physicochemical and Engineering Aspects*, 677, p.132300.
- Piao, C. et al., 2021. Construction of solar light-driven dual Z-scheme Bi<sub>2</sub>MoO<sub>6</sub>/Bi<sub>2</sub>WO<sub>6</sub>/AgI/Ag Photocatalyst for enhanced simultaneous degradation and conversion of nitrogenous organic pollutants. *Separation and Purification Technology*, 274, p.119140.
- Piccirillo, C. and L. Castro, P.M., 2017. Calcium hydroxyapatite-based photocatalysts for environment remediation: Characteristics, performances and future perspectives. *Journal of Environmental Management*, 193, pp.79–91.
- P, L.R. and Seetharaman, D., 2022. Investigation of thermal stability, structure, magnetic and dielectric properties of solvothermally synthesised SnFe<sub>2</sub>O<sub>4</sub>. *Open Ceramics*, 9, p.100222.
- Pimentel Prates, M. et al., 2023. Fenton: A systematic review of its application in wastewater treatment. *Processes*, 11(8), p.2466.
- Prüss-Üstün, A., Bos, R., Gore, F. and Bartram, J., 2008, [Online]. Available at:

- [https://www.researchgate.net/publication/277802990\\_Safer\\_water\\_better\\_health\\_costs\\_benefits\\_and\\_sustainability\\_of\\_interventions\\_to\\_protect\\_and\\_promote\\_health](https://www.researchgate.net/publication/277802990_Safer_water_better_health_costs_benefits_and_sustainability_of_interventions_to_protect_and_promote_health) [Accessed: 19 November 2023].
- Przystaś, W., Zabłocka-Godlewska, E. and Grabińska-Sota, E., 2011. Biological removal of azo and triphenylmethane dyes and toxicity of process by-products. *Water, Air, & Soil Pollution*, 223(4), pp.1581–1592.
- PubChem, 2024, *Malachite Green* [Online]. Available at: <https://pubchem.ncbi.nlm.nih.gov/compound/Malachite-Green> [Accessed: 11 February 2024].
- Qian, R. et al., 2019. Charge carrier trapping, recombination and transfer during TiO<sub>2</sub> photocatalysis: An overview. *Catalysis Today*, 335, pp.78–90.
- Rafat, M.N. et al., 2021. 3D ternary laccase-GO-TiO<sub>2</sub> nanocomposite synthesized with high power sonication method and sonophotocatalytic efficiency for hydrogen evolution with different scavengers. *Research on Chemical Intermediates*, 47(8), pp.3411–3436.
- Rahman, M.M., Hasnat, M.A. and Sawada, K., 2008. Degradation of commercial textile dye by Fenton's reagent under xenon beam irradiation in aqueous medium. *Journal of Scientific Research*, 1(1), pp.108–120.
- Rodríguez Couto, S., 2009. Dye removal by immobilised fungi. *Biotechnology Advances*, 27(3), pp.227–235.
- Rizzo, L. et al., 2014. Effect of solar simulated N-doped TiO<sub>2</sub> photocatalysis on the inactivation and antibiotic resistance of an *E. coli* strain in biologically treated urban wastewater. *Applied Catalysis B: Environmental*, 144, pp. 369–378.
- Salih, S.J. and Mahmood, W.M., 2023. Review on magnetic spinel ferrite (mFe<sub>2</sub>O<sub>4</sub>) nanoparticles: From synthesis to application. *Heliyon*, 9(6).
- Sargazi, S. et al., 2021. Assessment of SnFe<sub>2</sub>O<sub>4</sub> nanoparticles for potential application in theranostics: Synthesis, characterization, in vitro, and in vivo toxicity. *Materials*, 14(4), p.825.
- Sarkar, S. et al., 2021. Sorptive removal of Malachite Green from aqueous solution by magnetite/coir pith supported sodium alginate beads: Kinetics, isotherms, thermodynamics, and parametric optimization. *Environmental Technology & Innovation*, 24, p.101818.
- Shaikh, I.N. and Ahammed, M.M., 2020. Quantity and quality characteristics of Greywater: A Review. *Journal of Environmental Management*, 261, p.110266.
- Shen, R. et al., 2020. Nanostructured cds for efficient photocatalytic H<sub>2</sub> Evolution: A Review. *Science China Materials*, 63(11), pp.2153–2188.
- Shi, K.-W., Wang, C.-W. and Jiang, S.C., 2018. Quantitative microbial risk assessment



- of Greywater on-site reuse. *Science of The Total Environment*, 635, pp.1507–1519.
- Shin, Y.-E. et al., 2014. An ice-templated, pH-tunable self-assembly route to hierarchically porous graphene nanoscroll networks. *Nanoscale*, 6(16), pp.9734–9741.
- Shindhal, T. et al., 2020. A critical review on advances in the practices and perspectives for the treatment of dye industry wastewater. *Bioengineered*, 12(1), pp.70–87.
- Smith, M., Cross, K., Paden, M. and Laban, P., 2016. *Spring: Managing groundwater sustainably*.
- Subash, B., Krishnakumar, B., Swaminathan, M. and Shanthi, M., 2013. Highly efficient, solar active, and reusable photocatalyst: ZR-loaded Ag–ZnO for reactive red 120 dye degradation with synergistic effect and dye-sensitized mechanism. *Langmuir*, 29(3), pp.939–949.
- Sun, X., Chen, M., Wei, D. and Du, Y., 2019. Research progress of disinfection and disinfection by-products in China. *Journal of Environmental Sciences*, 81, pp. 52–67
- Tahir, N., Zahid, M., Bhatti, I.A., Jamil, Y., 2021. Fabrication of visible light active Mn-doped Bi<sub>2</sub>WO<sub>6</sub>-GO/MoS<sub>2</sub> heterostructure for enhanced photocatalytic degradation of methylene blue. *Environmental Science and Pollution Research* 29, 6552–6567.
- Tan, H.L., Abdi, F.F. and Ng, Y.H., 2019. Heterogeneous photocatalysts: An overview of classic and modern approaches for optical, electronic, and Charge Dynamics Evaluation. *Chemical Society Reviews*, 48(5), pp.1255–1271.
- Tiwari, N. et al., 2023. Photocatalytic degradation of malachite green using TiO<sub>2</sub> and ZnO impregnated on fecal sludge derived BioChar. *Journal of the Taiwan Institute of Chemical Engineers*, 145, p.104800.
- Tran, T.V. et al., 2022. Green synthesis of Mn<sub>3</sub>O<sub>4</sub> nanoparticles using *Costus woodsonii* flowers extract for effective removal of malachite green dye. *Environmental Research*, 214, p.113925.
- Tripathi, R.M. et al., 2015. Facile and rapid biomimetic approach for synthesis of HAp nanofibers and evaluation of their photocatalytic activity. *Materials Letters*, 140, pp.64–67.
- United Nations, 2021, *WHO/UNICEF joint monitoring program for water supply, sanitation and hygiene (JMP) - progress on household drinking water, sanitation and hygiene 2000 - 2020* [Online]. Available at: <https://www.unwater.org/publications/who/unicef-joint-monitoring-program-water-supply-sanitation-and-hygiene-jmp-progress-0> [Accessed: 19 November 2023].

- United Nations Educational, Scientific and Cultural Organization, 2023, [Online]. Available at: <https://www.unesco.org/en/articles/imminent-risk-global-water-crisis-warns-un-world-water-development-report-2023> [Accessed: 20 November 2023].
- United States Environmental Protection Agency, 2023, [Online]. Available at: <https://www.epa.gov/watersense/statistics-and-facts> [Accessed: 19 November 2023].
- Vargas, V.H. et al., 2019. Sisal fiber as an alternative and cost-effective adsorbent for the removal of methylene blue and reactive black 5 dyes from Aqueous Solutions. *Chemical Engineering Communications*, 207(4), pp.523–536.
- Wan, J. et al., 2018. Mesoporous nanoplate multi-directional assembled  $\text{Bi}_2\text{WO}_6$  for high efficient photocatalytic oxidation of no. *Chemosphere*, 193, pp.737–744.
- Wang, H. et al., 2022. A review on heterogeneous photocatalysis for environmental remediation: From semiconductors to modification strategies. *Chinese Journal of Catalysis*, 43(2), pp.178–214.
- Wang, L. et al., 2022. Z-scheme  $\text{Cu}_2(\text{OH})_3\text{F}$  nanosheets-decorated 3D  $\text{Bi}_2\text{WO}_6$  heterojunction with an intimate hetero-surface contact through a hydrogen bond for enhanced photoinduced charge separation and transfer. *Chemical Engineering Journal*, 427, p.131704.
- Wang, X., Tian, P., Lin, Y. and Li, L., 2015. Hierarchical nanostructures assembled from ultrathin  $\text{Bi}_2\text{WO}_6$  nanoflakes and their visible-light induced photocatalytic property. *Journal of Alloys and Compounds*, 620, pp.228–232.
- Wang, Y. et al., 2024. Enhanced led light-driven antibacterial system with efficient charge transfer coordinated by  $\text{Bi}_2\text{WO}_6/\text{TiO}_2$  Z-scheme heterojunction. *Ceramics International*, 50(6), pp.9307–9322.
- WHO, 2023, *Drinking-water* [Online]. Available at: <https://www.who.int/news-room/fact-sheets/detail/drinking-water> [Accessed: 7 February 2024].
- Xiao, S., Fakhri, A. and Janani, B.J., 2021. Synthesis of spinel tin ferrite decorated on bismuth ferrite nanostructures for synergetic photocatalytic, superior drug delivery, and antibacterial efficiencies. *Surfaces and Interfaces*, 27, p.101490.
- Wijetunga, S., Li, X.-F. and Jian, C., 2010. Effect of organic load on decolourization of textile wastewater containing acid dyes in upflow anaerobic sludge blanket reactor. *Journal of Hazardous Materials*, 177(1–3), pp.792–798.
- Xu, F. et al., 2018. Ultra-thin  $\text{Bi}_2\text{WO}_6$  porous nanosheets with high lattice coherence for enhanced performance for photocatalytic reduction of Cr(VI). *Journal of Colloid and Interface Science*, 525, pp.97–106.
- Yahya, N. et al., 2018. A review of integrated photocatalyst adsorbents for wastewater treatment. *Journal of Environmental Chemical Engineering*, 6 (6), pp. 7411–7425.

- Yang, A.-M. et al., 2017. Synthesis and comparison of photocatalytic properties for B  $\text{Bi}_2\text{WO}_6$  nanofibers and hierarchical microspheres. *Journal of Alloys and Compounds*, 695, pp.915–921.
- Yong, Z.-J. et al., 2024. Incorporating photocatalytic fuel cell with dual S-scheme  $\text{CuBi}_2\text{O}_4/\text{Bi}_2\text{WO}_6/\text{ZnO}$  NRA photoanode for energy recuperation from municipal wastewater treatment under sunlight. *Journal of Environmental Chemical Engineering*, 12(1), p.111606.
- Yusof, M.F. et al., 2022, *Clean water production enhancement through the integration of small-scale solar stills with solar dish concentrators (SDCs)-A Review* [Online]. Available at: <https://www.mdpi.com/2071-1050/14/9/5442> [Accessed: 19 November 2023].
- Zaheer, A., 2023, *Top 20 countries with highest water consumption* [Online]. Available at: [https://finance.yahoo.com/news/top-20-countries-highest-water-234541941.html?guccounter=1&guce\\_referrer=aHR0cHM6Ly93d3cuZ29vZ2xILmNvbS5zZy8&guce\\_referrer\\_sig=AQAAAMZTVGyRc4CH7UnhDdQvGK5nVocx4l\\_dFbrgYmEBULvzgw3wbgGzfYD1sw5EF0bWaqevboBYfyjk3EnkYYEDBSUoJE8ZFeebBMctH9SOmVpuINzk5qpIMTOf3M3nnBhcY\\_RdH-Mu4s2yI56POlcssMqTGvbLkVnGSRF8BU3F1xT-](https://finance.yahoo.com/news/top-20-countries-highest-water-234541941.html?guccounter=1&guce_referrer=aHR0cHM6Ly93d3cuZ29vZ2xILmNvbS5zZy8&guce_referrer_sig=AQAAAMZTVGyRc4CH7UnhDdQvGK5nVocx4l_dFbrgYmEBULvzgw3wbgGzfYD1sw5EF0bWaqevboBYfyjk3EnkYYEDBSUoJE8ZFeebBMctH9SOmVpuINzk5qpIMTOf3M3nnBhcY_RdH-Mu4s2yI56POlcssMqTGvbLkVnGSRF8BU3F1xT-) [Accessed: 19 November 2023].
- Zhang, G.-L. et al., 2021. Synergistic effects of flake-like  $\text{ZnO}/\text{SnFe}_2\text{O}_4$ /nitrogen-doped carbon composites on structural stability and electrochemical behavior for lithium-ion batteries. *Journal of Colloid and Interface Science*, 594, pp.173–185.
- Zhang, Y. et al., 2022. Synthesis of  $\text{SnO}_2/\text{ZnO}$  flower-like composites photocatalyst for enhanced photocatalytic degradation of Malachite Green. *Optical Materials*, 133, p.112978.
- Zhang, L. and Zhu, Y., 2012. A review of controllable synthesis and enhancement of performances of bismuth tungstate visible-light-driven photocatalysts. *Catalysis Science & Technology*, 2(4), p.694.
- Zhang, W. et al., 2020. High electrochemical performance of  $\text{Bi}_2\text{WO}_6$ /carbon nanion composites as electrode materials for pseudocapacitors. *Frontiers in Chemistry*, 8.
- Zhao, G., Liu, S. and Lu, Q., 2012. One-dimensional  $\text{Bi}_2\text{WO}_6$  nanofibers controllable synthesis by electrospinning and enhanced visible photocatalytic degradation performances. *Journal of Cluster Science*, 24(2), pp.523–530.
- Zhao, X. et al., 2021. Construction and enhanced efficiency of Z-scheme-based  $\text{ZnCdS}/\text{Bi}_2\text{WO}_6$  composites for visible-light-driven photocatalytic dye degradation. *Journal of Physics and Chemistry of Solids*, 154, p.110075.
- Zhou, Y. et al., 2015. Monolayered  $\text{Bi}_2\text{WO}_6$  nanosheets mimicking heterojunction interface with open surfaces for photocatalysis. *Nature Communications*, 6(1).